

# Politecnico di Torino

## Master's Degree in Civil Engineering



# Politecnico di Torino

### Master's degree Thesis

## Huge underground caverns design and excavation: interpretation of monitoring data through back-analyses.

Supervisors

Prof. MONICA BARBERO

ENG. GIOVANNI QUAGLIO

ENG. SIMONE ADDOTTO

Candidate

MOHAMED IBRAHIM

March 2022



# Summary

Nowadays, in conjunction with the tremendous demand for electricity which is the backbone of the new civilization, humanity searches for renewable and sustainable resources of electric energy and invests a lot of money to find modern solutions. Thus, one of the innovative technologies in the new era is the power pumped-storage hydroelectric plants underground. In addition to that, the superb latest technologies not only generate electricity from these hydropower plants but restore the excess energy that already exists on the grid. So, these hydropower plants act as large batteries. Also, these plants have less cost, less environmental harm, no greenhouse gases emission, and their life cycle has around 40-50 years.

The study reported a discussion about a hydropower plant located 300 meters below the ground surface in the complexity of geological conditions, heterogeneity, and anisotropy of the rock mass. the storage capacity of water that will be in the upper and lower reservoirs reach around three and half million cubic meters. The head between the upper and lower reservoirs will be around 450 m. The project consists of around 6 km of underground tunnels. and two caverns that are 97m long, 18 meters wide, and 27 meters high.

The purpose of the thesis is a scope on back-analysis of a huge underground caverns excavation of hydroelectric plant and interpretation of monitoring data. This study is based on data provided by a monitoring system; in particular, the displacements recorded by the extensometers and the forces provided by the instrumented tendons and bar anchors of the caverns are considered. In addition, a time-dependent analysis is carried out to predict the performance of the rock mass around the excavation contour, and the stability of the excavated structure over time.

All the analyses using FEM, implemented in RS3 code (Rocscience,2021) which is an efficient tool to deal with the high level of details and complexity of the stratigraphy.

The analysis is based on the latest geological model and the mapping information that was obtained during excavation. Furthermore, the results are compared with

the results received from FLAC3D code (Itasca,2020) with equivalent geomechanically and in situ stress parameters.

Thanks to the process of the back-analysis and the evaluation of the performance of the excavated structure, reached outcomes can be used as a handling tool in prediction procedure to foretell the creep behavior, time dependence of the rock mass, and the stability of the hydropower plant over the life cycle of the project.

# Acknowledgements

First of all, I would like to thank my supervisor, prof. Monica Barbero for her kindness, support, and availability.

Then, my gratefulness to my supervisor Eng. Giovanni Quaglio who gave me that opportunity, with his guidance and observations through all the phases of the project. Also, I want to thank Eng. Simone Addotto and Eng. Cristiano Bertello for their contribution to this work. Finally, I extend my thanks to all the staff in Geodata.

Last but not least, my deep praise to ALLAH, as for always being by my side. I am grateful to my parents. I wish you both were still alive to see my graduation. Also, to my siblings for their motivation and encouragement.



# Table of Contents

<b>List of Tables</b>	VIII
<b>List of Figures</b>	IX
<b>Acronyms</b>	XV
<b>1 Introduction</b>	1
<b>2 Geological condition.</b>	3
2.1 Description of study case . . . . .	3
2.2 Geological model . . . . .	4
2.2.1 Lithology . . . . .	4
2.2.2 Geological structure. . . . .	7
2.2.3 Rock classification. . . . .	9
2.2.4 Geological Model . . . . .	10
2.3 In-situ stress . . . . .	11
2.4 Suggested parameters for rock mass . . . . .	11
<b>3 Support and monitoring design</b>	13
3.1 Support elements and monitoring devices . . . . .	13
3.1.1 Rock bolt . . . . .	13
3.1.2 Bar anchors and tendons . . . . .	13
3.2 Support design . . . . .	16
3.2.1 Vault . . . . .	16
3.2.2 Upstream side wall . . . . .	18
3.2.3 Downstream side wall. . . . .	20
3.2.4 Southern ending wall. . . . .	22
3.2.5 Northern ending wall. . . . .	24
3.3 Monitoring Design . . . . .	31
3.3.1 Extensometers and load cells . . . . .	31
3.3.2 Monitoring system . . . . .	33

<b>4</b>	<b>Back analysis technical route and parameters</b>	<b>37</b>
4.1	Back analysis technical route . . . . .	37
4.2	Rock mass constitutive mechanical model . . . . .	38
4.3	The parameters from back analysis . . . . .	43
<b>5</b>	<b>Back analysis with 3D models</b>	<b>45</b>
5.1	3D geological model and excavated structure . . . . .	45
5.1.1	3D geological model . . . . .	45
5.1.2	Modelling the excavated structures . . . . .	52
5.2	Numerical models and boundaries . . . . .	57
5.2.1	Model geometry and excavation procedure. . . . .	57
5.2.2	Different loads of simulation . . . . .	58
5.3	Modeling the supports elements . . . . .	68
<b>6</b>	<b>The Back analysis results</b>	<b>72</b>
6.1	Total displacements . . . . .	72
6.2	Axial forces in tendons and bar anchors . . . . .	81
6.3	Stresses in rock dowels . . . . .	83
6.4	Plastic zones . . . . .	85
6.5	Monitoring data comparison . . . . .	91
<b>7</b>	<b>time dependent behavior of rock mass</b>	<b>99</b>
7.1	Introduction . . . . .	99
7.2	Prediction of the stress-strain behaviour of rock mass . . . . .	99
7.3	Strength parameters update . . . . .	105
7.4	Long term behaviour results . . . . .	112
7.4.1	First scenario simulation . . . . .	112
7.4.2	Second scenario simulation . . . . .	115
<b>8</b>	<b>Conclusion</b>	<b>119</b>
	<b>Bibliography</b>	<b>120</b>

# List of Tables

2.1	Summaries of faults and deformation zones . . . . .	8
2.2	The proportion of each rock mass class . . . . .	9
2.3	Magnitude and orientation of principal stress components. . . . .	11
2.4	Hoek-Brown failure parameters data. . . . .	11
2.5	Input data for faults . . . . .	12
3.1	Supports of powerhouse vault. . . . .	17
3.2	Support of upstream sidewall. . . . .	19
3.3	Support of downstream sidewall. . . . .	21
3.4	Support of south ending wall. . . . .	23
3.5	Support of the north wall . . . . .	26
4.1	Updated parameters for bs-strong class III and bs-weak class III/IV	44
4.2	Updated parameters for pyr IV and bs-weak V . . . . .	44
6.1	Results of the monitoring load cells and RS3 outputs on up stream side wall. . . . .	92
6.2	Results of the monitoring load cells and RS3 outputs on down stream side wall. . . . .	94
6.3	Results of the monitoring load cells and RS3 outputs of the north wall.	96
6.4	Results of the monitoring load cells and RS3 outputs of the south wall.	97
7.1	Stress-strain values. . . . .	104
7.2	Decreasing of the friction angle. . . . .	107
7.3	Updated cohesion values . . . . .	107
7.4	Mohr coulomb input parmeters (First scenario simulation). . . . .	111
7.5	Mohr-coulomb input parameters(Second scenario simulation). . . . .	111

# List of Figures

2.1	General scheme of the hydropower plant . . . . .	3
2.2	Scheme of the excavated structure . . . . .	4
2.3	Geological mapping 1 . . . . .	5
2.4	Geological mapping 2 . . . . .	5
2.5	Geological mapping of machine hall in the 6 layer . . . . .	6
2.6	Geological mapping of machine hall in the 6 layer . . . . .	6
2.7	Geological map on the foundation of the machine hall . . . . .	6
2.8	The contour plot of joint sets . . . . .	7
2.9	Distribution of rock mass classification . . . . .	9
2.10	Geological model of the powerhouse . . . . .	10
2.11	Geological model of the powerhouse(class v) . . . . .	10
3.1	Strand support . . . . .	14
3.2	Bar anchor . . . . .	14
3.3	Rock bolt . . . . .	15
3.4	Supports of powerhouse vault. . . . .	16
3.5	Shotcrete of vault. . . . .	16
3.6	Supports of upstream side wall. . . . .	18
3.7	Shotcrete of upstream side wall. . . . .	18
3.8	Support of downstream sidewall. . . . .	20
3.9	Shotcrete of downstream sidewall. . . . .	20
3.10	Support of southern ending wall . . . . .	22
3.11	Shotcrete of south Wall . . . . .	22
3.12	Support of the north end wall . . . . .	24
3.13	Shotcrete of north wall. . . . .	25
3.14	Plan view of the vault and longitudinal sections of PH. . . . .	26
3.15	Section 3-3 . . . . .	27
3.16	Section 1-1. . . . .	28
3.17	Section 2-2 . . . . .	29
3.18	Section 4-4 . . . . .	30
3.19	Multi point extensometer. [2] . . . . .	31

3.20	Load cell . . . . .	32
3.21	Installed monitoring instruments. . . . .	33
3.22	Optical targets of convergence . . . . .	33
3.23	Extensometers sections location . . . . .	34
3.24	Extensometer section A . . . . .	34
3.25	Extensometer section B . . . . .	35
3.26	Extensometer section C. . . . .	35
3.27	Extensometer section E. . . . .	36
4.1	Technical route of back analysis. . . . .	38
4.2	Simplified post-failure and tunnel behaviour.(Loren,2013) . . . . .	39
4.3	Cohesion and friction angle for different constitutive model. . . . .	40
4.4	Major and minor principal stress for Hoek-Brown and equivalent Mohr-coulombe criteria . . . . .	42
4.5	Calculation of $\sigma'_{3max}$ for equivalent Mohr-Coulombe and Hoek-Brown parameters for tunnels . . . . .	42
4.6	The parameters of rock mass when using the MC model . . . . .	43
5.1	Class V and class IV . . . . .	45
5.2	Faults . . . . .	46
5.3	Pyroclastic layers . . . . .	47
5.4	3D geological model . . . . .	48
5.5	Modification of the pyroclastic layer . . . . .	49
5.6	Intersestion between PH and BS-IV . . . . .	50
5.7	Modified class V to overcome mesh issues. . . . .	51
5.8	Primary structure. . . . .	52
5.9	Excavation contour n.1. . . . .	53
5.10	Excavation contour n.2. . . . .	53
5.11	Modified north wall. . . . .	54
5.12	Final level of details to simulate n.1. . . . .	55
5.13	Final level of details to simulate n.2. . . . .	56
5.14	Model external dimension. . . . .	57
5.15	Excavation stages. . . . .	58
5.16	First model . . . . .	59
5.17	Second model . . . . .	59
5.18	Third model . . . . .	60
5.19	Displacements in the first model. . . . .	61
5.20	Displacements in the second model. . . . .	61
5.21	Displacements in the third model. . . . .	62
5.22	Sigma 1 in first model. . . . .	62
5.23	Sigma 1 in second model. . . . .	63

5.24	Sigma 1 in third model. . . . .	63
5.25	Sigma 3 in first model. . . . .	64
5.26	Sigma 3 in second model. . . . .	64
5.27	Sigma 3 in third model. . . . .	65
5.28	Yield elements in the first model. . . . .	65
5.29	Yield elements in the second model. . . . .	66
5.30	Yield elements in the third model. . . . .	66
5.31	Final selected model. . . . .	67
5.32	Supports on the powerhouse and transform hall. . . . .	69
5.33	Rock bolts . . . . .	69
5.34	Various shotcrete sections . . . . .	70
5.35	Upstream and north wall supports . . . . .	70
5.36	South wall and down stream supports . . . . .	71
6.1	Displacements in the south and up stream wall. . . . .	73
6.2	Displacements in the north wall and down stream wall . . . . .	73
6.3	Displacements results obtained from FLAC 3D code. . . . .	74
6.4	Different sections for the presentation of the results. . . . .	75
6.5	The displacement curve of the section auxiliary PH in FLAC 3D. . . . .	76
6.6	The displacement curve of the section auxiliary PH in RS3. . . . .	76
6.7	The displacement curve of the section erection bay in FLAC 3D. . . . .	77
6.8	The displacement curve of the section erection bay in RS3 3D. . . . .	77
6.9	The displacement curve of the section PH I in FLAC 3D. . . . .	78
6.10	The displacement curve of the section PH I in RS3 3D. . . . .	78
6.11	The displacement curve of the section PH II in FLAC 3D. . . . .	79
6.12	The displacement curve of the section PH II in RS3 3D. . . . .	79
6.13	The displacement curve of the section PH III in FLAC 3D. . . . .	80
6.14	The displacement curve of the section PH III in RS3 3D. . . . .	80
6.15	The force of tendons in FLAC 3D. . . . .	81
6.16	The tendons axial force in RS3. . . . .	82
6.17	The tendons axial force in RS3. . . . .	82
6.18	Stress of rock bolts in Flac 3D. . . . .	83
6.19	Stress of rock bolts in RS3 . . . . .	84
6.20	Stress of rock bolts in RS3. . . . .	84
6.21	Plastic zones in FLAC 3D. . . . .	85
6.22	Auxiliary section Plastic zone in RS3 . . . . .	86
6.23	Erection bay section plastic zone in RS3. . . . .	86
6.24	PH I section plastic zone in RS3. . . . .	87
6.25	PH II section plastic zone in RS3. . . . .	87
6.26	PH III section plastic zone in RS3 . . . . .	88
6.27	Slice 1 section plastic zone in RS3. . . . .	88

6.28	Slice 2 section plastic zone in RS3. . . . .	89
6.29	Intersection between the PH and the bus bar tunnels. . . . .	89
6.30	Intersection between the TH and the mat. . . . .	90
6.31	The view inside the mat. . . . .	90
6.32	Load cells distribution on up stream side wall. . . . .	91
6.33	Comparison between RS3 results and Monitoring system on up stream side wall. . . . .	91
6.34	Load cells distribution on down stream side wall. . . . .	93
6.35	Comparison between RS3 results and Monitoring system on down stream side wall. . . . .	93
6.36	Load cells distribution on north and south wall. . . . .	95
6.37	Comparison between RS3 results and Monitoring system on north wall. . . . .	95
6.38	Comparison between RS3 results and Monitoring system on south wall. . . . .	97
7.1	Idealised stress-strain curves and associated states [5] . . . . .	100
7.2	Experimental relationship between rock resistance and normalized deformations. [5] . . . . .	101
7.3	Hoek-Brown and Mohr-Coulomb envelopes and definition of uniaxial and global cluster resistance [7] . . . . .	102
7.4	Stress-strain curve (BS-strong III). . . . .	103
7.5	Stress-strain curve (BS-weak III). . . . .	103
7.6	Stress-strain curve (BS-weak IV). . . . .	104
7.7	The complete stress-strain curve (LADANY1,1993). . . . .	105
7.8	Proposed model for the analysis of squeezing behaviour (Barla and Borgna,2000). . . . .	106
7.9	Mohr-Coulomb envelopes used to define stage 1 and stage 2 on the complete stress-strain curve (Barla and Borgna,2000). . . . .	106
7.10	Friction angle reduction(BS-strong III). . . . .	108
7.11	Friction angle reduction(BS-weak III). . . . .	108
7.12	Friction angle reduction(BS-weak IV). . . . .	109
7.13	width=.6height=6cm . . . . .	109
7.14	Cohesion reduction (BS weak III). . . . .	110
7.15	Cohesion reduction (BS weak IV). . . . .	110
7.16	Total displacement in south and upstream sidewall(first scenario). . . . .	112
7.17	Total displacement in south and upstream sidewall(first scenario). . . . .	113
7.18	Axial force in tendons and bar anchors(first scenario). . . . .	113
7.19	Axial stress in rock bolts(first scenario). . . . .	114
7.20	Axial stress in rock bolts(first scenario). . . . .	114
7.21	Total displacement in south and upstream sidewall(second scenario). . . . .	115

7.22	Total displacement in north wall and downstream side wall(second scenario). . . . .	115
7.23	Axial force in tendons and bar anchors(second scenario). . . . .	116
7.24	Axial force in tendons and bar anchors(second scenario). . . . .	116
7.25	Axial stress in rock bolts(second scenario). . . . .	117
7.26	Axial stress in rock bolts(second scenario). . . . .	117



# Acronyms

BS : Basalt

PYR : pyroclastic

PH : Power house

TFH : Transformed hall

LSS : Lower surge shaft

PT1 : Pilot 1

DD : Deep direction

DA : Deep angle

PL : Power left

PR : Power right

USMH : Upstream side machine hall

DSMH : Downstream side machine hall

NEMH : North end machine hall

SEMH : South end machine hall

$K_H$  : Maximum principle stress factor

$K_h$  : Minimum principle stress factor

# Chapter 1

## Introduction

The thesis is a discussion related to the back analysis of huge underground caverns belonging to a mega hydroelectric power plant. Moreover, a time-dependent analysis was performed to predict the stability of the excavated structure within the life cycle of the project and its long-term performance. The caverns were located in a complex stratigraphy which is consisted of a variety of different basalt class rock layers, faults, and pyroclastic layers.

The excavated structure consisted of two main caverns, the powerhouse and the transfer hall. The powerhouse is 97 meters long 18 meters wide and 27 meters high. the transfer hall is 76 meters long 15 meters wide and 19.5 meters high. the underground watercourse of the whole hydropower plant consisted of 6 km total length and the diameters varied between 4 and 5.5 m which distributed between different parts.

Due to the complexity of geological conditions, heterogeneity, and anisotropy of the rock mass, the data involved in the back analysis have been updated from rock mass excavation response, the monitoring data, and the last modified geological map.

All the analyses using FEM, implemented in RS3 code (Rocscience,2021) which is an efficient tool to deal with the high level of details and complexity of the stratigraphy.

In Chapter 2, the geological model and the lithology are illustrated in detail as the rock mass classification; in addition, the state of stress, the rock mass parameters, and a general overview of the project are reported. Chapter 3 describes the support and monitoring design. The back analysis technical route, the constitutive model and the parameters from the back analysis were explained in Chapter 4.

In Chapter 5, the numerical 3d models have been clarified in detail, simplifying the geological model, model geometry, excavation stages. And different loads of simulations are shown. Chapters 6 and 7, which represent the core of the thesis, the results of the back analysis. Then, the time-dependent simulation is highlighted

and the prediction method illustrated.

# Chapter 2

## Geological condition.

### 2.1 Description of study case

The study case is a hydroelectric power plant that is used to generate electricity by converting the kinetic or potential energy of water in the upper reservoir to the lower one through the water turbines. Moreover, the new innovation of the hydroelectric power plants is analyzed that they are being used as large batteries to restore the excess electric energy in the network by rising again the water from the lower reservoir to the top one. So, the hydropower plant has more sustainability compared to the ordinary electric generation methods, less environmental impact, less cost and maintenance is affordable. On the other hand, the life cycle of these hydro-power plants is around 40-50 years.

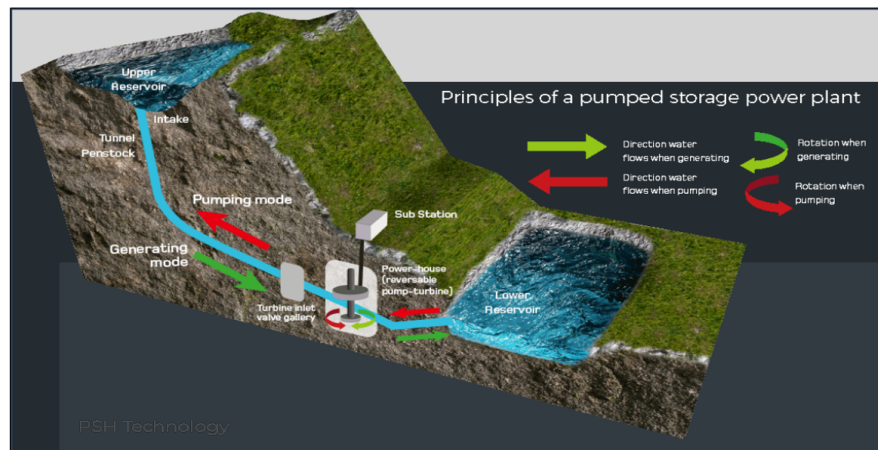


Figure 2.1: General scheme of the hydropower plant

[ili-energy.com/why-pump-storage](http://ili-energy.com/why-pump-storage)

In our case, the upper and lower reservoir's capacity is 3 million cubic meters. The excavated structure consisted of two main caverns: the powerhouse and the transfer hall. The powerhouse is 97 meters long 18, meters wide and 27 meters high. The transfer hall is 76 meters long, 15 meters wide and 19.5 meters high. The underground tunnels of the whole hydro-power plant consisted of 6 km total length and the diameters ranged between 4 and 5.5 m .

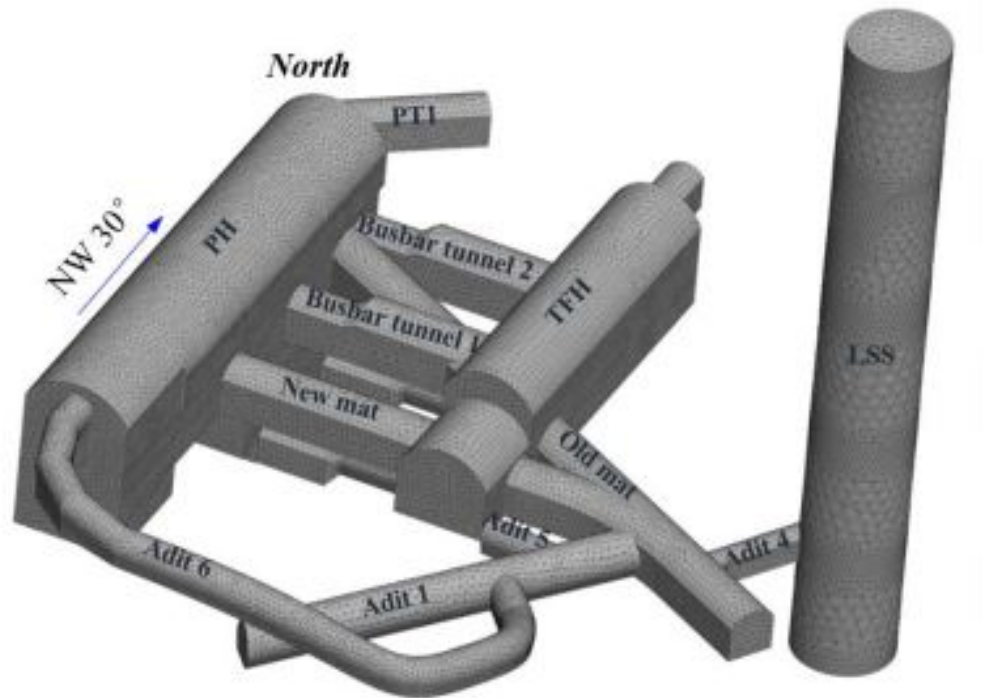


Figure 2.2: Scheme of the excavated structure

## 2.2 Geological model

### 2.2.1 Lithology

The major part of the stratigraphy is basalt which is extrusive igneous (volcanic) rock and the pyroclastic part which is formed from clastic material ejected from volcanoes.

The lithology mainly consists of 3 rock categories including the bs-strong, bs-weak, and pyroclastic layers according to the excavation and investigation borehole. The lithology distribution in the area of the powerhouse is shown in Figure 2.3 , figure

2.4 , figure 2.5 , figure 2.6, figure 2.7.

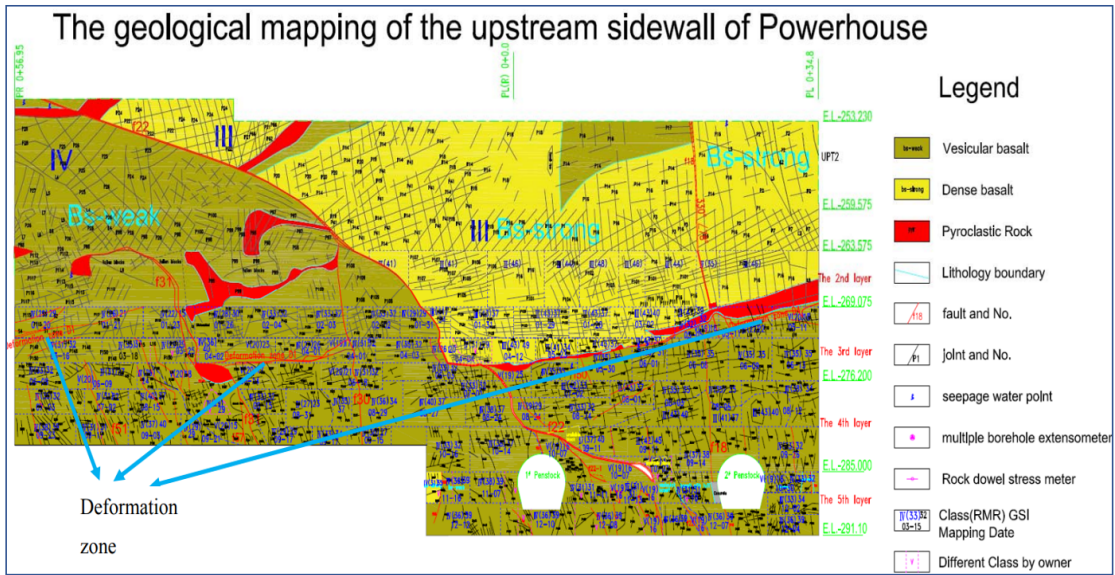


Figure 2.3: Geological mapping 1

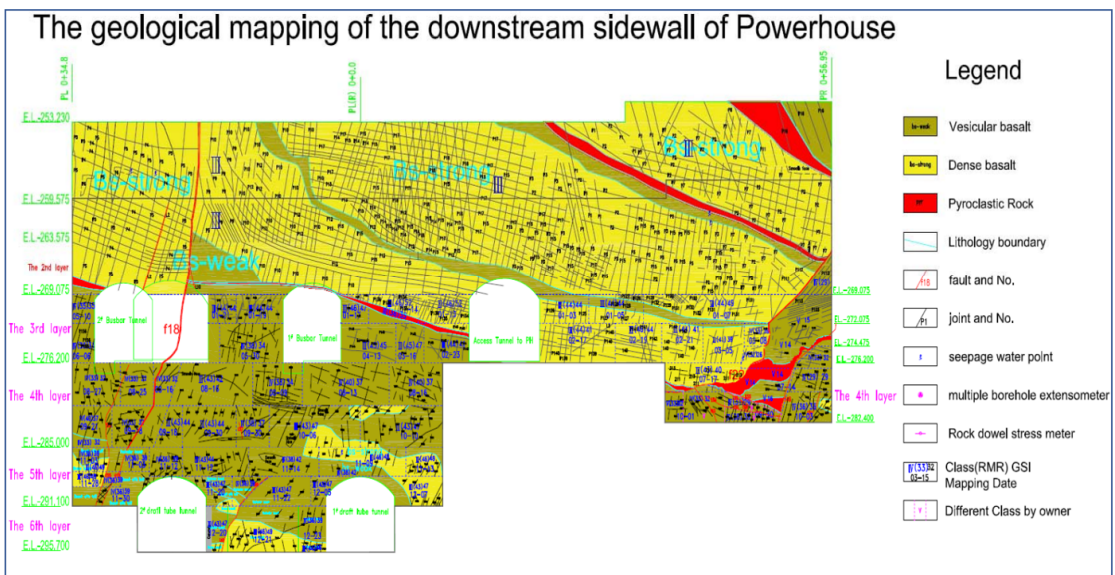


Figure 2.4: Geological mapping 2

Geological condition.

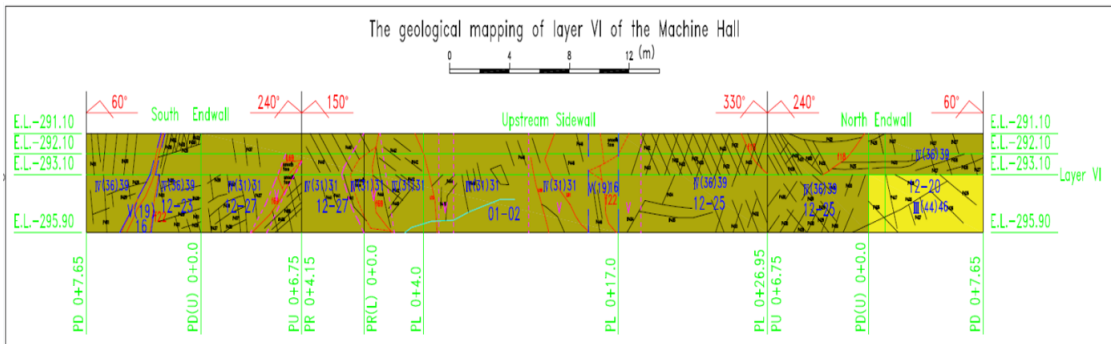


Figure 2.5: Geological mapping of machine hall in the 6 layer

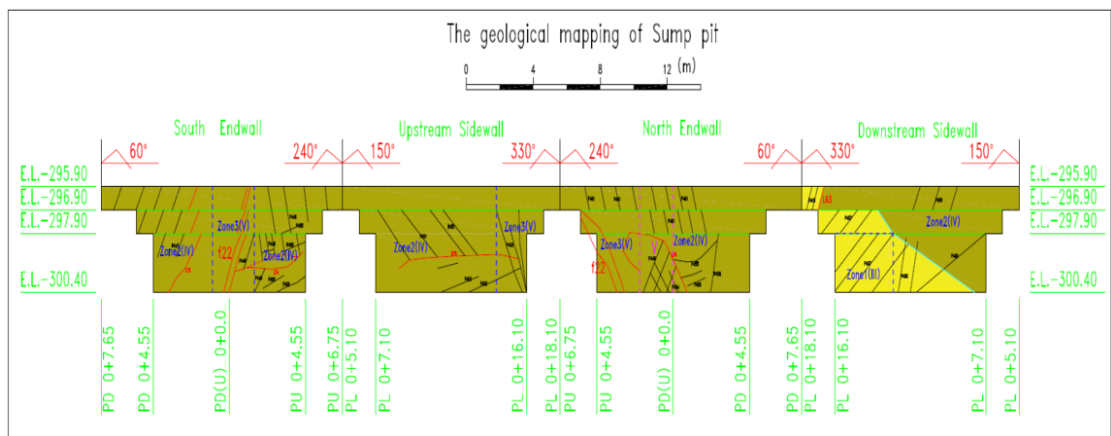


Figure 2.6: Geological mapping of machine hall in the 6 layer

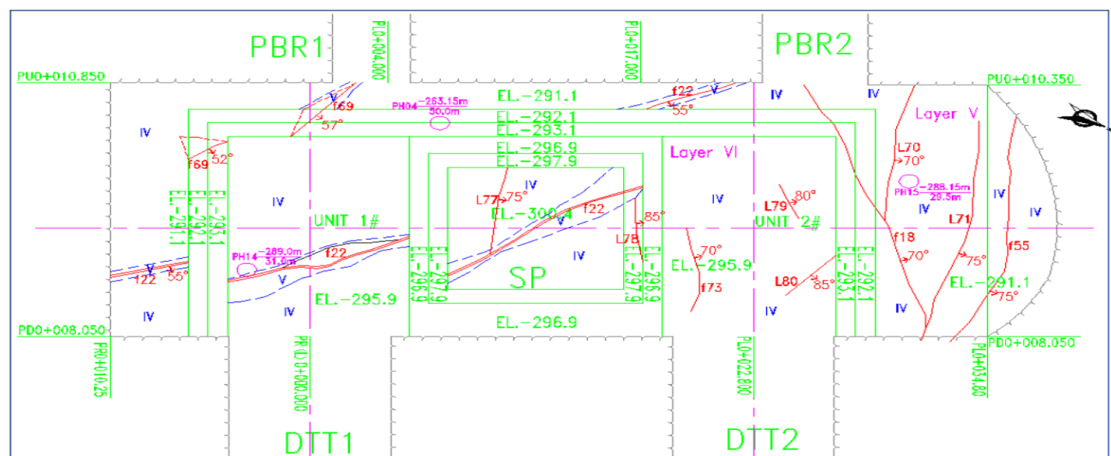
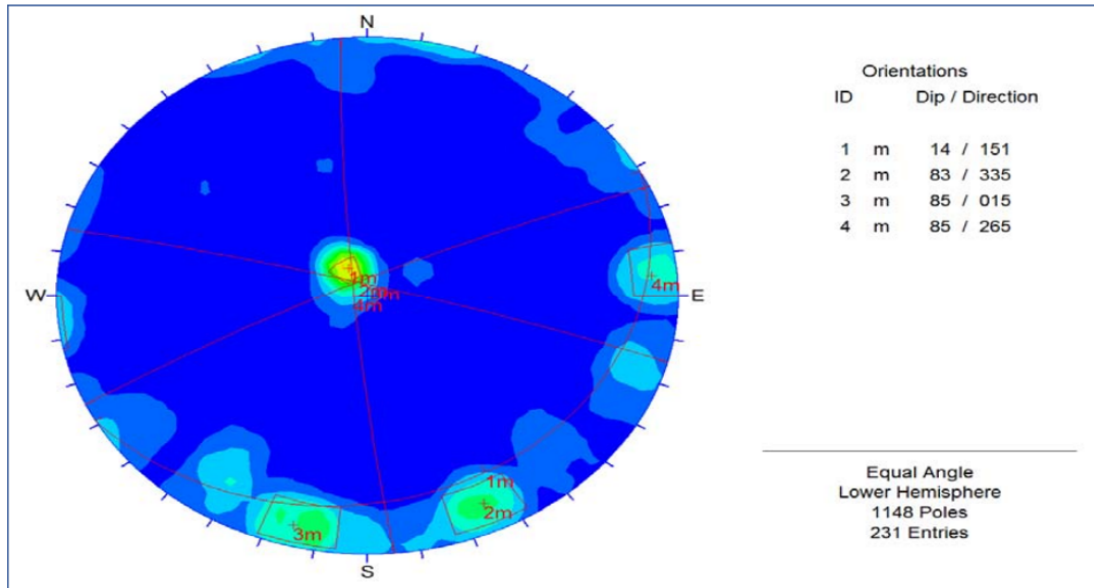


Figure 2.7: Geological map on the foundation of the machine hall

## 2.2.2 Geological structure.

Based on the latest geological information and mapping as shown in Figures 2.3 2.4 2.5 2.6 2.7. The zone where our structure is located consists of different intersecting faults and different deformation digging zones. The detailed information of the faults and deformation zones is shown in Table 2.1

The contour plot is shown in figure 2.8 Based on the information of joints exposed in the powerhouse.



**Figure 2.8:** The contour plot of joint sets

The following sets of dominant joints are observed:

- 1) 151° / 14°, spacing 0.2-0.6m, flat rough-smooth, close-slightly open, extension longer.
- 2) 335° / 83°, spacing 0.2-0.4m, flat rough-smooth, slightly open, chlorination, extension longer.
- 3) 015° / 85°, spacing 0.2-0.4m, flat rough, slightly open, chlorination, extension longer.
- 4) 265° / 85°, spacing 0.2-0.4m, flat rough-smooth, slightly open, chlorination, extension longer.

**Table 2.1:** Summaries of faults and deformation zones

No.	Azimuth(Deg)		Width(m)	Exposed section	Filling
	DD	DA			
f18	322-330	65-78	0.05-0.15	Upstream PL 21.5-22.5	gouge, breccia
f22	15-30	40-65	0.02-0.1	normal Upstream PR1.1-8.5	gouge,
f22-1	10-20	50-60	0.08-0.1	Upstream PL4.5-11.0	Rock debris, gouge
f30	15-20	70-9	0.3-0.5	Upstream PR17.0-19.5	gouge,
f31	5-10	70-80	0.3-0.5	Upstream PR31.0-38.5	gouge,
f46	15-25	60-70	0.05-0.15	Upstream PR50.5-57.0	–
f50	270-280	70-80	0.01-0.05	Upstream PL7.5-8.5	Gouge,
f51	320-330	80-90	0.02-0.05	Upstream PR48.0-49.0	Gouge,
f55	340-350	80-90	0.01-0.02	Downstraem PL 27.5-31.0	Rock debris
f57	65-70	75-80	0.01-0.02	Upstream PR30.0-32.0	Rock debris, gouge
f62	100-110	60-70	0.01-0.02	Downstraem PR40.0-44.0	Rock debris, gouge
f65	0-10	70-80	0.05-0.10	NEP PU 2.0-3.0	Rock debris, green mineral
f66	165-180	65-85	0.05-0.10	Upstream PR 8.0-10.0	Rock debris, green mineral
f67	350-360	80-85	0.05-0.10	SEMH PU 8.0-9.0	Rock debris, green mineral
f69	30-40	55-60	0.005-0.01	USMH PL 1.0-PR 2.0	Rock debris
f73	320-330	65-75	0.005-0.01	Floor of Unit2#	Rock debris
D1	160-200	8-15	0.10-0.50	Upstream PR 56.95- 42.0,	Rock debris
D4	130-150	15-20	0.10-0.50	Upstream PL10.0-34.8	Rock debris

### 2.2.3 Rock classification.

The attribution of the rock mass area classification has been represented in table 2. Mainly classes of rock mass are divided between class III around 20%, class IV around 70%, and class V around 10%.

**Table 2.2:** The proportion of each rock mass class

Location	Fair(III)		Poor(IV)		Very Poor(V)	
	area(m <sup>2</sup> )	percentage	area(m <sup>2</sup> )	percentage	area(m <sup>2</sup> )	percentage
USMH	0	0%	139.68	94%	9.6	6%
DSMH	69.4	58%	49.95	42%	0	0%
NEMH	21.42	18%	81.27	70%	14.68	12%
SEMH	0	0%	99.42	85%	17.95	15%
Total	90.82	18%	370.32	74%	42.23	8%

The allocation of the rock mass classification that has been excavated is shown in figure2.9.

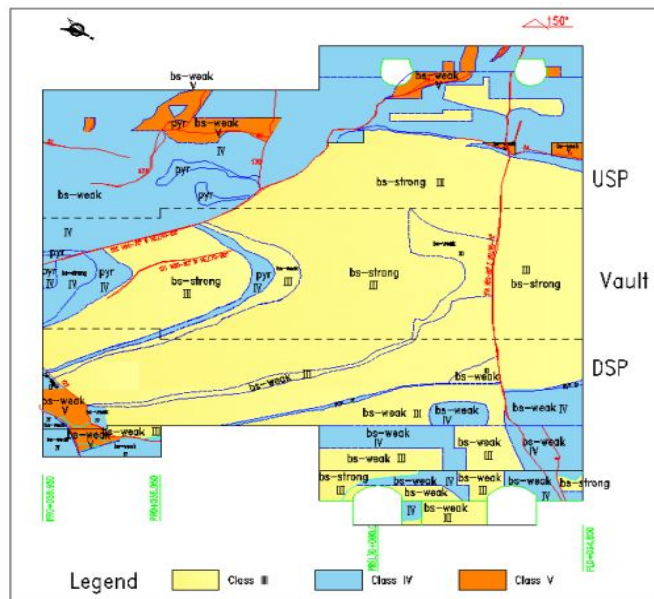


**Figure 2.9:** Distribution of rock mass classification

## 2.2.4 Geological Model

Based on the latest investigation of the powerhouse and the geological information, the main rock formation is the bs-strong between the pyroclastic layers number 3, 6, and 9. The bs-weak is located below the pyroclastic layer number 9 as shown in the figure2.10. In the end, a general overview related to the class v with the excavated structure is shown in figure2.11

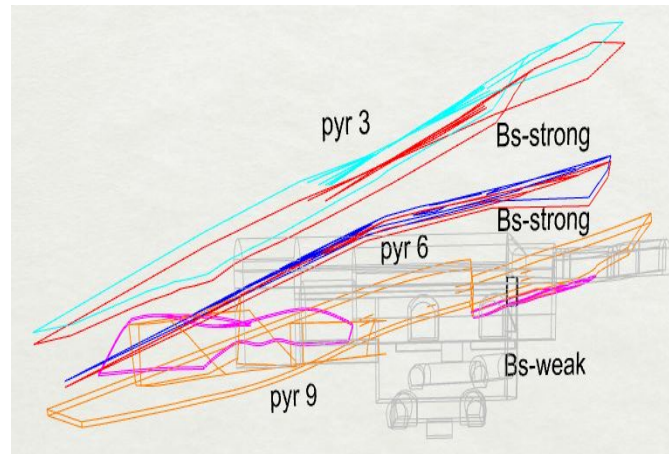


**Figure 2.10:** Geological model of the powerhouse

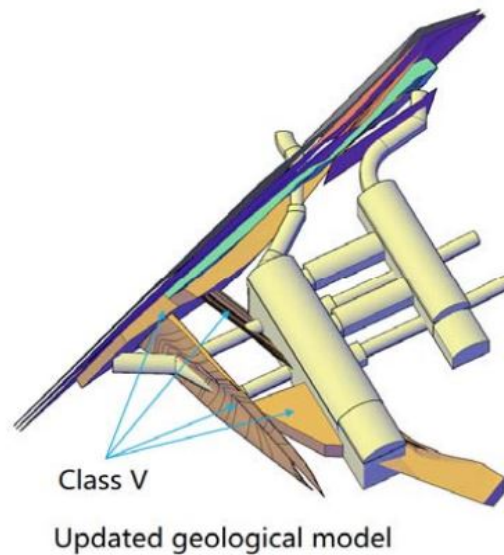


**Figure 2.11:** Geological model of the powerhouse(class v)

## 2.3 In-situ stress

The in-situ stress used in the back analysis is the same as the design phase. The vertical stress is assumed 10 MPa,  $k_H = 1.5$  and  $K_h = 0.7$ .

The orientation of the major principal stress is approximately N11 °W, while the direction of the minor principal stress is N79 °E.

**Table 2.3:** Magnitude and orientation of principal stress components.

Stress components	Magnitude MPa	Dip [Deg]	Dip dir [Deg]
1	15	0	349N
2	10	90	–
3	7	0	79N

## 2.4 Suggested parameters for rock mass

The input parameters for the Hoek-Brown failure criterion of the rock mass are illustrated in the table 2.4. Laboratory tests have been taken to prove there is no overestimation of the rock mass parameters. The GSI classification is correlated to the updated version of the geological mapping and back analysis results. With respect to the faults, the suggested geological parameters are shown in the table??.

**Table 2.4:** Hoek-Brown failure parameters data.

Lithology	Rock classification	UCS(MPa)	GSI	mi
bs-strong	III	101.3	45	25
	III	50.81	43	25
bs-weak	IV	33.9	39	20
	IV	16.6	18	20
pyroclastic	IV	8.8	34	12

**Table 2.5:** Input data for faults

fault zone	Description	Mohr-coulomb parameters	
		c(MPa)	$\phi$ (Deg)
faults	Filling :clayey basaltic breccia	0.1	23

## Chapter 3

# Support and monitoring design

### 3.1 Support elements and monitoring devices

#### 3.1.1 Rock bolt

A rock bolt or cable bolt consists of a bar inserted in a borehole that is drilled into a soil or rock mass and anchored to it by means of a fixture (Windsor, 1992, Windsor and Thompson, 1996). Fully grouted bolts comprise four elements: the bar, the surrounding ground, the internal fixture to the borehole wall, and the external fixture to the excavation surface. The main characteristic of fully grouted bolts is that they only provide support action if the surrounding ground tries to deform; thus, they are passive reinforcement systems (Tincelin and Fine, 1991)[1]. The ground conditions affect the rock bolt Length and bolt pattern. Several tests like the pull-out test and torque test have to be done to determine the strength and capacity of the bolts.

#### 3.1.2 Bar anchors and tendons

Bar anchors have three main components; unbonded length (free stressing), bond length, and anchor head(anchorage). They are an active system that transfers a prestressing load to the ground to control or set a limit to the deformations. Bar anchors can be used with many geo applications such as slope stabilization, dam construction, and underground constructions. Moreover, strand or bar anchors could be classified based on their service life, in our case, it is a permanent application for more than 2 years.

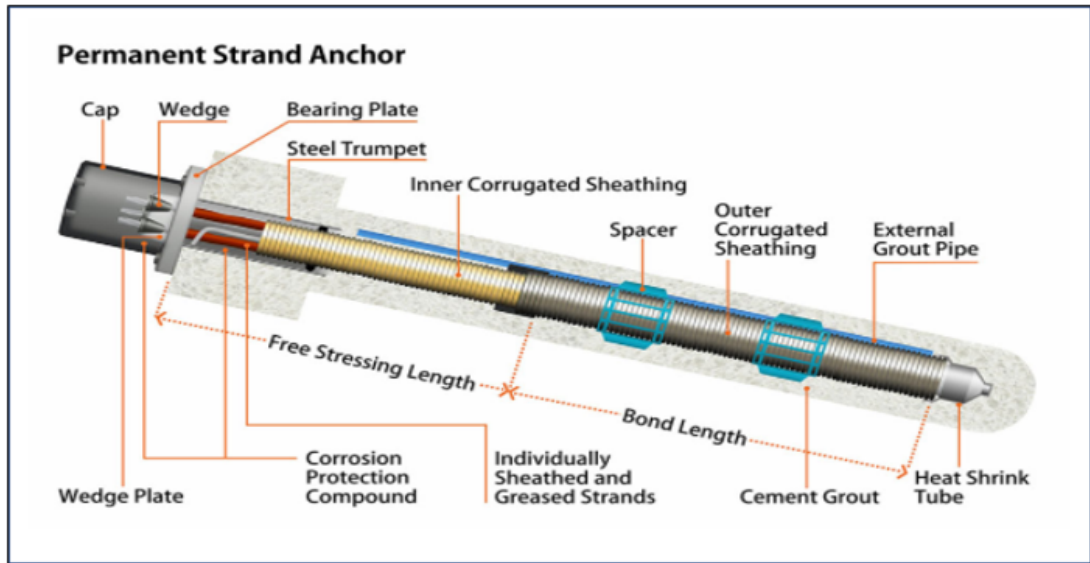


Figure 3.1: Strand support  
<https://forcetecgroup.com/strand-anchors/>

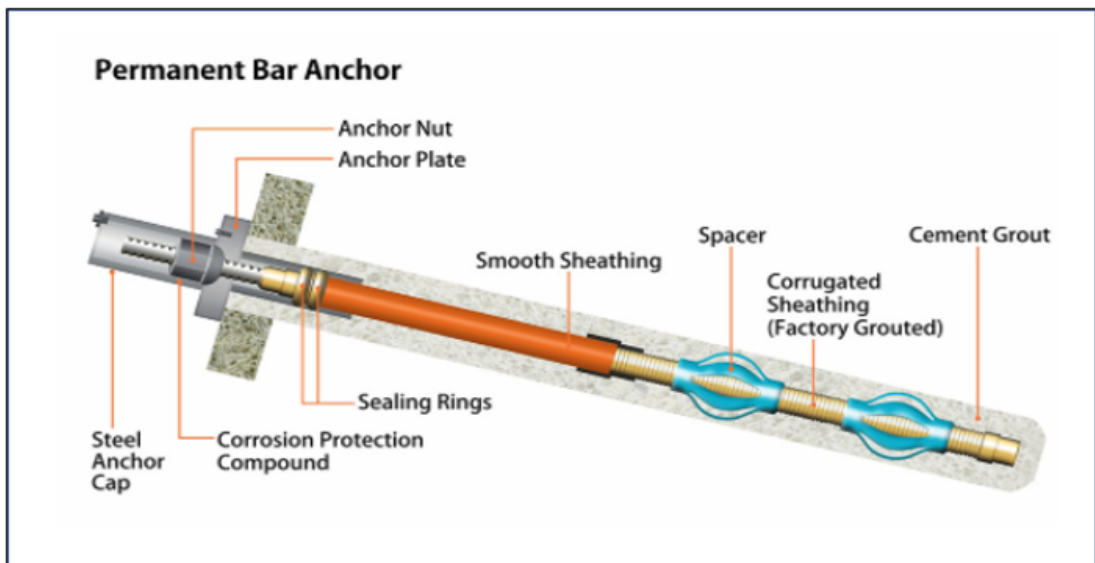


Figure 3.2: Bar anchor  
<https://forcetecgroup.com/bar-anchors/>

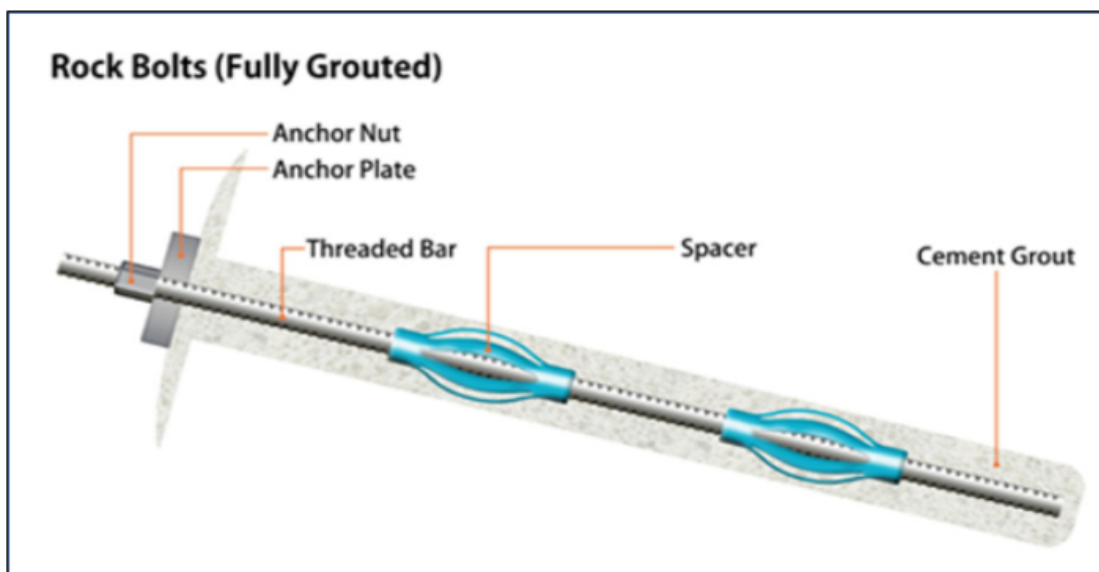


Figure 3.3: Rock bolt  
<https://forcetecgroup.com/rock-bolts/>

## 3.2 Support design

The designed support elements related to the powerhouse and the transformed hall are summarized in detail in the coming figures and tables.

### 3.2.1 Vault

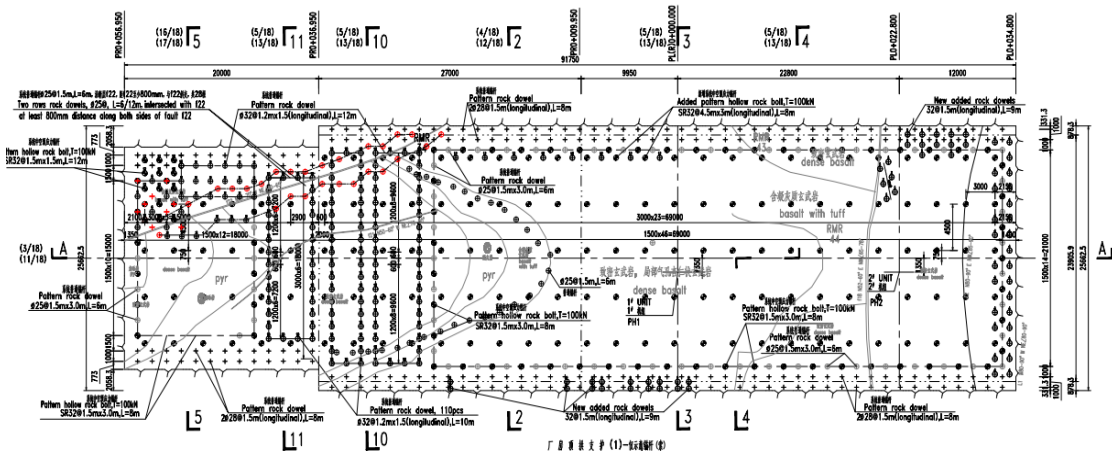


Figure 3.4: Supports of powerhouse vault.

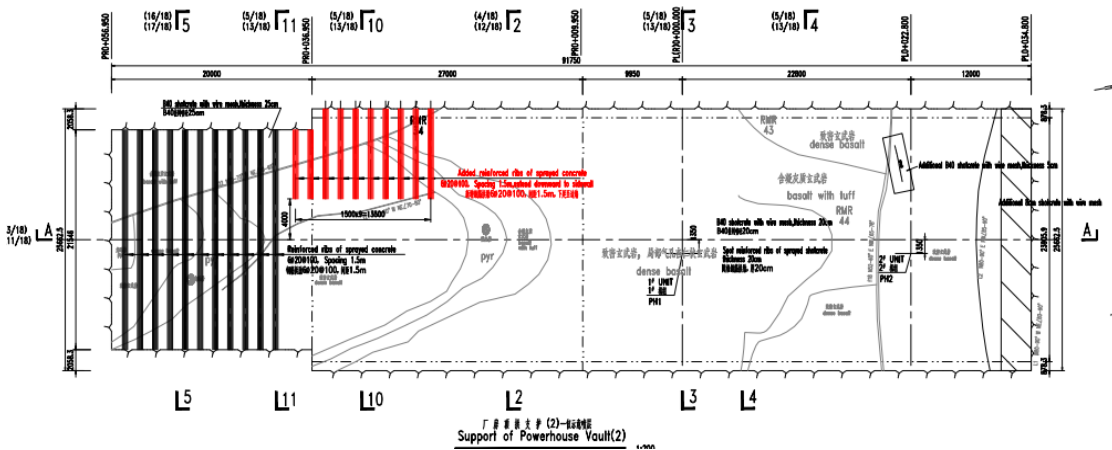


Figure 3.5: Shotcrete of vault.

**Table 3.1:** Supports of powerhouse vault.

positon	Support parameters	
	Powerhouse	Transform Hall
vault	1. pattern rock dowel, 25@1.5mx3m,L=6m	1. pattern rock dowel, 25@1.5mx3m,L=4m
	2. rock dowel in local area, .32@1.5mx1.2m,L=10/12m	2. rock dowel in local area, 32@1.5mx1.5m,L=10m
	3. pattern hollow rock bolt: R32@1.5mx3m,L=8m,T=100kN	3. pattern hollow rock bolt: SR32@1.5mx3m,L=8m,T=100kN
	4. 20cm shotcrete with wire mesh, 25cm with double wire mesh for vault of auxiliary PH	4. 12cm shotcrete with wire mesh

### 3.2.2 Upstream side wall

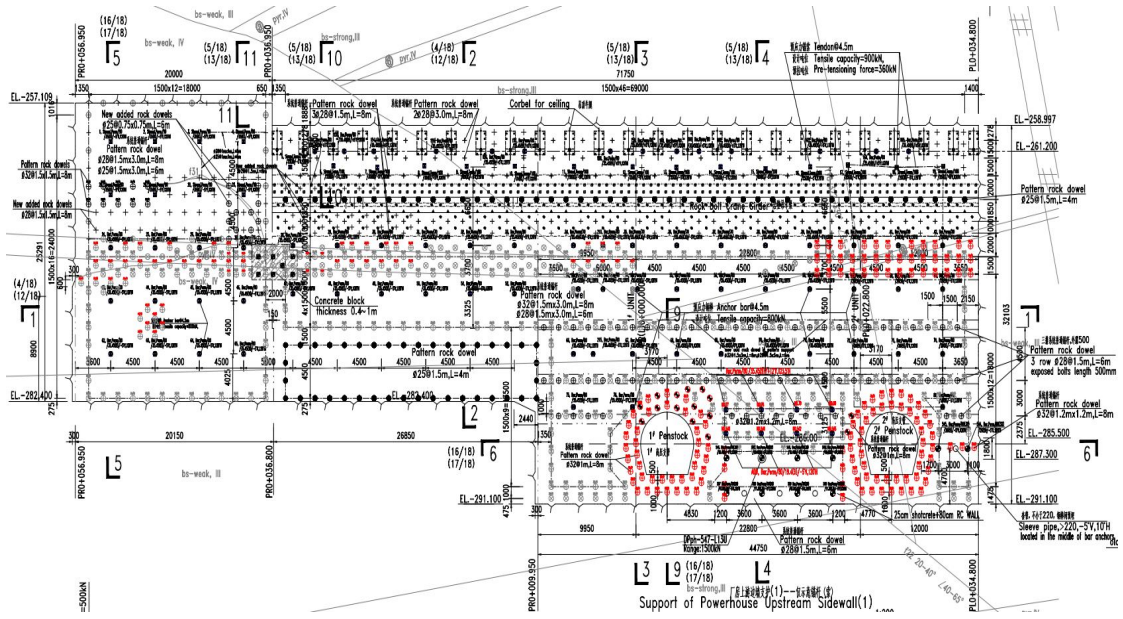


Figure 3.6: Supports of upstream side wall.

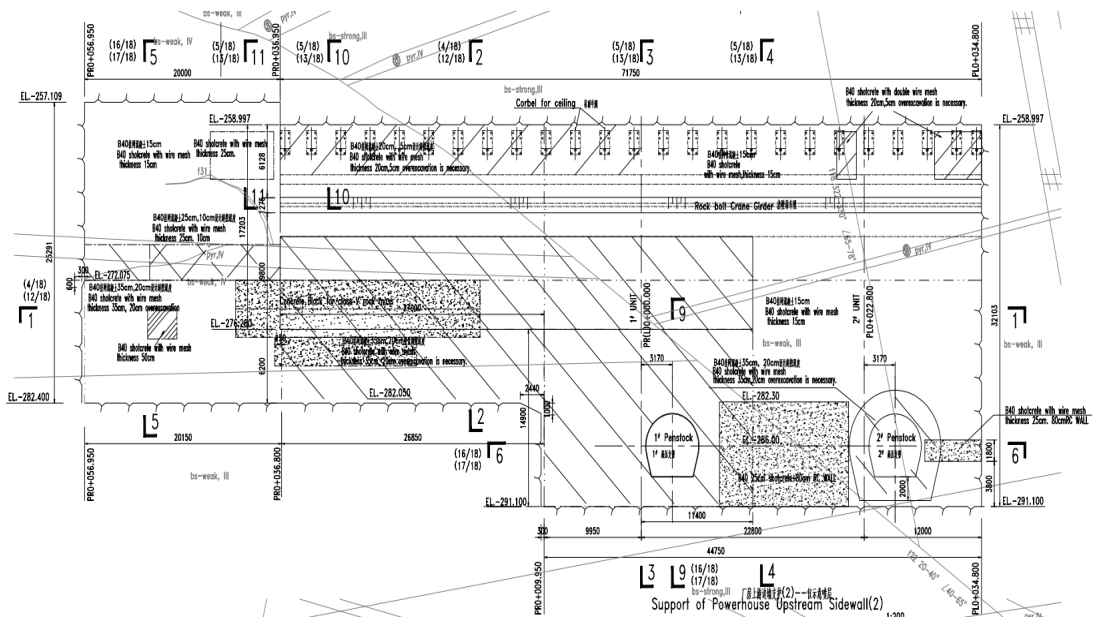


Figure 3.7: Shotcrete of upstream side wall.

**Table 3.2:** Support of upstream sidewall.

position	Support parameters	
	Powerhouse	Transform Hall
UP Stream	1. pattern rock dowel, $a28@1.5m \times 3m, L=6m$	1. pattern rock dowel, $a25/28@1.5m \times 1.5m, L=4/6m$
side wall	2. pattern rock dowel, $32@1.5m \times 3m, L=8m$	2. shotcrete with wire mesh, 12cm
	3. shotcrete with wire mesh 20/35cm with double wire mesh.	3. Upstream wall between busbar tunnels:
	4. pattern tendon@3m/4.5m, $L=25/35m$ , Tensile capacity=900kN, Pre-tensioning force=360KN	bar anchor, $L=26m$ , service capacity 800kN, prestressed force 320kN bar anchor, $L=10m$ , service
	5. pattern bar anchor@3m/4.5m with waler beam, $L=26/35.45m$ , Tensile capacity=800kN, Pre-tensioning force=50KN	capacity 500kN, prestressed force 100kN
	6. Class V rock mass: 80cm concrete lining+25cm shotcrete lining	

### 3.2.3 Downstream side wall.

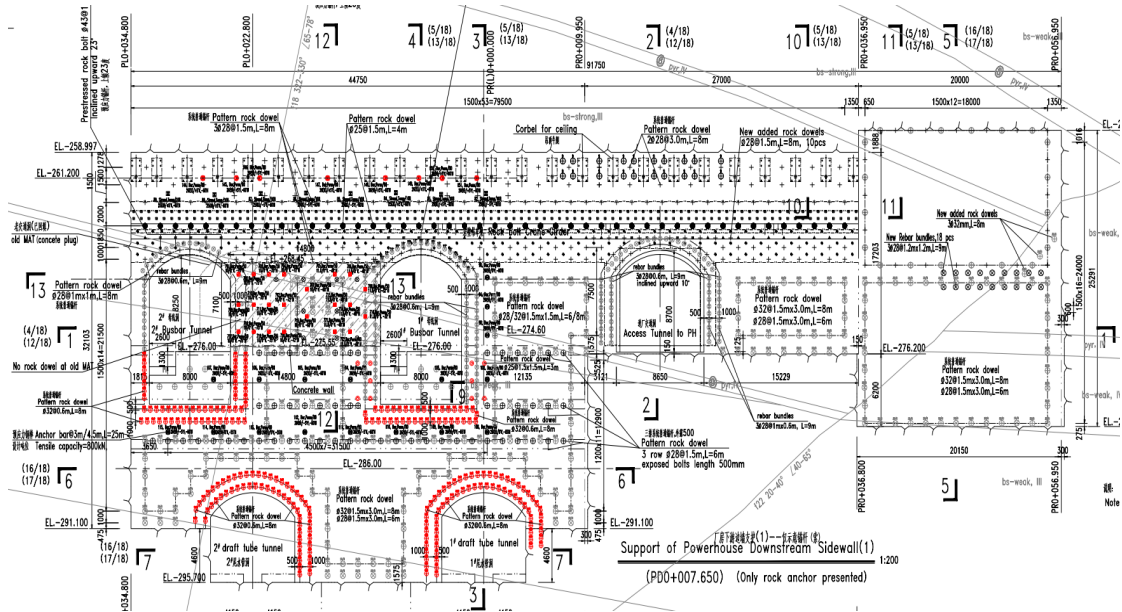


Figure 3.8: Support of downstream sidewall.

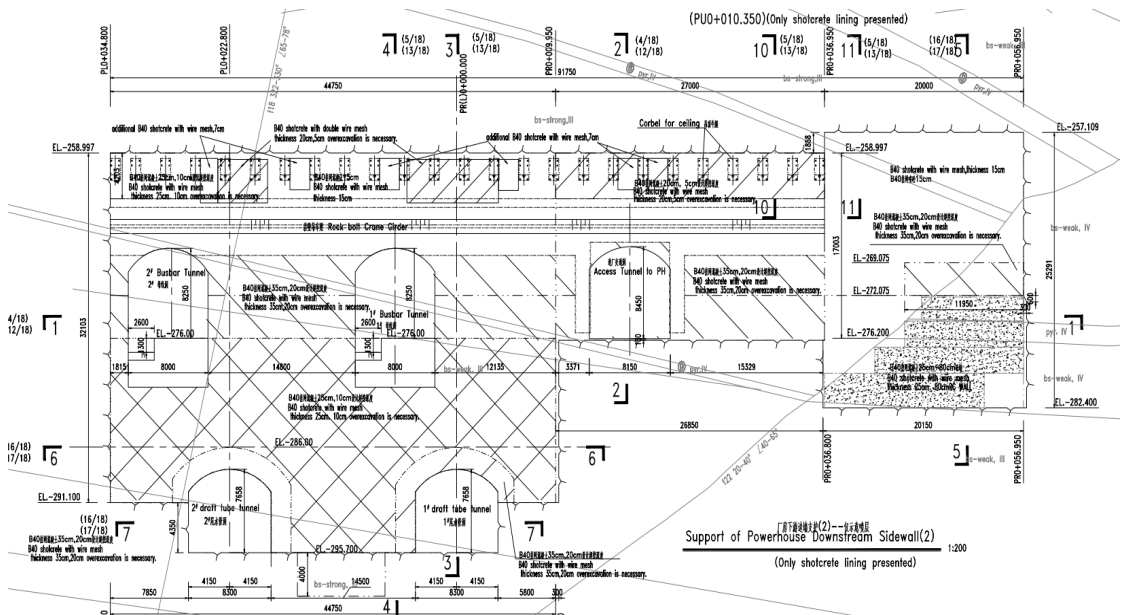


Figure 3.9: Shotcrete of downstream sidewall.

**Table 3.3:** Support of downstream sidewall.

position	Support parameters	
	Powerhouse	Transform Hall
Down stream	1. pattern rock dowel, a28@1.5mx3m,L=6m	1. pattern rock dowel, a25/28@1.5mx1.5m,L=4/6m
side wall	2. pattern rock dowel, .32@1.5mx3m,L=8m	2. Local rock dowel, 25/28@1.5mx1.5m,L=6/8m
	3. shotcrete with wire mesh: 15cm,25cm and 35cm with double wire mesh	3. shotcrete with wire mesh, 12cm
	4. pattern tendon@3m/4.5m,L=25m,Tensile capacity=900kN, Pre-tensioning force=360kN	
	5. pattern bar anchor@3m/4.5m with waler beam,L=26m,Tensile capacity=800kN, Pre-tensioning force=50KN	
	6. Bar anchor, L=10m,service capacity 500kN,prestressed force 50KN	

### 3.2.4 Southern ending wall.

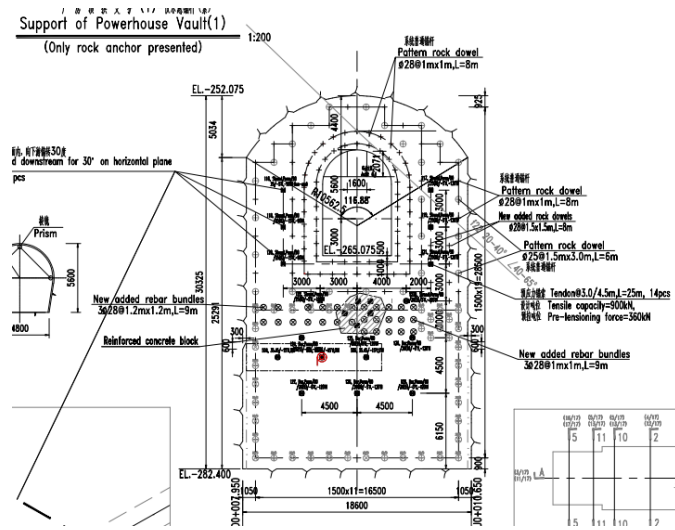


Figure 3.10: Support of southern ending wall

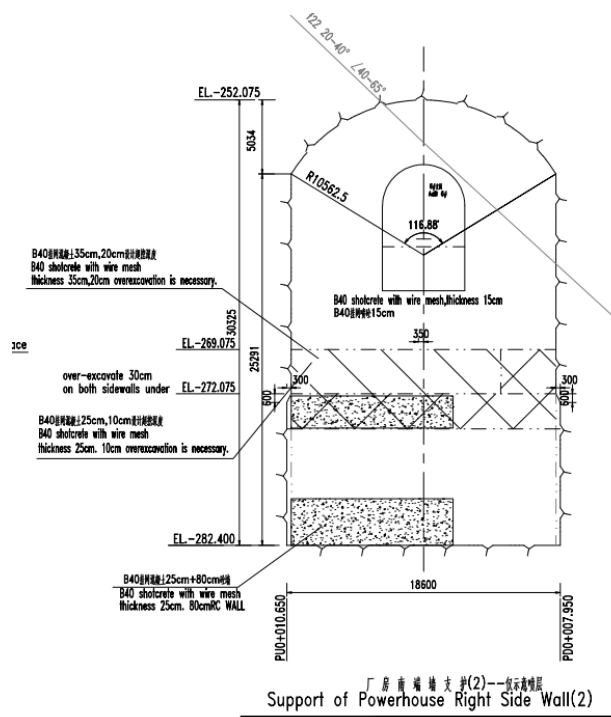


Figure 3.11: Shotcrete of south Wall

**Table 3.4:** Support of south ending wall.

positon	Support parameters	
	Powerhouse	Transform Hall
south ending wall	1. pattern rock dowel, .28@1.5mx3m,L=6m	1. pattern rock dowel, a25@1.5mx1.5m,L=4/6m
	2. pattern rock dowel, 32@1.5mx3m,L=8m	2. shotcrete with wire mesh, 12cm
	3. shotcrete with wire mesh, 15cm	
	4. Pattern tendon@3/4.5m,L=35m,Tensile capacity=900kN, Pre-tensioning force=360Kn	
	5. Pattern bar anchor@3m/4.5m,L=26/35.45m,Tensile capacity=800kN, Pre-tensioning force=50KN	
	6. Class V rock mass: 80cm concrete lining+25cm shotcrete lining	

### 3.2.5 Northern ending wall.

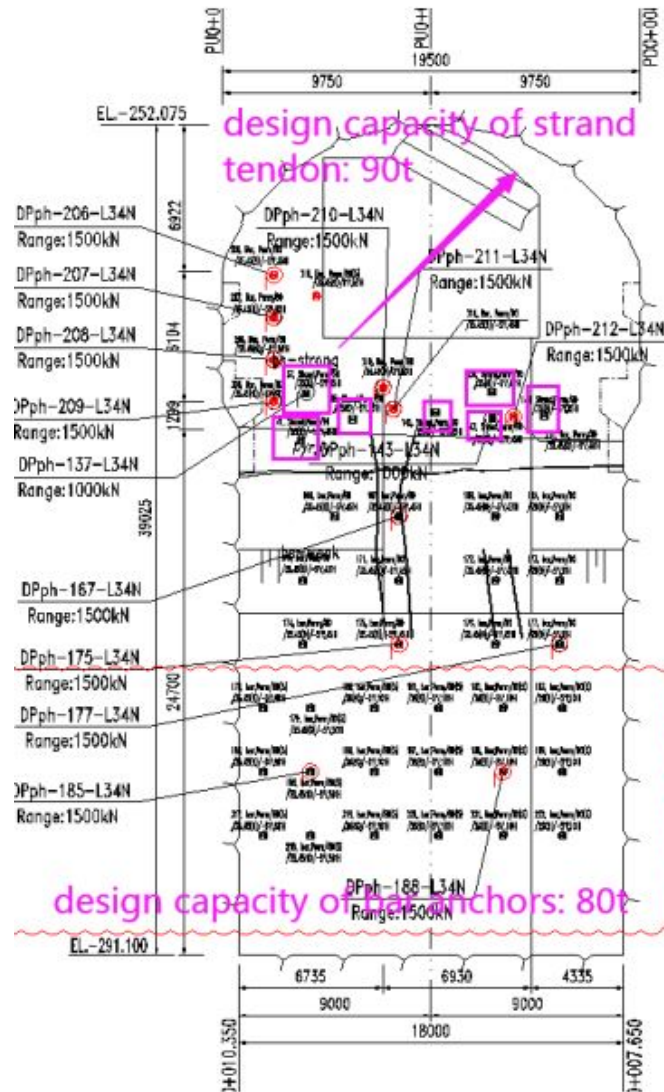


Figure 3.12: Support of the north end wall

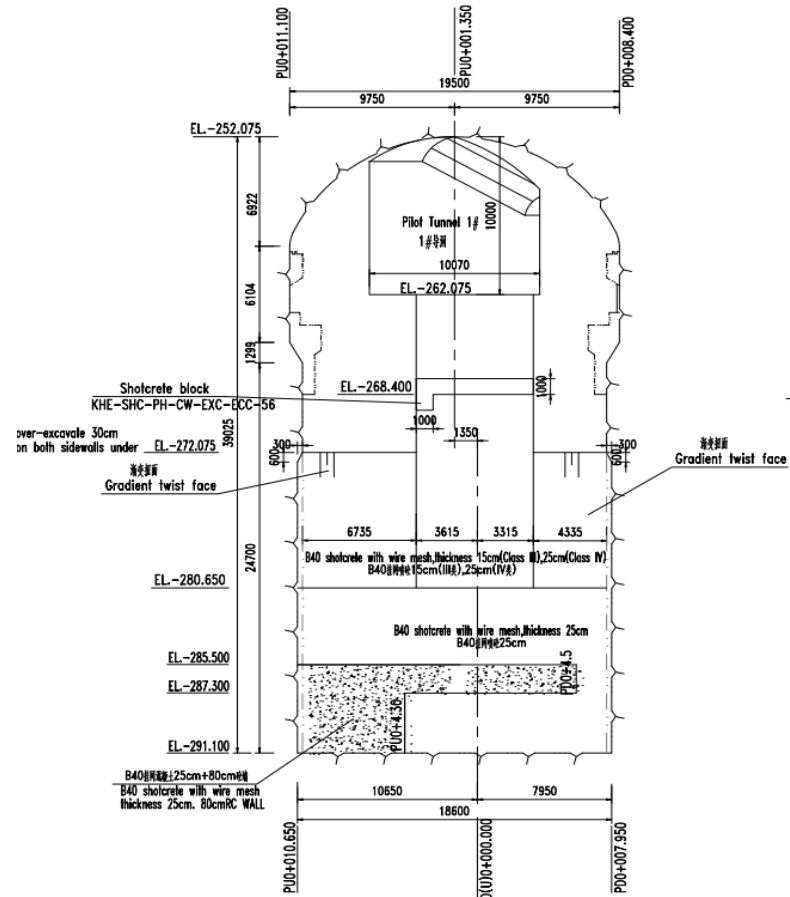
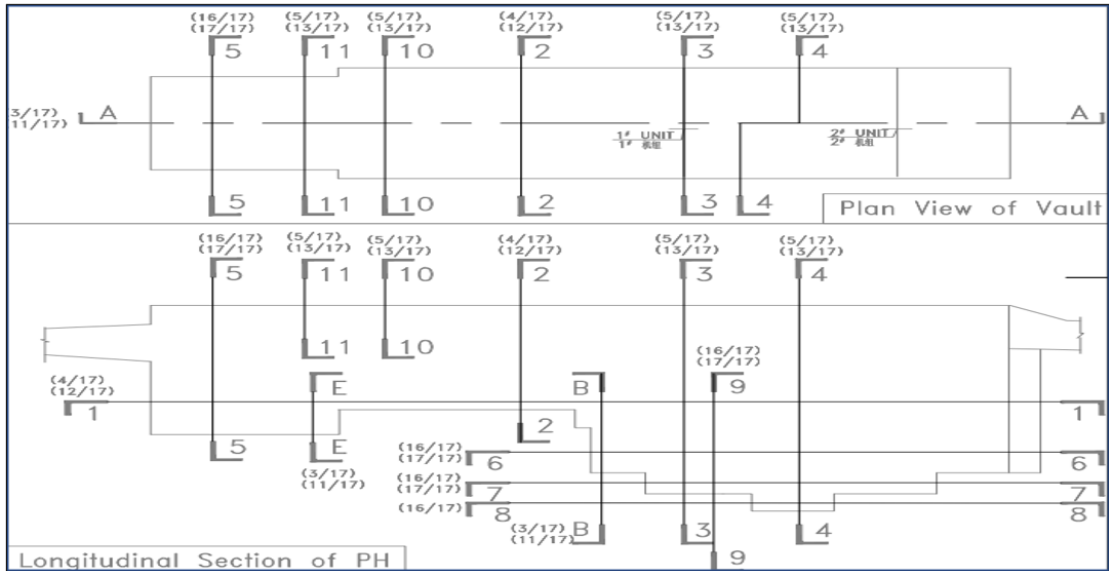


Figure 3.13: Shotcrete of north wall.

**Table 3.5:** Support of the north wall

position	Support parameters	
	Powerhouse	Transform Hall
North End wall	1. pattern rock dowel, .28@1.5mx3m,L=6m	1. pattern rock dowel, a25/28@1.5mx1.5m,L=4/6m
	2. pattern rock dowel, 2@1.5mx3m,L=8m	2. shotcrete with wire mesh, 12cm
	3. shotcrete with wire mesh, , 15cm	
	4. Pattern tendon@3/4.5m,L=35m,Tensile capacity=900kN, Pre-tensioning force=360Kn	
	5. Pattern bar anchor@3m/4.5m,L=26/35.45m,Tensile capacity=800kN, Pre-tensioning force=50KN	



**Figure 3.14:** Plan view of the vault and longitudinal sections of PH.



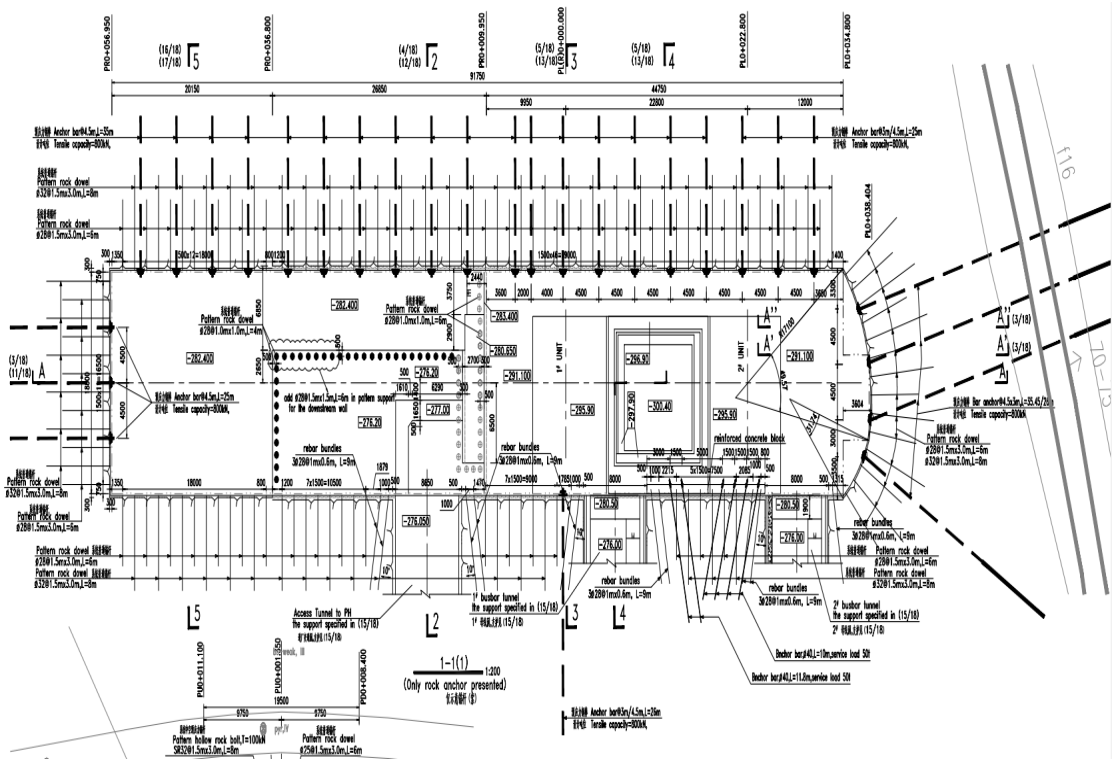


Figure 3.16: Section 1-1.

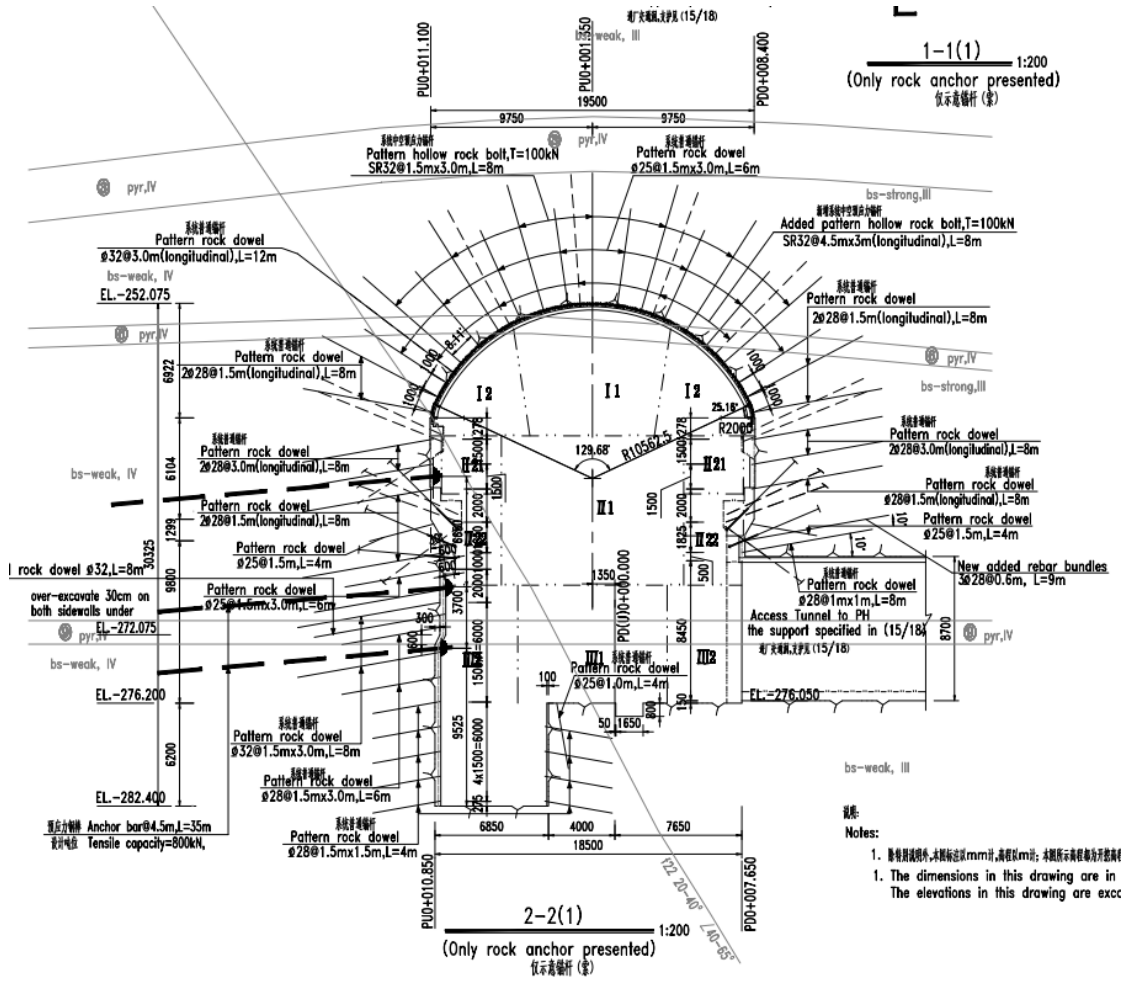


Figure 3.17: Section 2-2

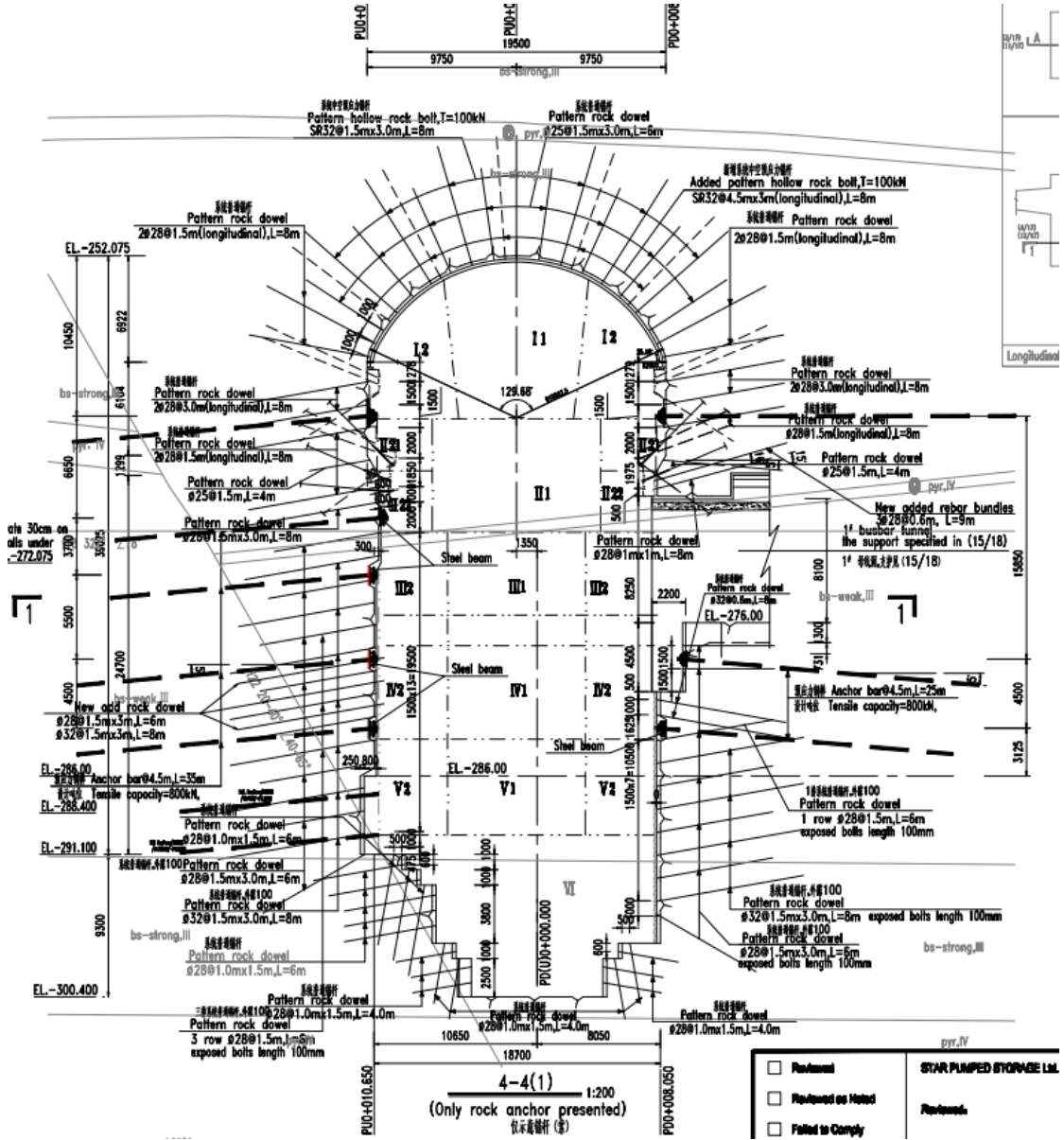


Figure 3.18: Section 4-4

### 3.3 Monitoring Design

#### 3.3.1 Extensometers and load cells

Extensometer measures the relative displacement between two or more points along the line, by installing multiple anchors at different depths.

It is used to monitor landslides, tunnels, dams. With respect to the load cell, it measures load or pressure inside a structural element, in which it is inserted, and monitors anchors, linings, concrete structures, etc.

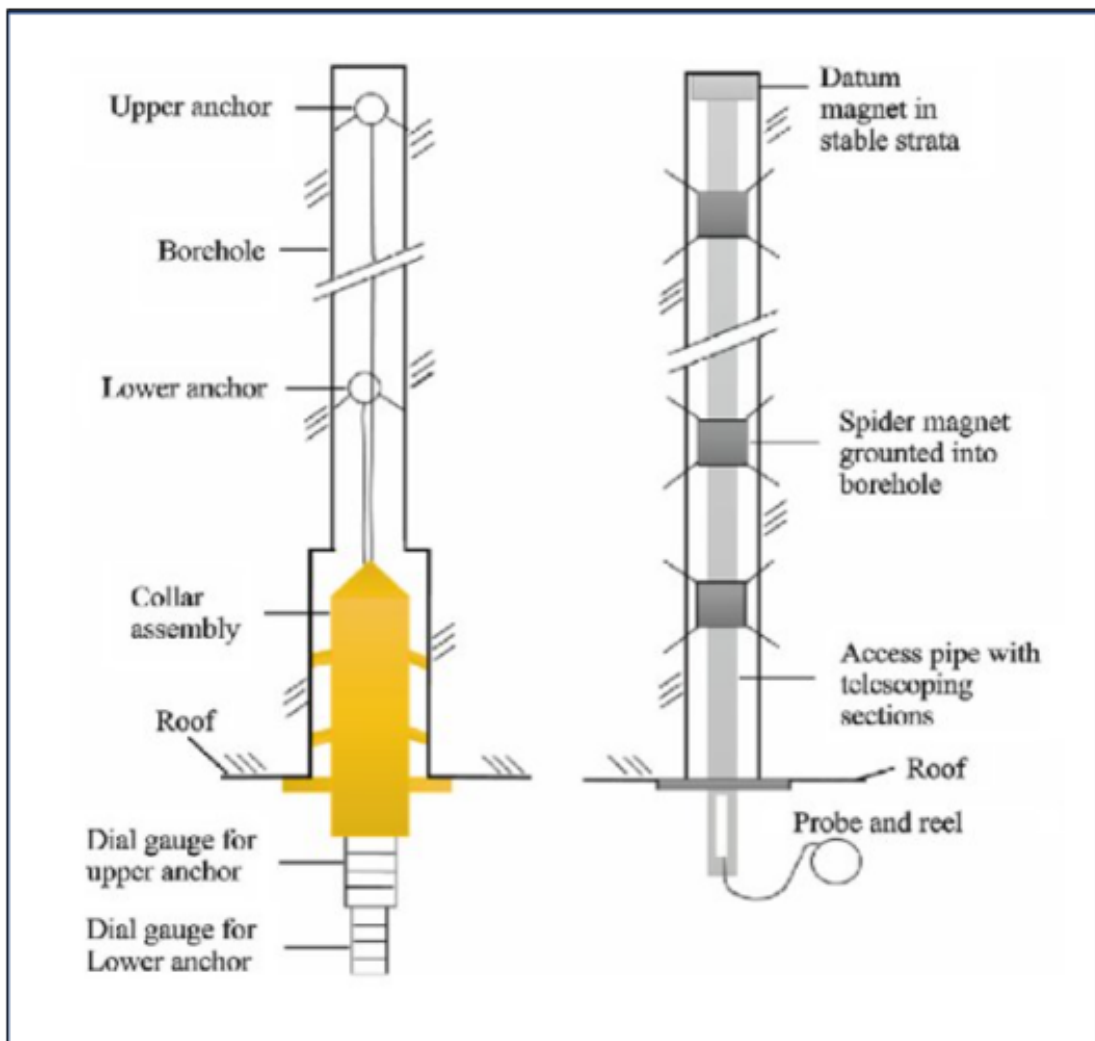


Figure 3.19: Multi point extensometer.

[2]



**Figure 3.20:** Load cell  
[earthsystem.it/product/anchor-load-cell-2/](http://earthsystem.it/product/anchor-load-cell-2/)

### 3.3.2 Monitoring system

The installed extensometers, load cells, and stress meters are illustrated in the figure3.21. Furthermore, the optical target is shown in the figure3.22.

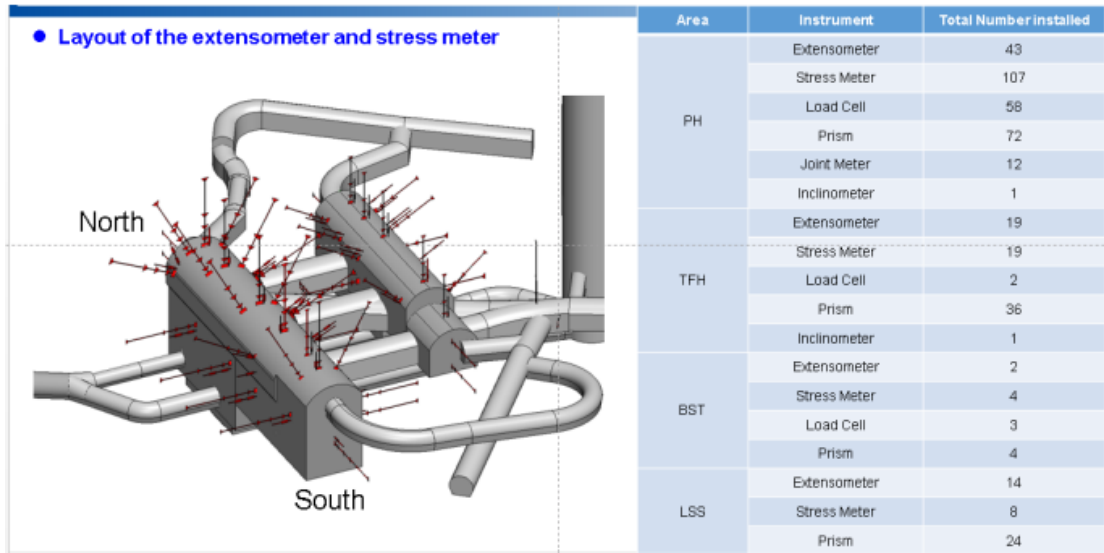


Figure 3.21: Installed monitoring instruments.

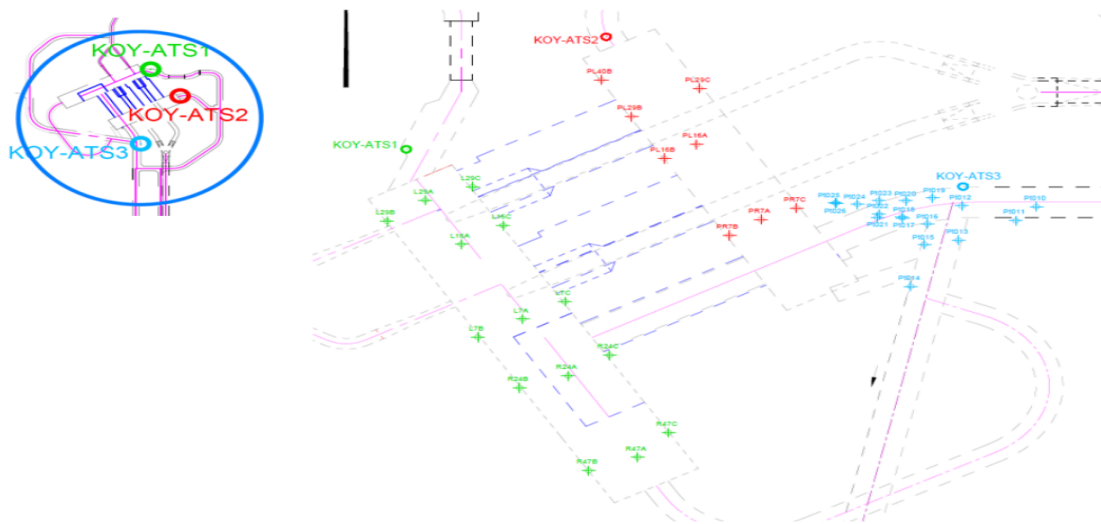


Figure 3.22: Optical targets of convergence

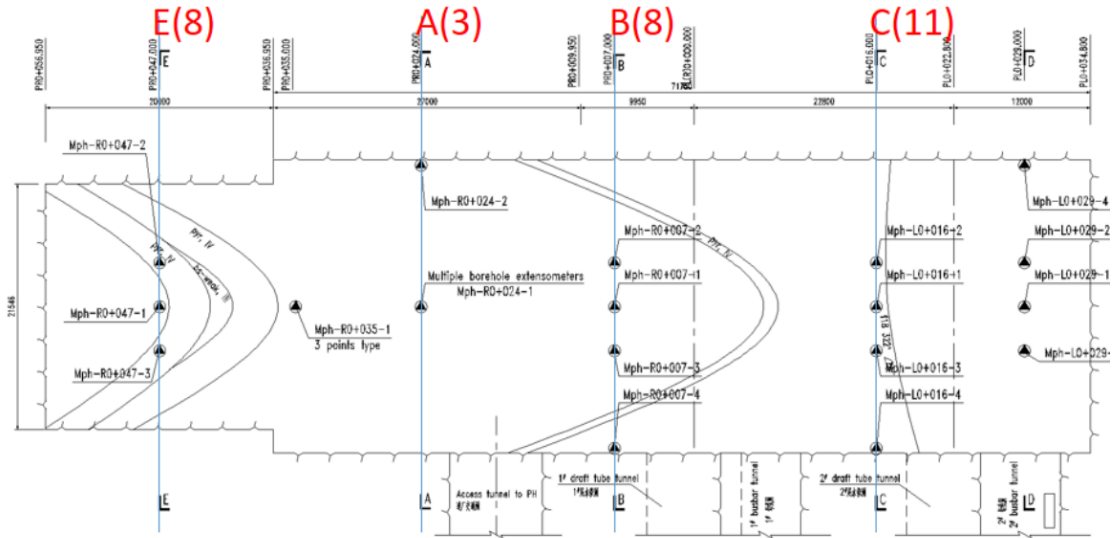


Figure 3.23: Extensometers sections location

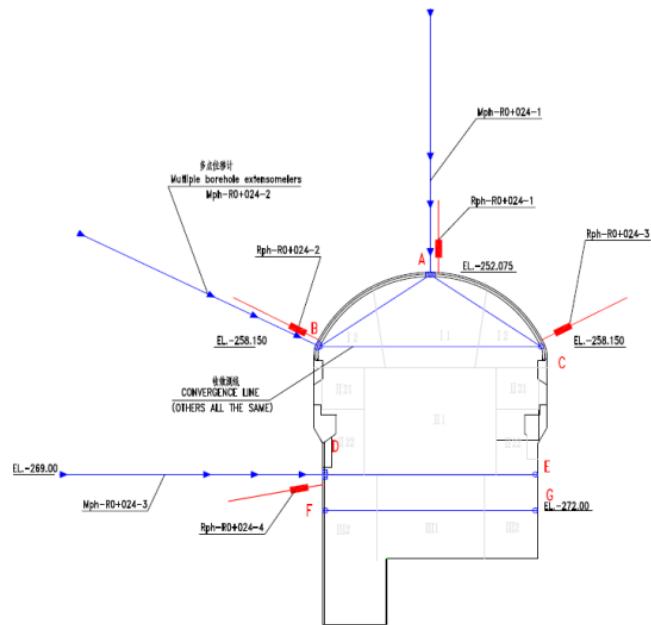


Figure 3.24: Extensometer section A



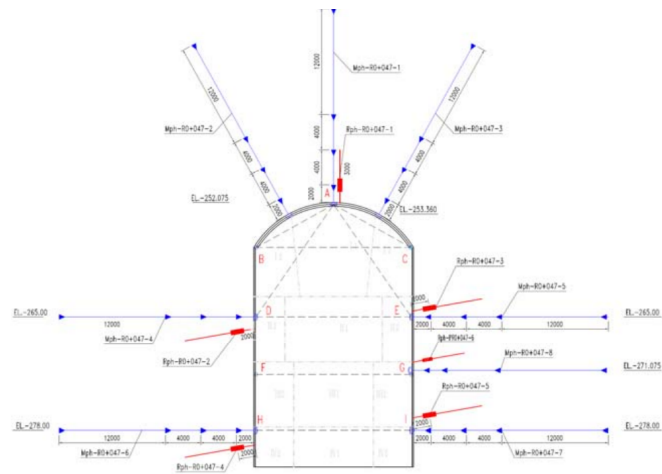


Figure 3.27: Extensometer section E.

## Chapter 4

# Back analysis technical route and parameters

### 4.1 Back analysis technical route

The back analysis is a crucial part design of an underground cavern complex during the construction stage, which is important to check the original support design capacity and verify if the rock mass parameters and boundary conditions are suitable . During the execution phases, in-situ stress should be checked concerning the updated geology mapping and the monitoring data, due to uncertainties in the representation of the mechanical behavior of the rock mass .

The UCS of intact rock has been validated by further laboratory tests by comparing the results with the ones of the design stage. The target is to match a reasonable GSI value with the post-peak behavior of rock mass which is matching with the monitoring results.

It should be clarified that according to the complexity of the geological conditions, heterogeneity, and anisotropy of the rock mass, it is impossible to reflect all these characteristics in the numerical model. Thus, the back analysis is not precisely matched to the monitor data for each device.

The technical route for back analysis is shown in figure4.1

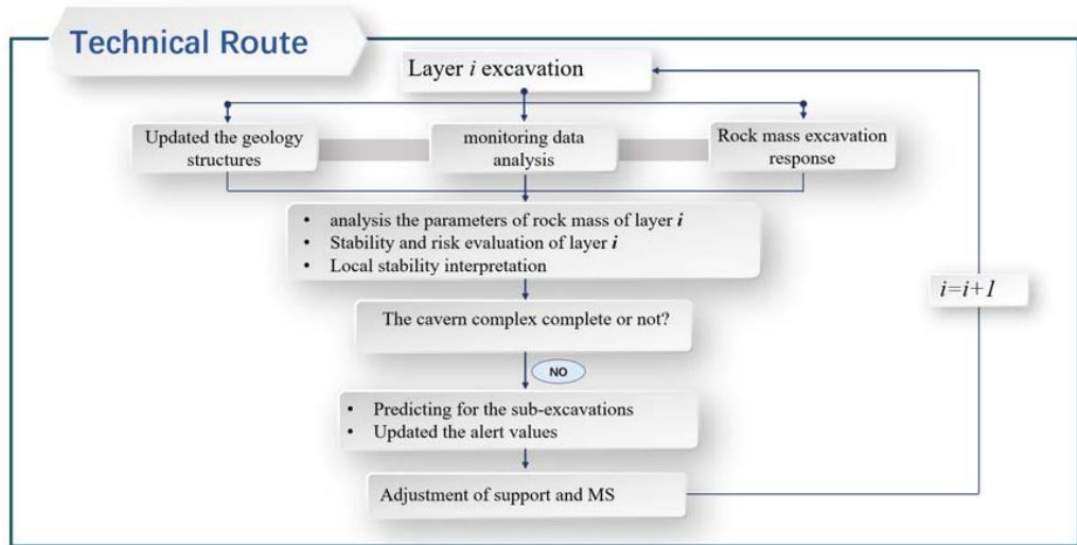


Figure 4.1: Technical route of back analysis.

## 4.2 Rock mass constitutive mechanical model

Recently it has been becoming reasonable to take the advantage of the power of the computer to demonstrate and scrutinize the rock behavior including instability which occurs as a result of one or more mechanisms of failure. On the other hand, the appropriate analysis tools and the optimization of the support system rely on understanding the instability mode. The main instability modes are illustrated below:

- Brittle-rock failure involves two possible rock mass behavior modes depending on the jointing density. Massive-brittle behavior is evident in massive rock masses ( $GSI > 75$ ) and is probably the most challenging behavior to simulate with existing numerical methods. Brittle behavior jointed rock masses ( $30 < GSI < 75$ ) involves the sliding, rotation, and crushing of rock blocks. This behavior mode is typical of blocky rock masses and is common in many mining environments. The predominant post-failure behavior (strain-softening model) is the jointed brittle type illustrated in the middle sketch in Figure 4.2.
- Weak-rock shear failure occurs in a heavily jointed, weak rock mass (Geological Strength Index ( $GSI < 30$ ) or weak intact rock dominated by stress-driven shear yielding behavior. Continuum-based plasticity models (perfect elastic-plastic model) are well suited to this instability mode, which is illustrated in the bottom sketch in Figure 4.2.
- Structurally controlled failure is dominated by geological structures such as

gravity-controlled wedge instability. The limit equilibrium method and the distinct element method are fit to this instability mode.

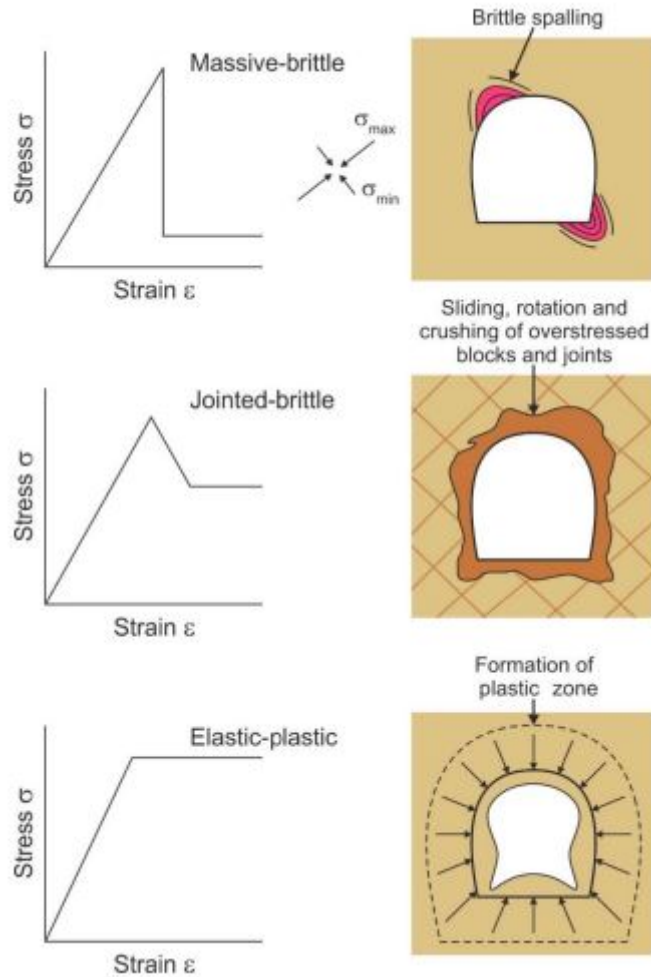


**Figure 4.2:** Simplified post-failure and tunnel behaviour.(Loren,2013)

Concerning the latest geological model and rock mass conditions, the strain-softening models might be more reasonable for bs-strong class III and bs-weak class III. While the pyroclastic class IV and bs-weak class v, could be more convenient for the perfect elastic-plastic models.

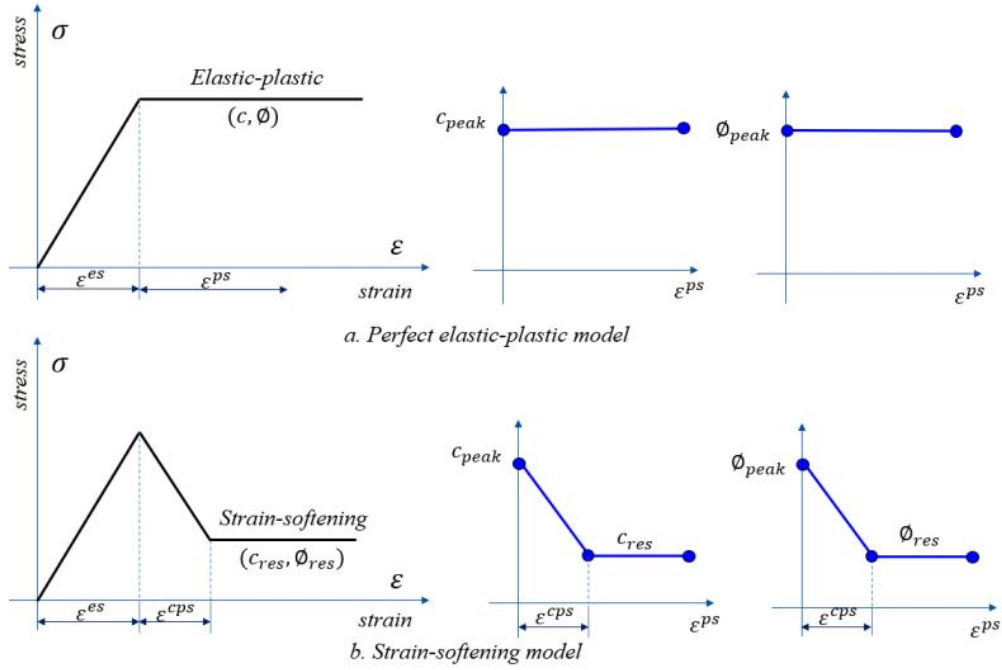


**Figure 4.3:** Cohesion and friction angle for different constitutive model.

The path to providing representative rock mass properties must be implemented through a derived sequence from GSI classification and Hoek-Brown strength criterion. In addition, several assessments should be involved which start from the intact rock laboratory properties, strength, stiffness, and rock mass characteristics. The generalized Hoek Brown criterion for jointed rock mass is expressed as:[3][4]

$$\sigma'_1 = \sigma'_3 + \sigma_{ci} \left( m_b \frac{\sigma'_3}{\sigma_{ci}} + s \right)^a \quad (4.1)$$

$$m_b = m_i \exp \left[ \frac{GSI - 100}{28 - 14D} \right] \quad (4.2)$$

Where  $\sigma'_3$  and  $\sigma'_1$  are the minor and major principal stresses,  $m_b$  is a reduced value of the material constant  $m_i$ .  $s$  and  $a$  are constants for the rock mass given by the following relations:

$$s = \exp \frac{GSI - 100}{9 - 3D} \quad (4.3)$$

$$a = \frac{1}{2} + \frac{1}{6} \left[ \exp \frac{-GSI}{15} - \exp \frac{-20}{3} \right] \quad (4.4)$$

The uniaxial compressive strength is obtained by setting  $\sigma'_3=0$  in equation 4.1:

$$\sigma_c = \sigma_{ci} * s^a \quad (4.5)$$

Thus,the tensile strength is:

$$\sigma_t = -\frac{s * \sigma_{ci}}{m_b} \quad (4.6)$$

The deformation modulus is derived from:

$$E_m(GPA) = \left(1 - \frac{D}{2}\right) \sqrt{\frac{\sigma_{ci}}{100}} \cdot 10^{\frac{GSI-10}{40}} \quad (4.7)$$

The equivalent angles of friction and cohesive strength are given by:

$$\phi' = \sin^{-1} \frac{6am_b(s + m_b\sigma'_{3n})^{a-1}}{2(1+a)(2+a) + 6am_b(s + m_b\sigma'_{3n})^{a-1}} \quad (4.8)$$

$$c' = \frac{\sigma_{ci}[(1+2a)s + (1-a)m_b\sigma'_{3n}](s + m_b\sigma'_{3n})^{a-1}}{(1+a)(2+a)\sqrt{1 + (6am_b9s + m - b\sigma'_{3n})6a - 1}/((1+a)(2+a))} \quad (4.9)$$

Where  $\sigma'_{3n}=\sigma'_{3max}/\sigma_{ci}$ .

The concept of a global rock mass strength could be estimated from the Mohr-Coulomb relationship:

$$\sigma'_{cm} = \frac{2c' \cos \phi'}{1 - \sin \phi'} \quad (4.10)$$

where  $c'$  and  $\phi'$  calculated within the stress range  $\sigma_t < \sigma'_3 < \sigma_{ci}/4$  giving:

$$\sigma'_{cm} = \sigma_{ci} \cdot \frac{(m_b + 4s - a(m - b - 8s))/(m_b/4 + s)^{a-1}}{2(1+a)(2+a)} \quad (4.11)$$

The studies results for the deep tunnels are shown in figure?? and the fitted equation is:

$$\frac{\sigma'_{3max}}{\sigma'_{cm}} = 0.47 \left( \frac{\sigma'_{cm}}{\gamma H} \right)^{-.94} \quad (4.12)$$

Where  $\gamma$  is the unit weight of the rock ,  $\sigma'_{cm}$  is the rock mass strength, H is the depth of the tunnel below the surface.

If the horizontal stress is higher than the vertical stress, the horizontal stress value should be used in place of  $\gamma H$ .

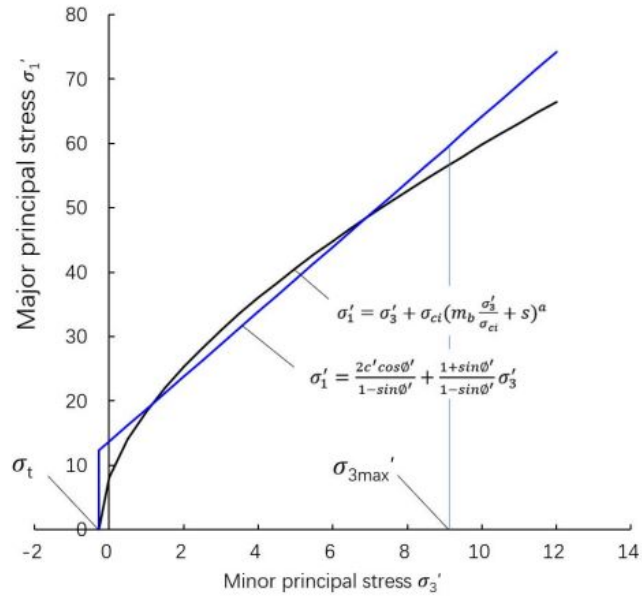


**Figure 4.4:** Major and minor principal stress for Hoek-Brown and equivalent Mohr-coulombe criteria

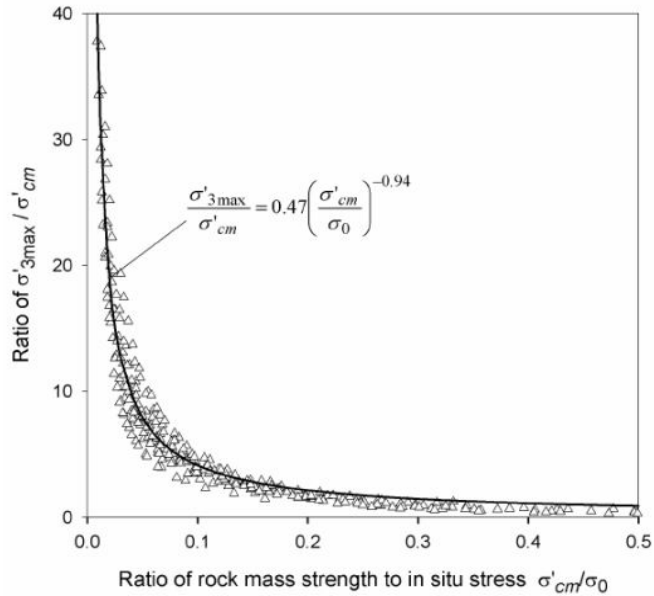


**Figure 4.5:** Calculation of  $\sigma'_{3max}$  for equivalent Mohr-Coulombe and Hoek-Brown parameters for tunnels

The Mohr-Coulombe parameters could be derived from the Hoek-Brown criterion(2002),according to the formula in figure4.6.

$$\sigma_3 = \frac{2c' \cos \phi'}{1 - \sin \phi'} + \frac{1 + \sin \phi'}{1 - \sin \phi'} * \sigma_1 \quad (4.13)$$

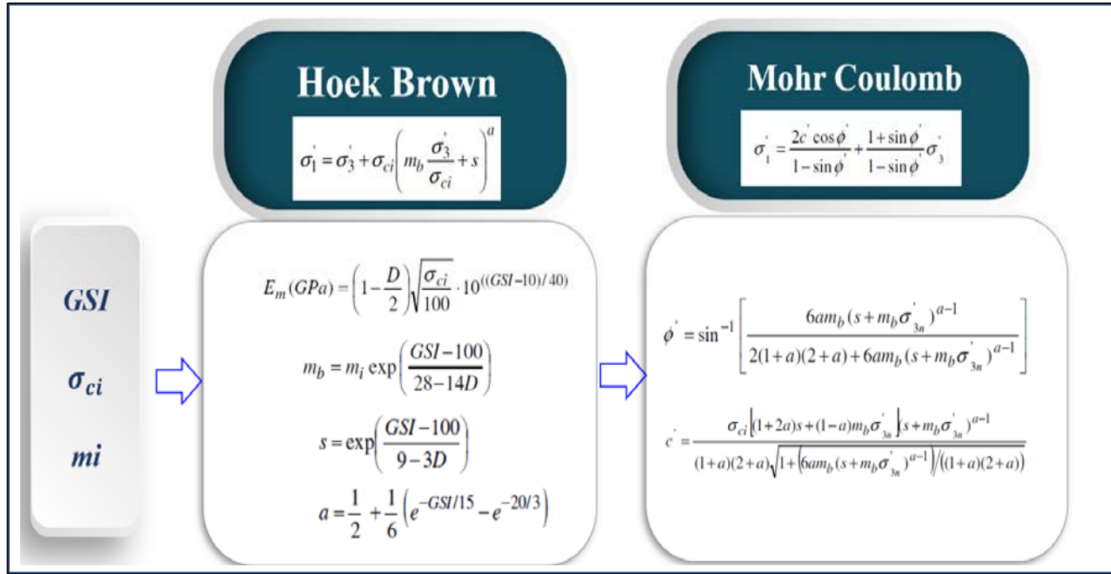


Figure 4.6: The parameters of rock mass when using the MC model

With respect to the strain-softening model, the residual strength should be back analyzed through the monitoring data. Furthermore, a fault characterized by a thickness greater than 2m should be simulated by solid zone by assigning the perfect elastic-plastic model, while for the thickness lower than 2m, the fault is modelled by interface with a linear strength criterion.

### 4.3 The parameters from back analysis

According to the back analysis results, the parameters are identified in table4.1 and table4.2.

**Table 4.1:** Updated parameters for bs-strong class III and bs-weak class III/IV

Lithology	UCS (MPa)	GSI	mi	D	Em (GPa)	Peak strength		Residual strength	
						Cohesion (MPa)	Fricton angle(deg)	Cohesion (MPa)	Fricton angle(deg)
bs-strong classIII	101.3	45	25	0	7.5	2.7	47.01	0	47.01
bs-weak classIII	50.81	43	25	0	4.76	2.05	41.08	0	41.08
bs-weak class IV	33.9	39	20	0	3.09	1.55	34.8	0	34.8

**Table 4.2:** Updated parameters for pyr IV and bs-weak V

Lithology	UCS (MPa)	GSI	m <sub>i</sub>	D	Em (GPa)	Peak Strength	
						Cohesion (MPa)	Fricton angle(deg)
Pyr	8.8	34	12	0	1.18	0.7	19.76
bs weak V	16.6	18	20	0	0.645	0.765	23.49

## Chapter 5

# Back analysis with 3D models

### 5.1 3D geological model and excavated structure

#### 5.1.1 3D geological model

As it has been shown before in the second chapter, the geological stratigraphy is complex. Moreover, it consists of many layers of different classes of rocks and faults. Thus, to design the geological condition directly in RS3 code is impossible. So, it is decided to draw it first in Rhino 3D which is a powerful design software to overcome this issue as shown in the figures 5.1 to 5.4.

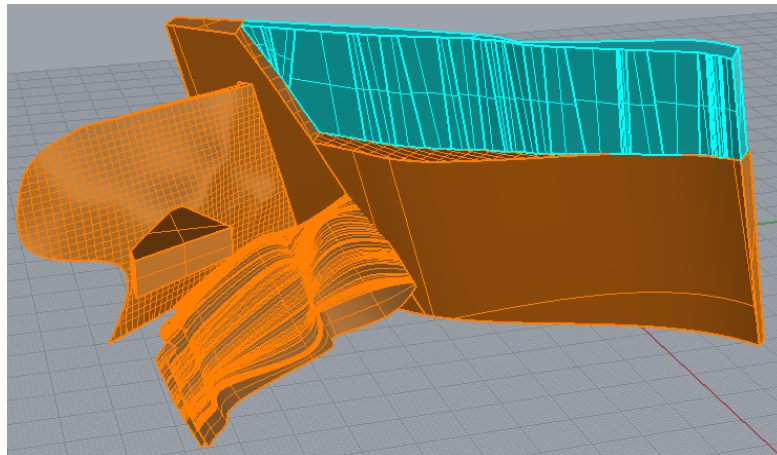


**Figure 5.1:** Class V and class IV

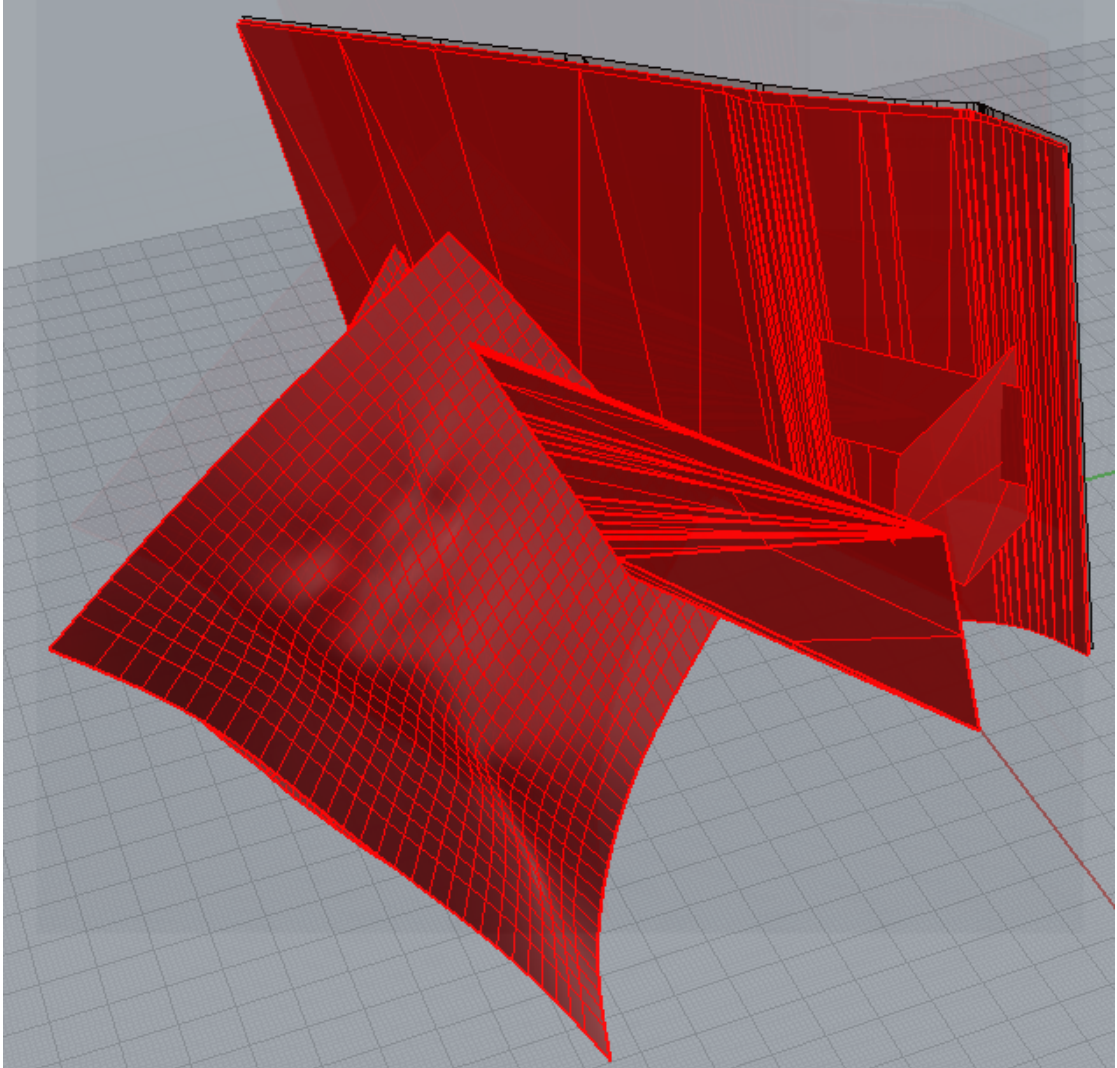


**Figure 5.2:** Faults

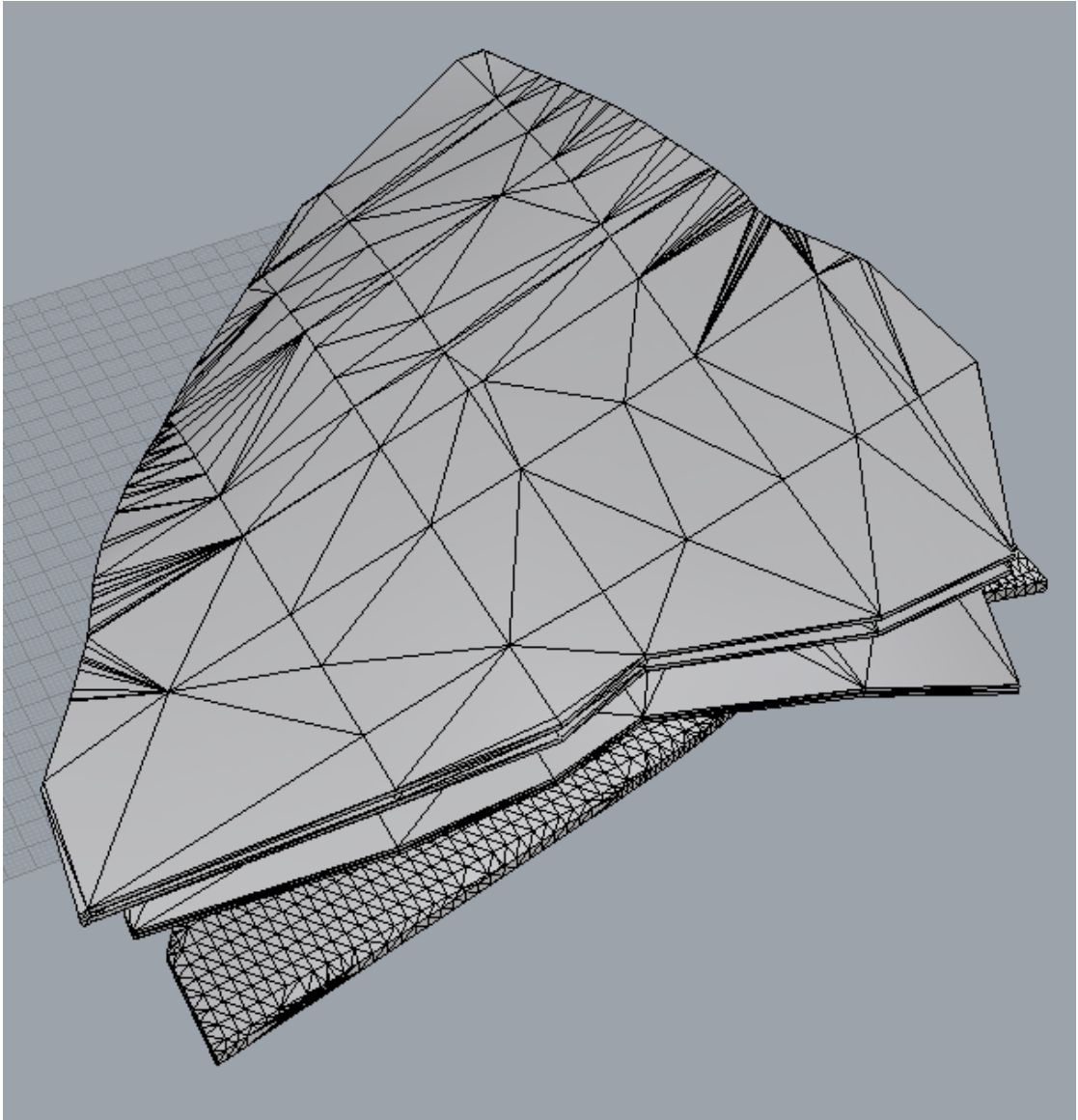


**Figure 5.3:** Pyroclastic layers

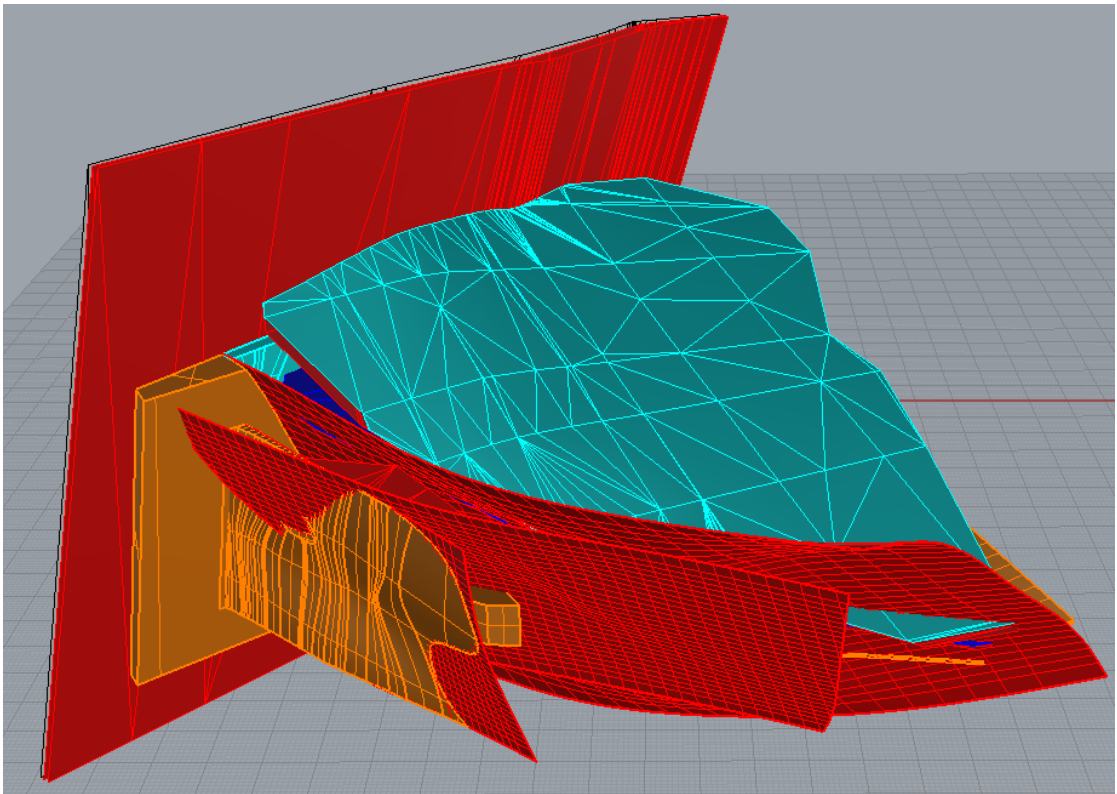


**Figure 5.4:** 3D geological model

The geological entities are nested and overlaid with each other. Furthermore, the curvature of the faults is going to cause issues to the RS3 code during the analysis. So, the solution is to simplify the geological entities and try step by step to increase the complexity to overcome the limits of the software. The first simplification is done on the pyroclastic layers where their curvature was reduced. Then the bs-class V geometry is to be reduced in size by cutting pieces until the optimum analysis is obtained. This is done because the bs-class v is tangent to the excavation contour. All simplifications are shown in figures 5.5 , 5.6 and 5.8.

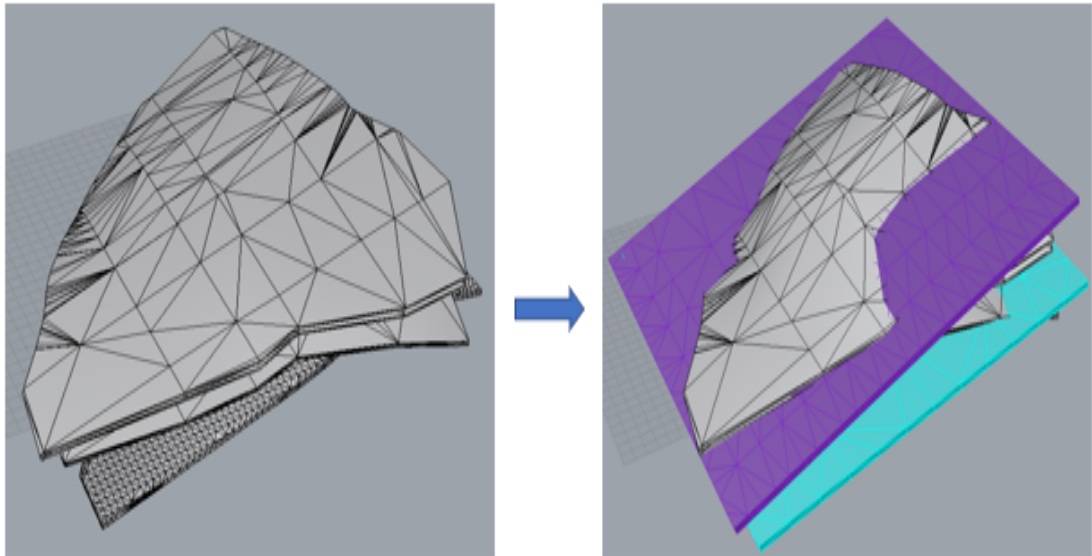


**Figure 5.5:** Modification of the pyroclastic layer

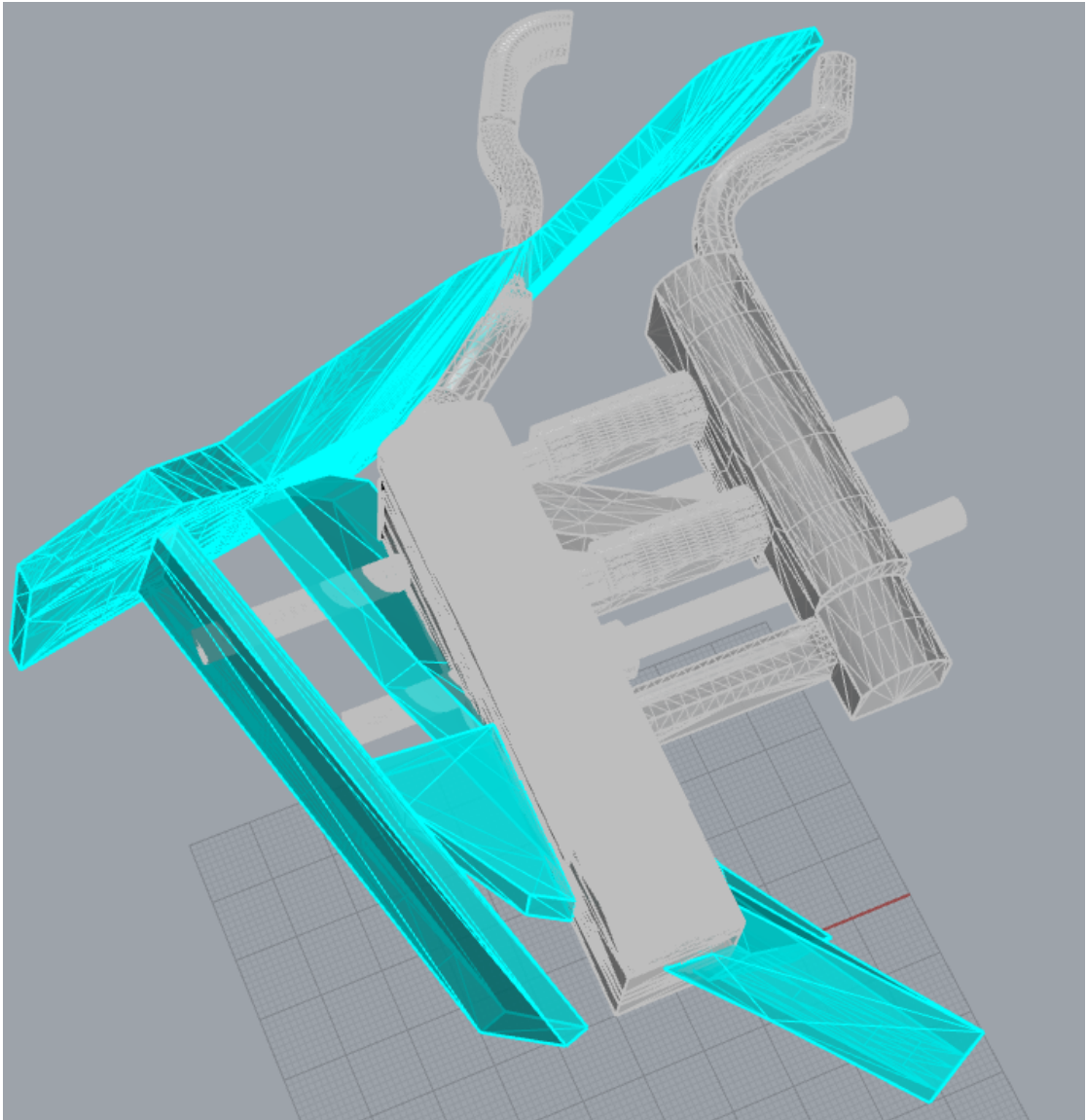


**Figure 5.6:** Intersestion between PH and BS-IV

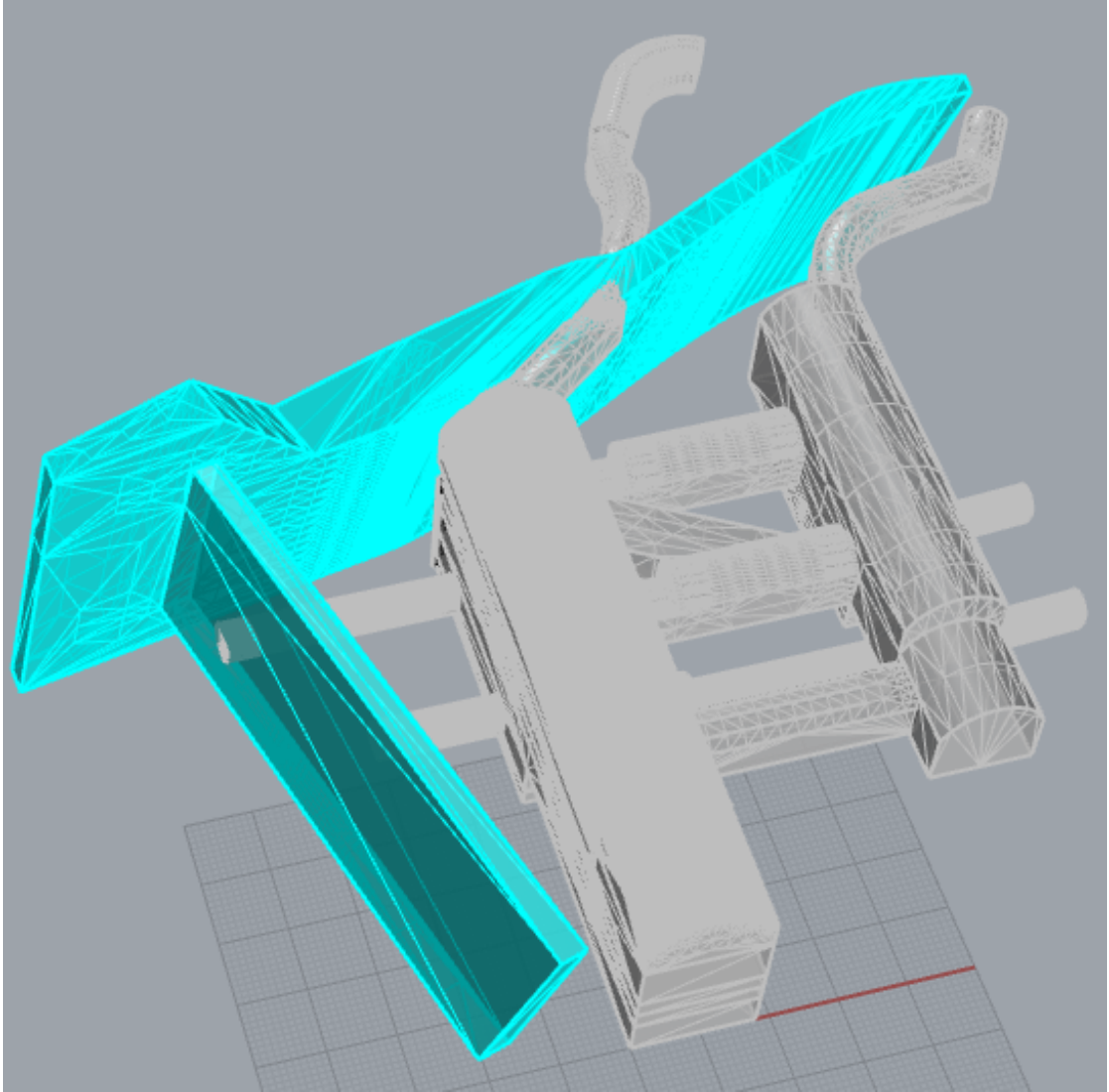


**Figure 5.7:** Modified class V to overcome mesh issues.

### 5.1.2 Modelling the excavated structures

The excavation structures consist of two main caverns and many intersections between crossed tunnels that are quite complex to draw directly in RS3 code. So, they have been designed in Rhino 3D too. Furthermore, the highlighted part with red circle in the north wall of the powerhouse in figure 5.9 and 5.11 has been modified because it created many problems for the mesh and the solver during analysis. The model of primary structure is reported in figure 5.8

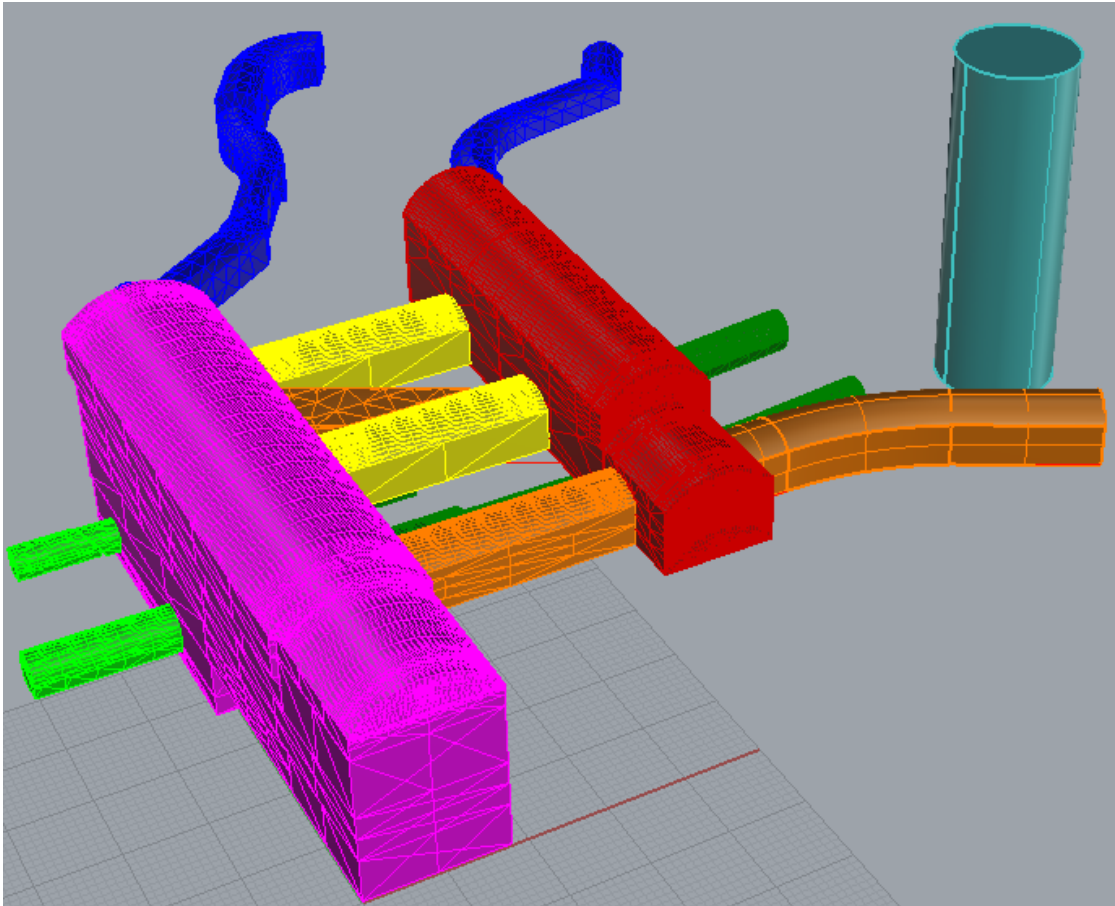


**Figure 5.8:** Primary structure.

Due to the complexity of the stratigraphy, a specific level of detail was defined as a target to have a balance between the reliability of the analysis results and the computational time and mesh quality . The selected geological entities are the most affecting the final results for instance faults No.22,31,18,16 and the pyroclastic layers No.(3,6,9). The scope of details has been shown in the figure5.12 and 5.13.

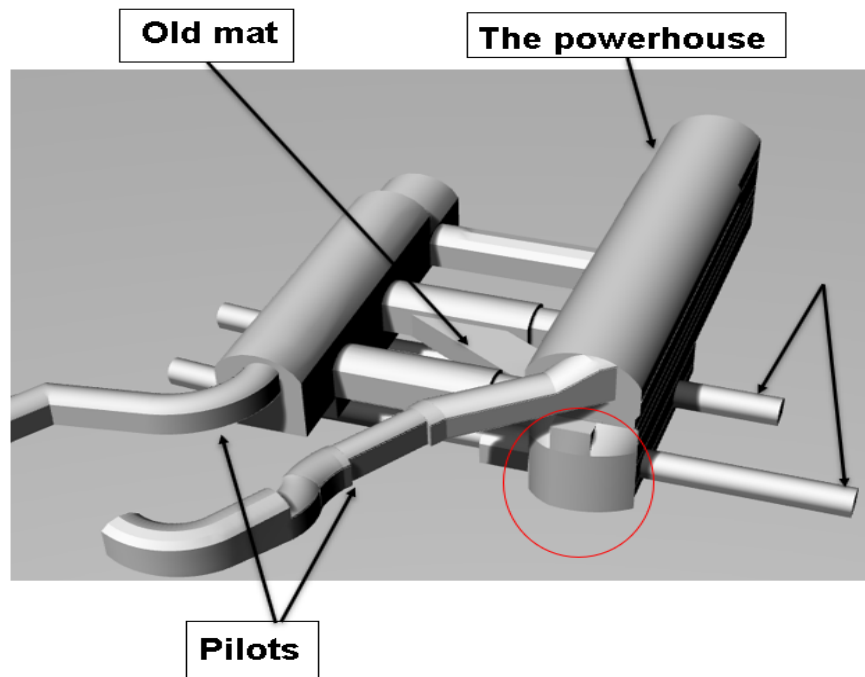


Figure 5.9: Excavation contour n.1.

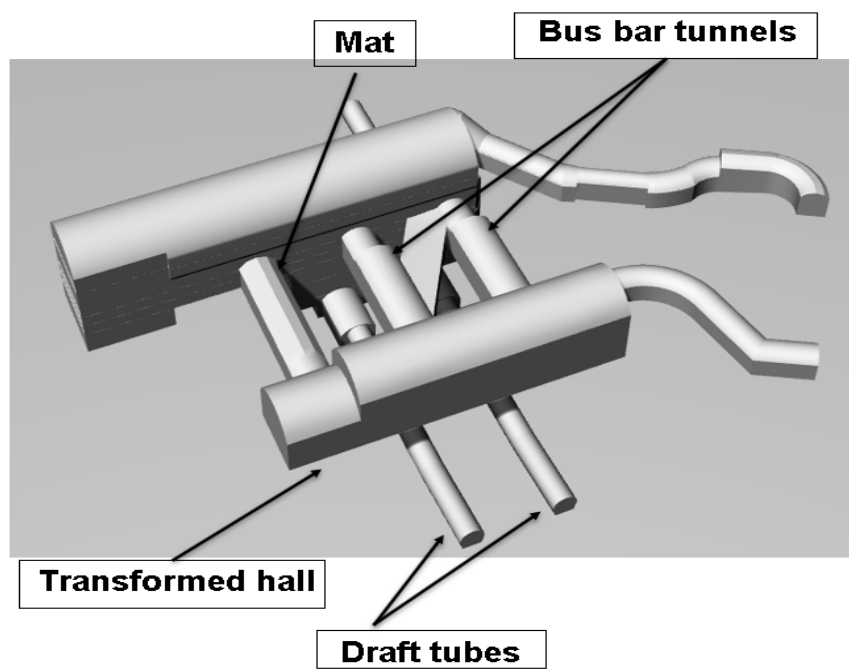
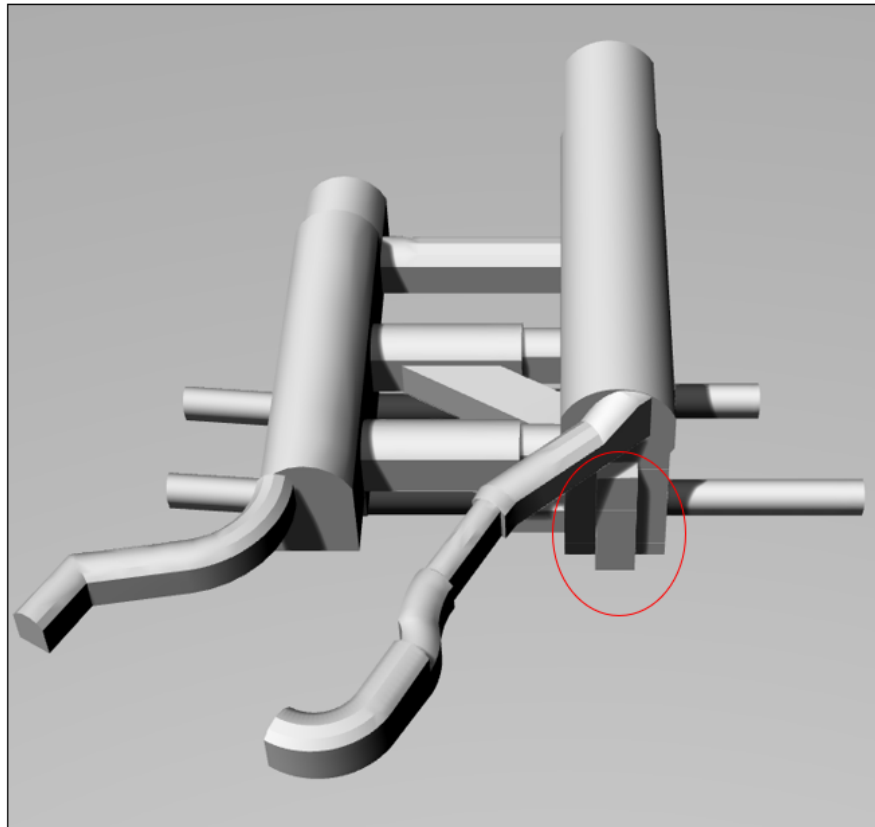
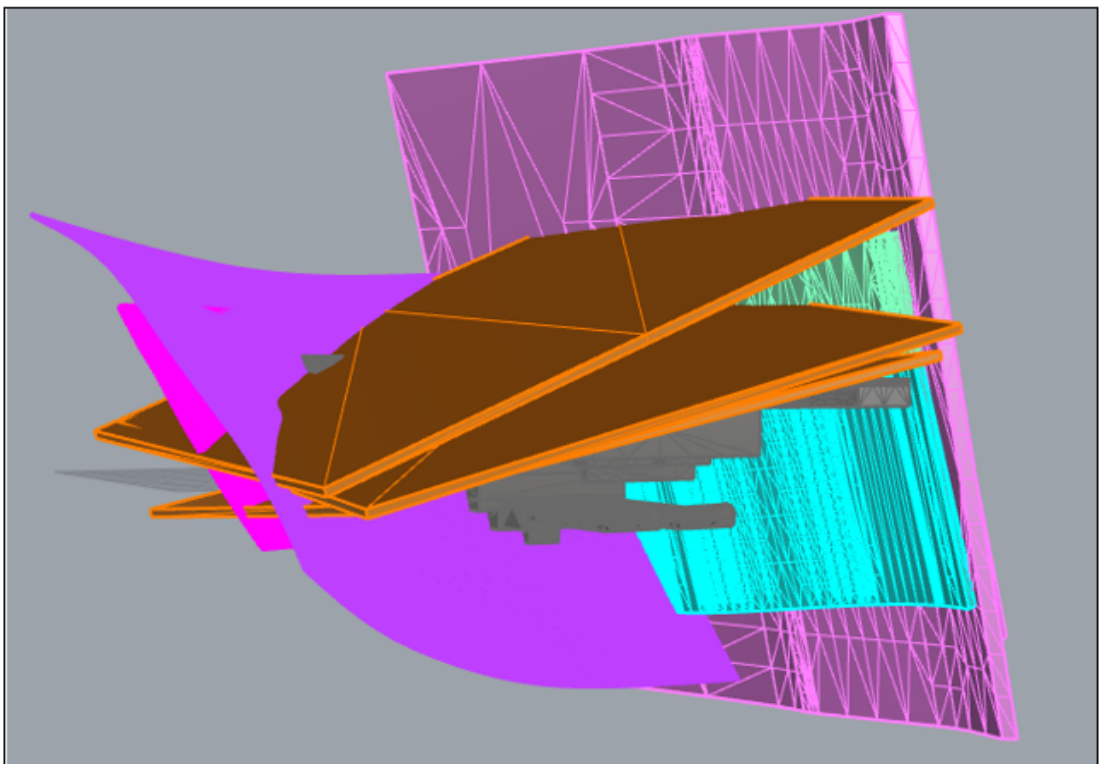


Figure 5.10: Excavation contour n.2.



**Figure 5.11:** Modified north wall.

Here in this figure ,the pyroclastic layers are clear and their intersection with the power house and the transformed hall.Also fault number 22 is intersected with front part of the power house and it's curvature is recognized .More over,fault 22 is affecting the whole up stream side wall.finally,the location of fault 16 is affected the north wall of the power house mainly .



**Figure 5.12:** Final level of details to simulate n.1.

The bs-weak class v here in this figure is located beside the up stream side wall and intersected with fault 31. Further more, both class V and fault 31 are playing a key role in the analysis. The bs-weak IV is going to reduce the stability of the pilot and the north wall.

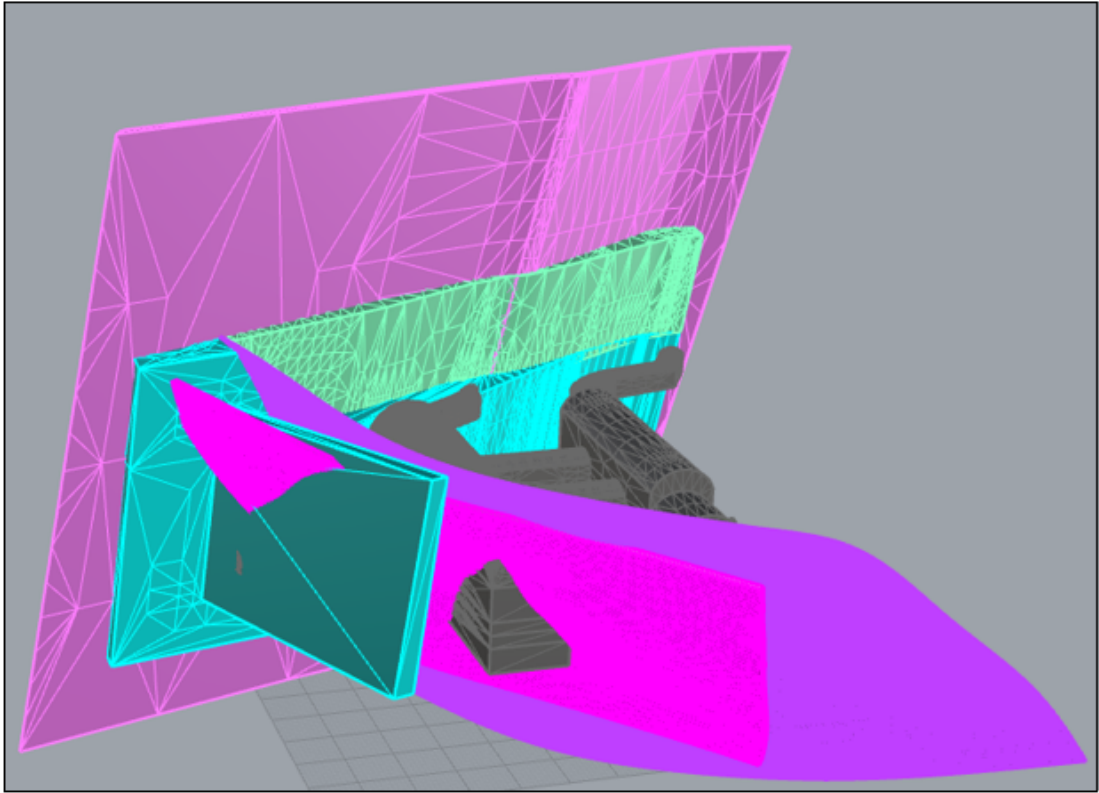


**Figure 5.13:** Final level of details to simulate n.2.

## 5.2 Numerical models and boundaries

### 5.2.1 Model geometry and excavation procedure.

The three-dimensional model includes the PH, the TH caverns, and the connecting Busbar tunnel 2 located in between them. The external box dimensions are 195x105x250m (BxHxL) as in figure 5.14. Concerning the excavation stages, the

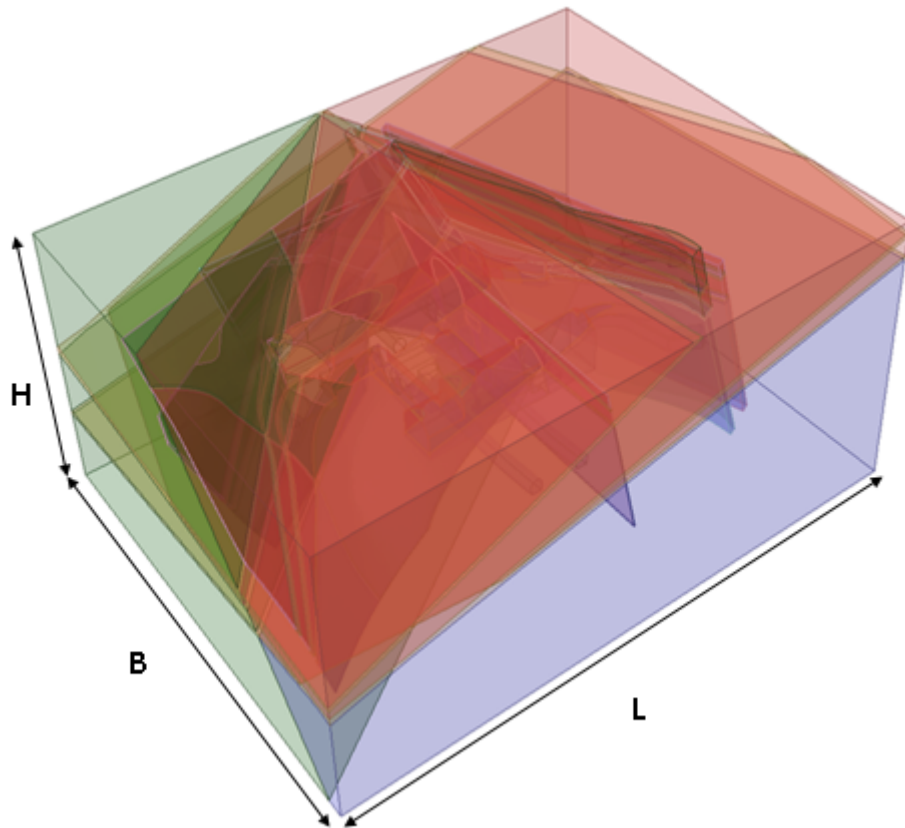


**Figure 5.14:** Model external dimension.

powerhouse was divided into six parts as it has been excavated. The first stage represents the original geological condition. Starting with the second stage, the pilot and the old mat were excavated. Moving to the third stage where the first part of the PH was excavated. Then in the fourth stage, the transformed hall was completely excavated with the second part of the PH. In the fifth and sixth stages, the third part of the powerhouse, mat, and the busbars were excavated respectively. Reaching the next two stages the fourth and fifth parts of the PH were excavated. Finally, in the last stage, the penstock and the draft tubes were excavated plus the

last part of the powerhouse.

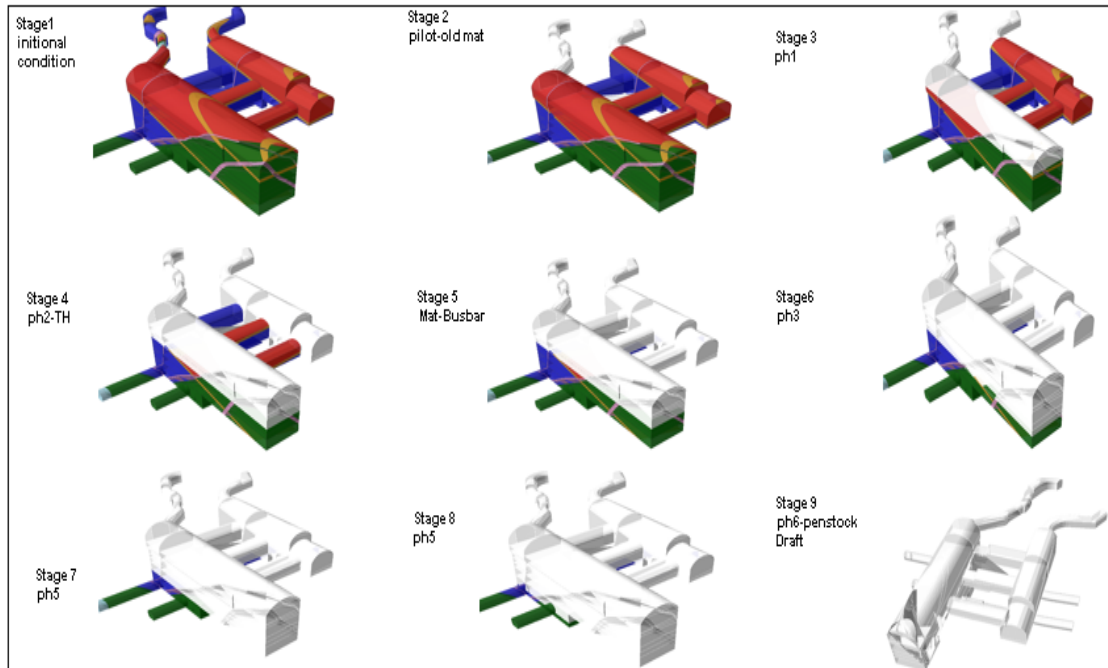


Figure 5.15: Excavation stages.

## 5.2.2 Different loads of simulation

To obtain optimum results from numerical software codes, there are three main components in the numerical models to be controlled. The first one is the level of details of the models to obtain logical results. Second is the mesh quality which can affect the computational time and the accuracy of the results. The third is the judgment on the results and comparing them with the monitoring data .

Three different models have been set up with three different levels of detail. They have been tested by comparing their output results and their computational time . The first level( 5.16) consists of fewer geological entities with respect to the second and third levels. The faults curvature is modified and replaced with straight plans. On the other hand, the second level(5.17) is more complex where the faults have been simulated as in reality. In the final model(5.18), all faults have been inserted and the bs-class IV entity was added as well.

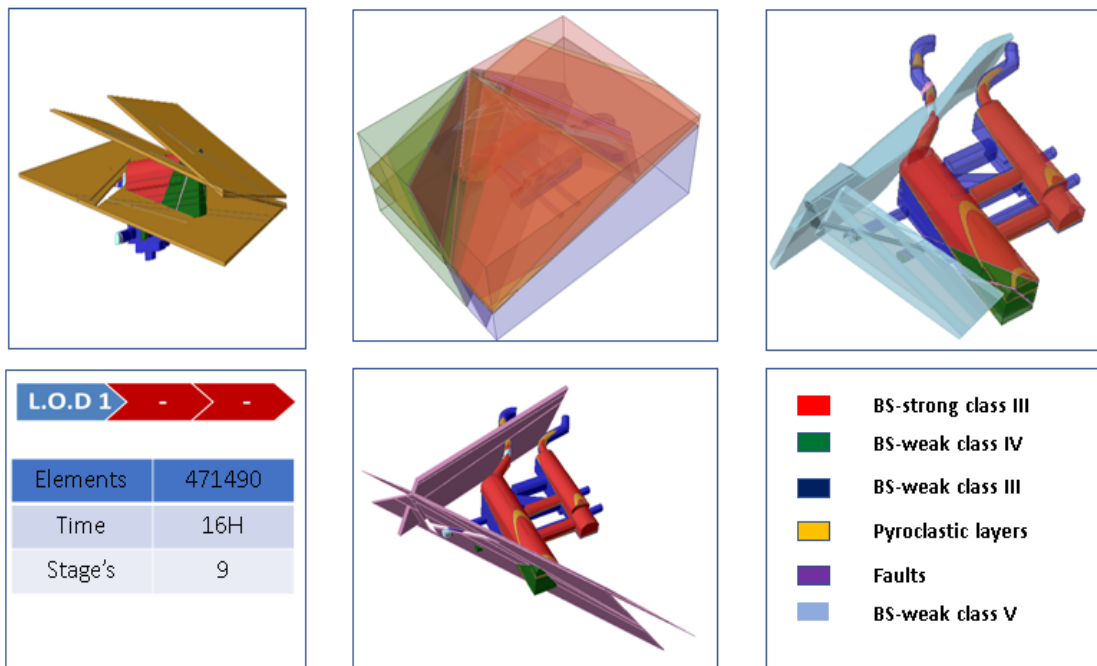


Figure 5.16: First model .

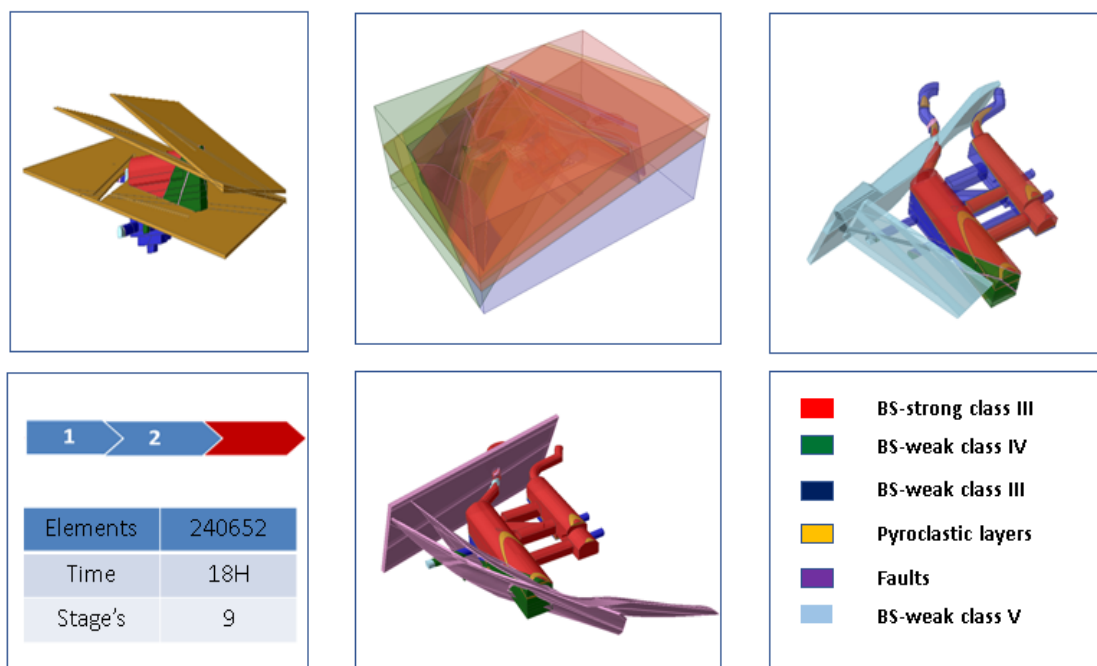
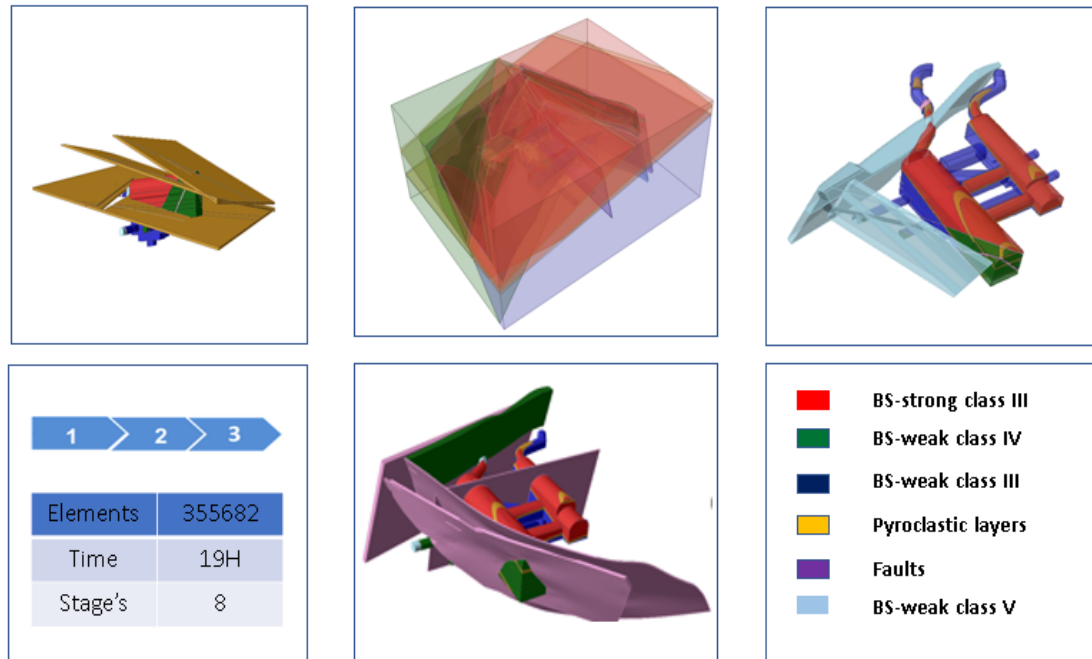


Figure 5.17: Second model .



**Figure 5.18:** Third model .

After managing to simulate different levels of detail, the scope has become to select the best model for performing the back analysis . Thus, a comparison has been done based on many factors: displacements ,maximum principle stress  $\sigma_1$ , minimum principle stress  $\sigma_3$ , and the yielding elements concerning the time which has been taken by the solver. In addition, it is clear that for the second and third models the results are much closer to each other than the first one, in terms of the displacements.

Also, the outputs for  $\sigma_1$  and  $\sigma_3$  are quite the same in all the three models. Finally, the yielded elements are almost uniform in the three models. In accordance with the comparison results, the second load was selected to be the main model and to have the supporting elements installed on it. The second model is more complete and reliable than the first one .Also the second model has less geological entities than the third one but have almost the same results.In general , the second model is less time consuming and computational effort.

Different results are shown in the next figures.

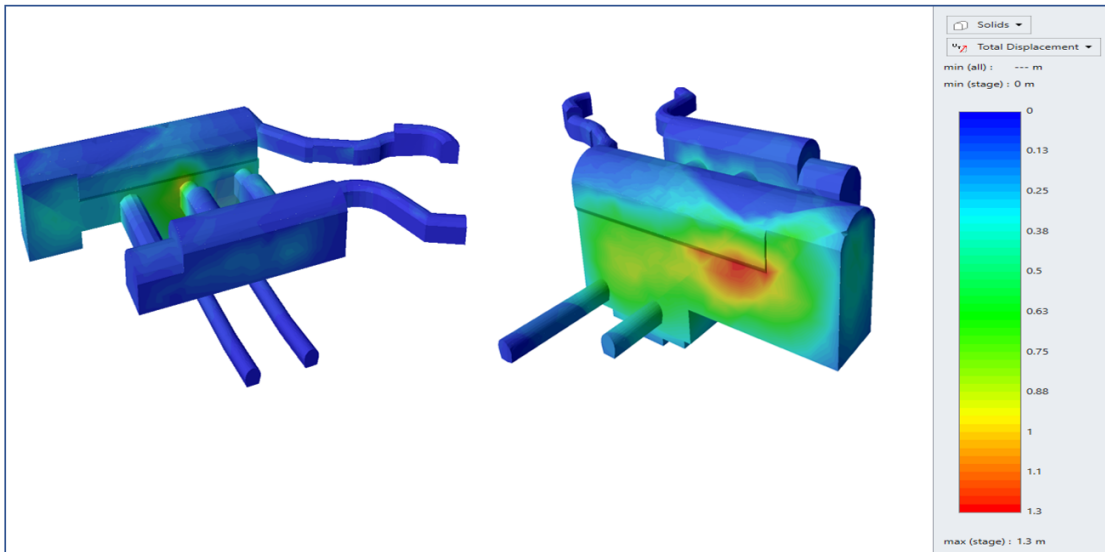


Figure 5.19: Displacements in the first model.

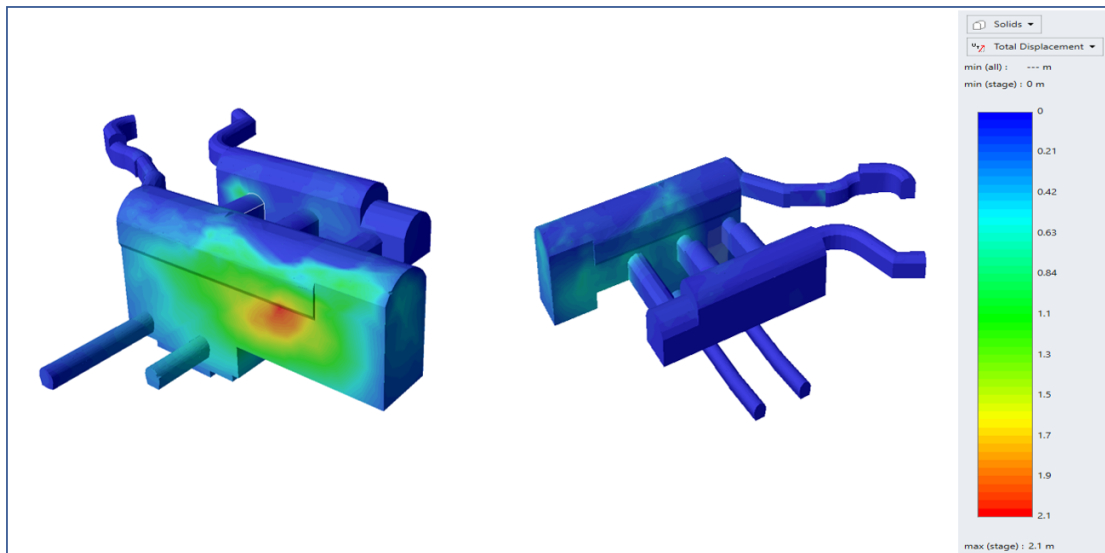


Figure 5.20: Displacements in the second model.

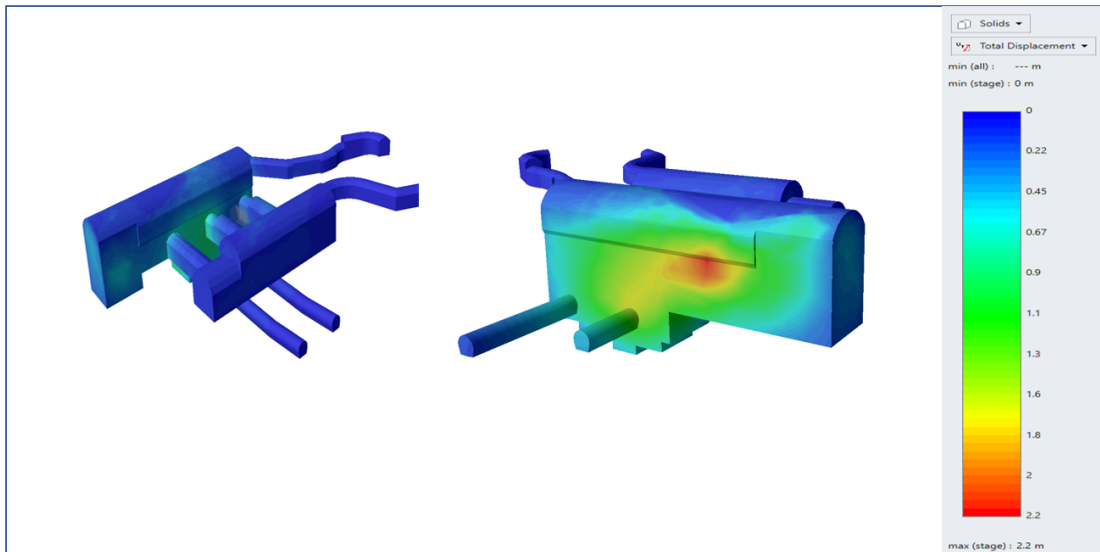


Figure 5.21: Displacements in the third model.

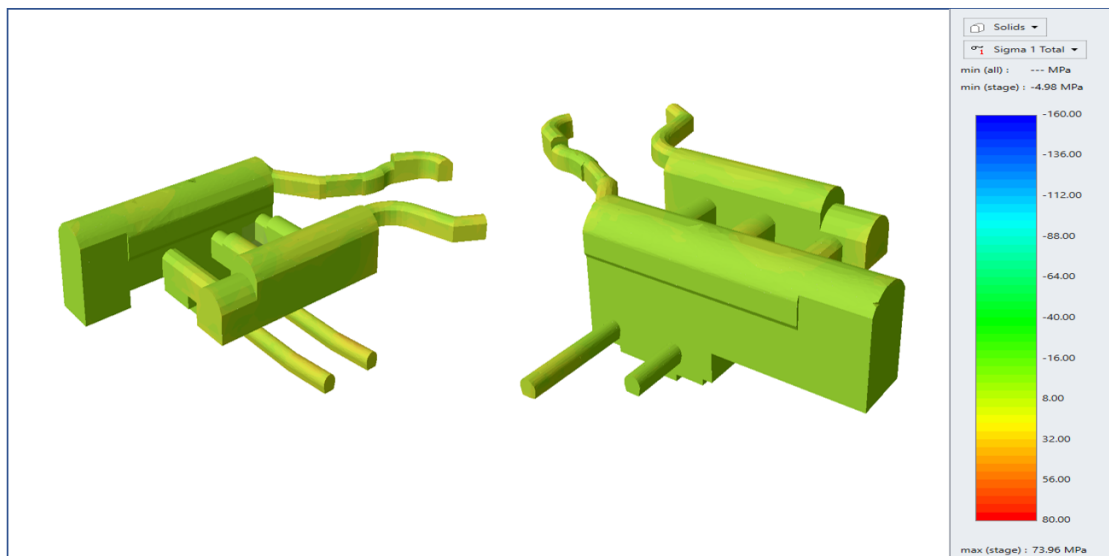


Figure 5.22: Sigma 1 in first model.

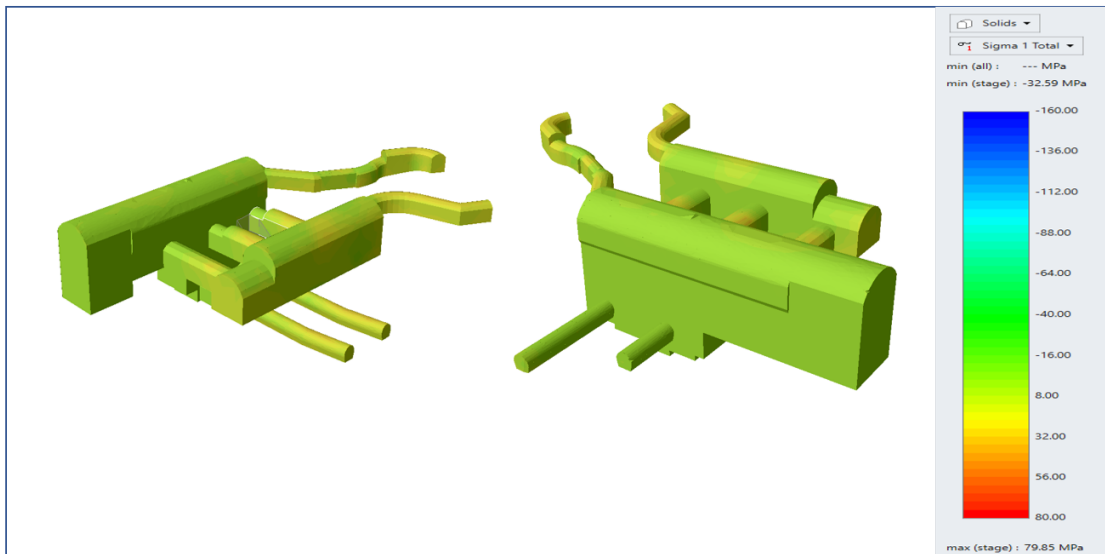


Figure 5.23: Sigma 1 in second model.

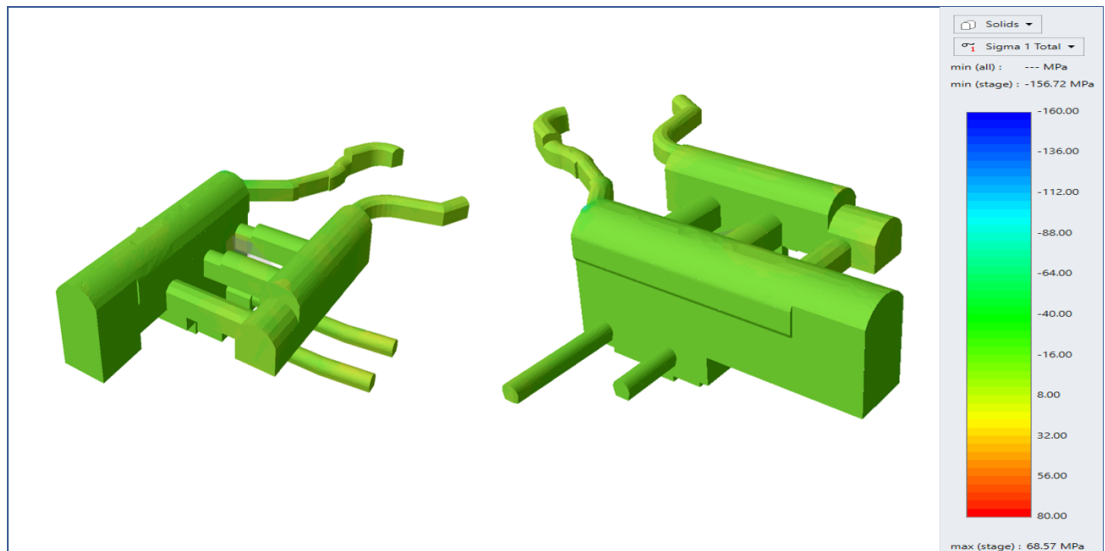


Figure 5.24: Sigma 1 in third model.

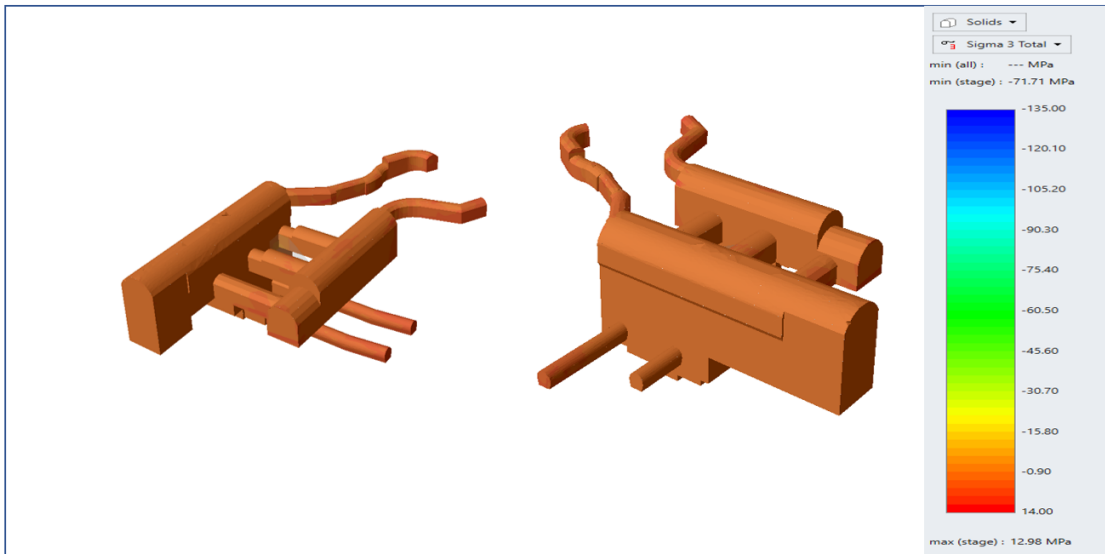


Figure 5.25: Sigma 3 in first model.

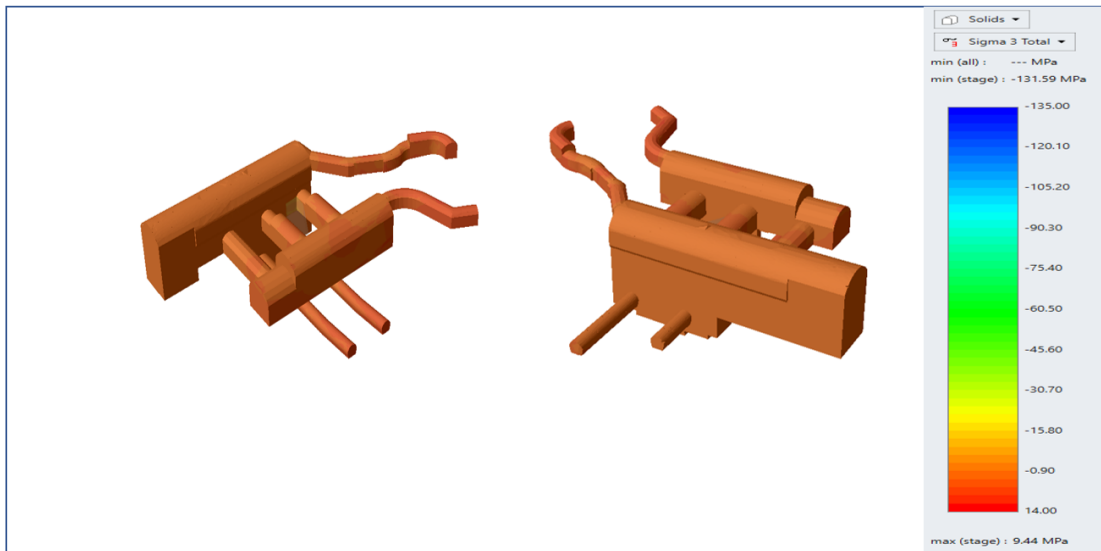


Figure 5.26: Sigma 3 in second model.

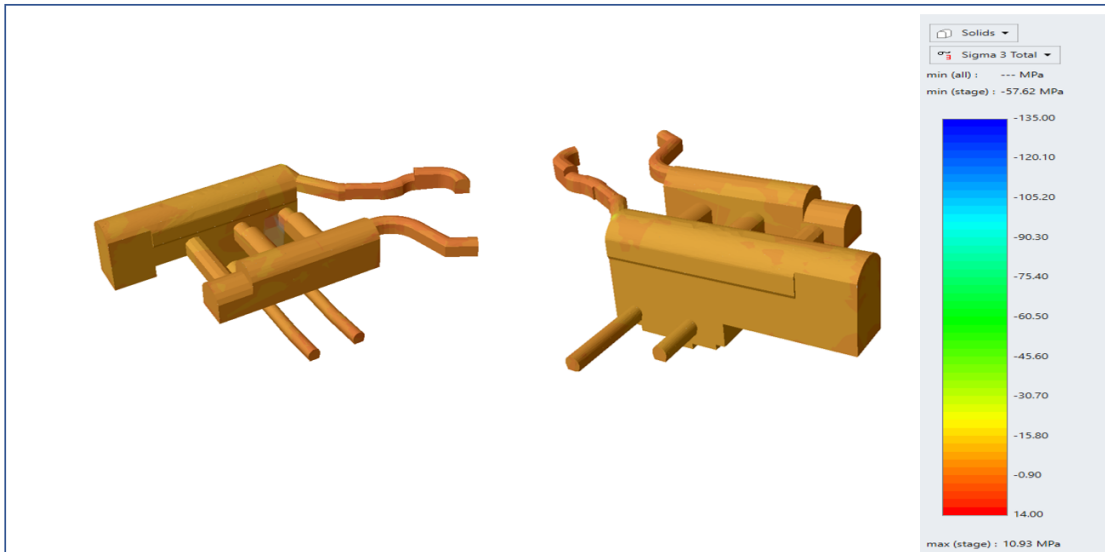


Figure 5.27: Sigma 3 in third model.

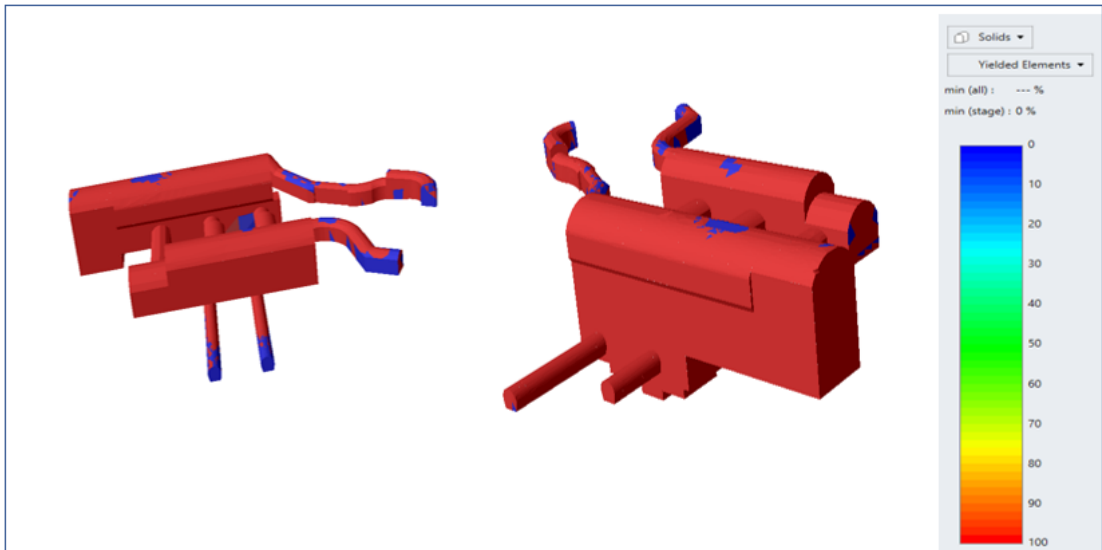
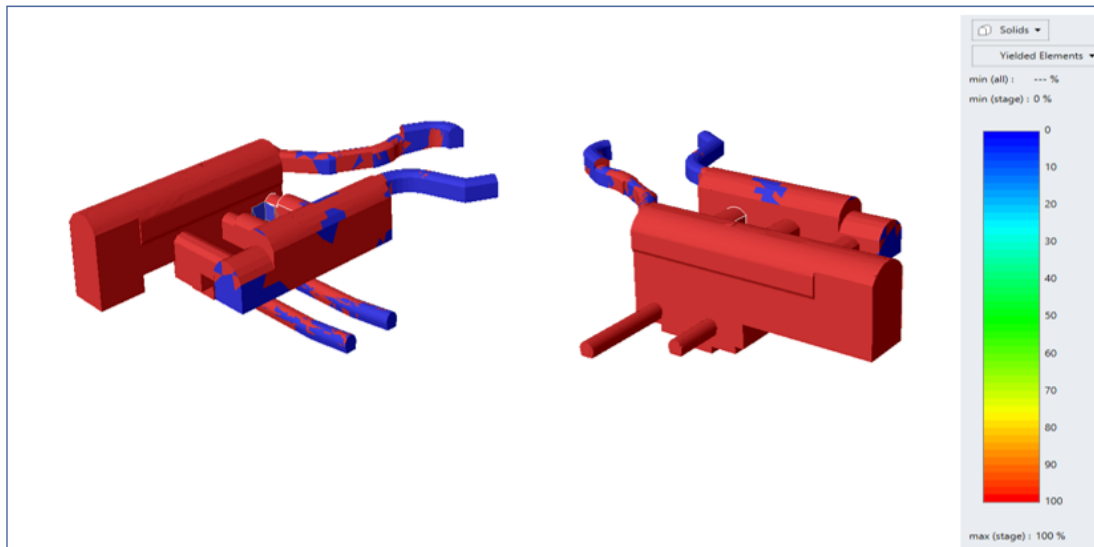
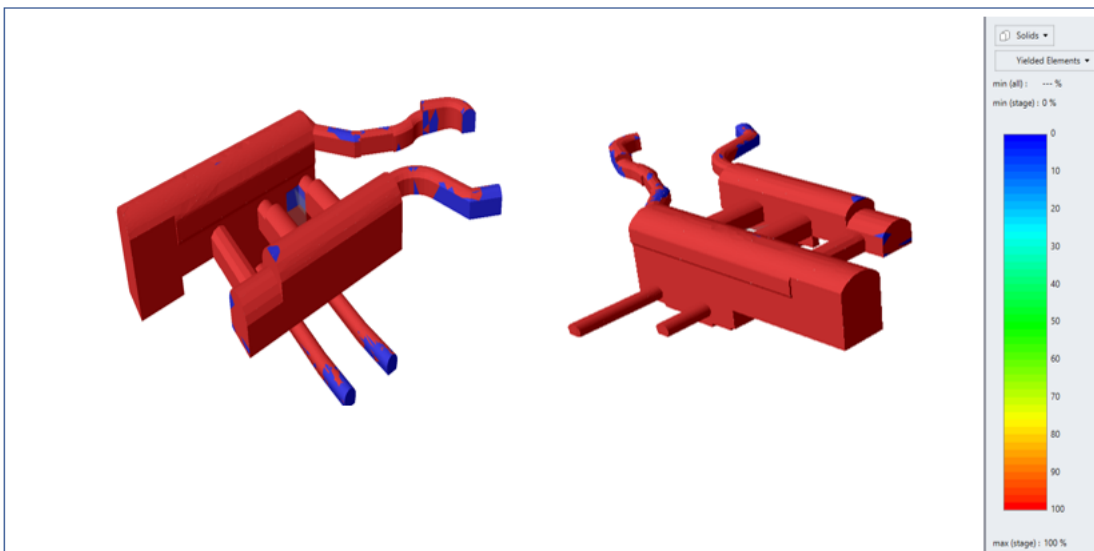


Figure 5.28: Yield elements in the first model.



**Figure 5.29:** Yield elements in the second model.



**Figure 5.30:** Yield elements in the third model.

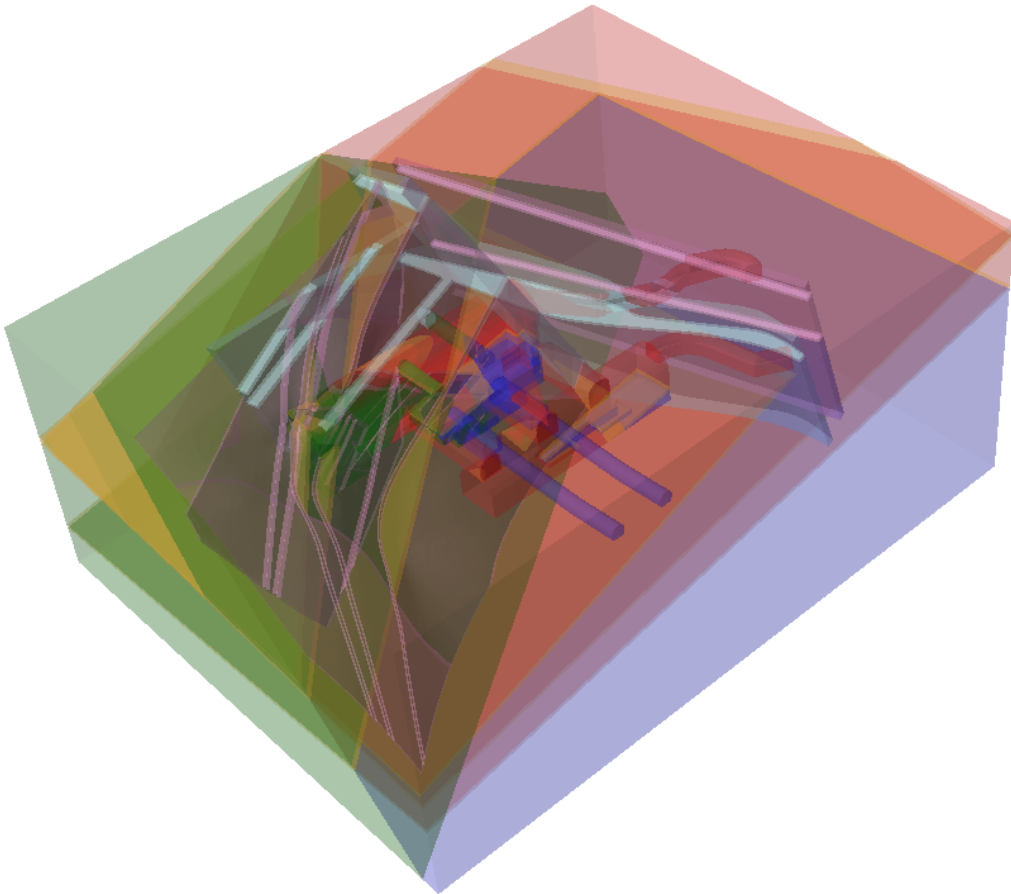


**Figure 5.31:** Final selected model.

### 5.3 Modeling the supports elements

The excavated structure supporting elements have been installed precisely stage by stage and are shown in the next figures. The supports consist of:

- Shotcrete of variable thickness ranged between 12cm to 25 cm (orange) that are installed all around the excavated structures and shotcrete of thickness 1.05 m (gray) which located on the upstream sidewall in the intersection between the faults 31,22 and the pyroclastic layer where high displacements are expected.
- pattern of rock dowel,  $\phi 25/\phi 28$ ,  $L = 7\text{m}$  (cyan). They are installed all around the power house and the transformed hall with a spacing of 1.5 m.
- 4 additional bar anchors from the first layer of the powerhouse floor towards fault 16.  $L = 44.9\text{ m}$ . (Brown)
- A group of Bar anchors, installed in the north wall towards fault 16 and class IV, V,  $L = 35.45\text{ m}$ . (light blue).
- A group of Bar anchors distributed over the powerhouse, upstream, downstream, north, and south wall, with a length of 26m (violet).
- There are bar anchors with the same color (light brown) but different lengths and pretension as for the ones in the upstream wall between penstocks and the ones in the north wall also in between busbar tunnels in the downstream wall each reach 11.8m, there is another group of those bar anchors with a length of 19.4m located in the upstream wall, layer 4 and 5, the last group of those bar anchors are in the downstream wall between busbar tunnels with a length of 10m.
- The black strand is located in the top part of the upstream wall with a length of 25m.
- The red strand of length 35m is located in the first layer of the powerhouse.

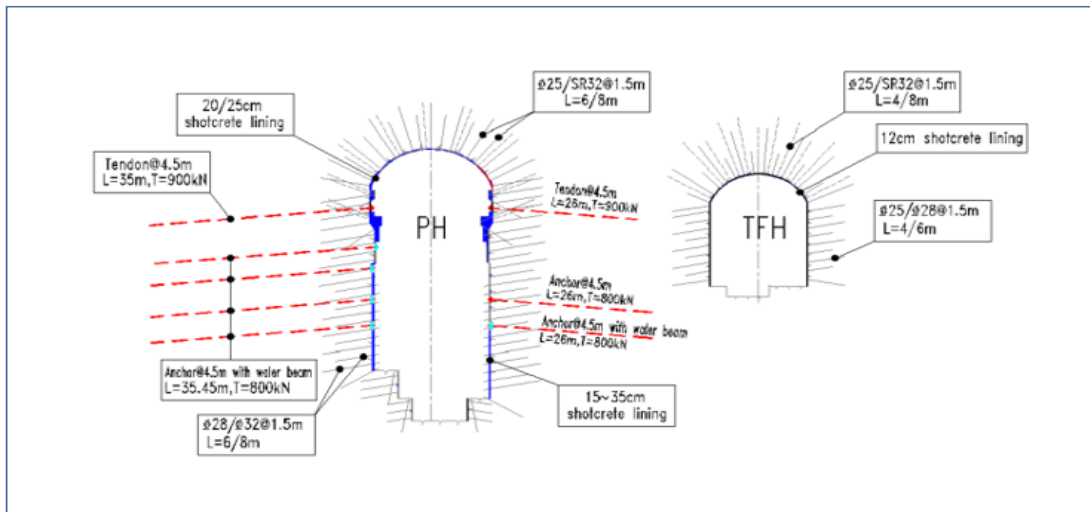


Figure 5.32: Supports on the powerhouse and transform hall.

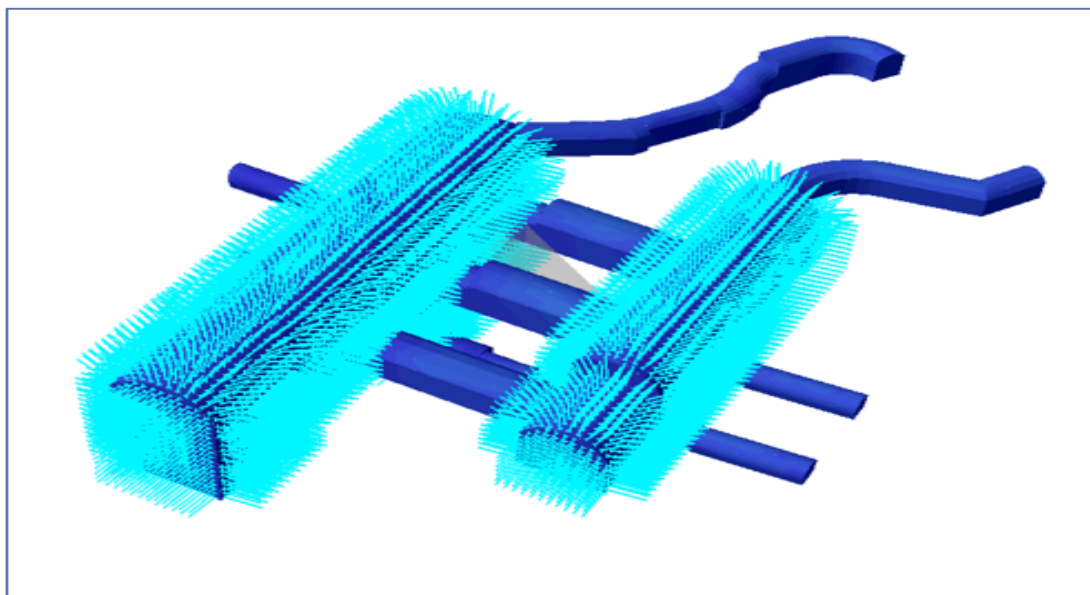


Figure 5.33: Rock bolts

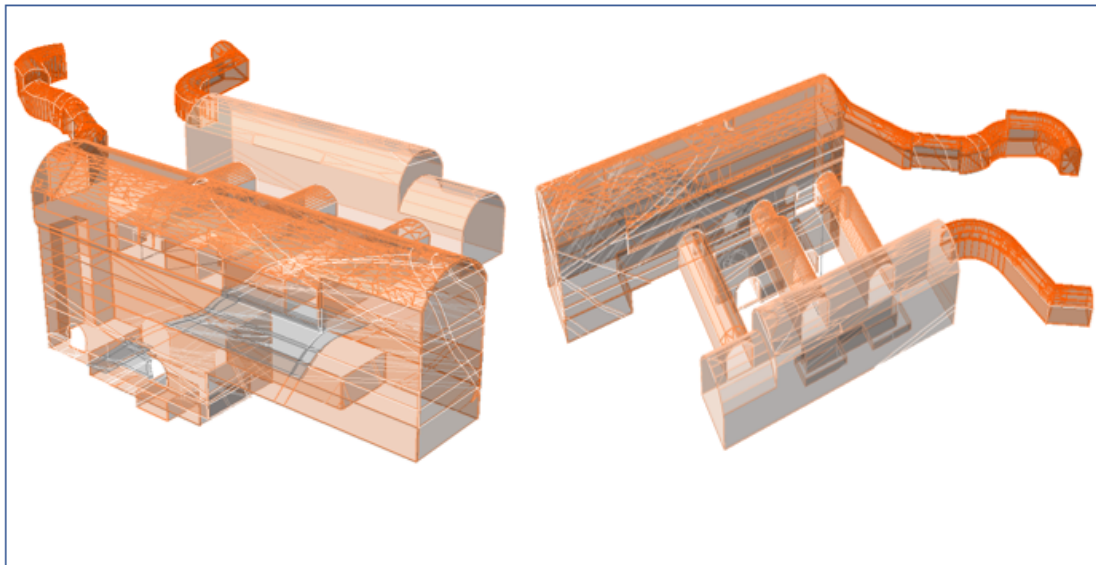


Figure 5.34: Various shotcrete sections

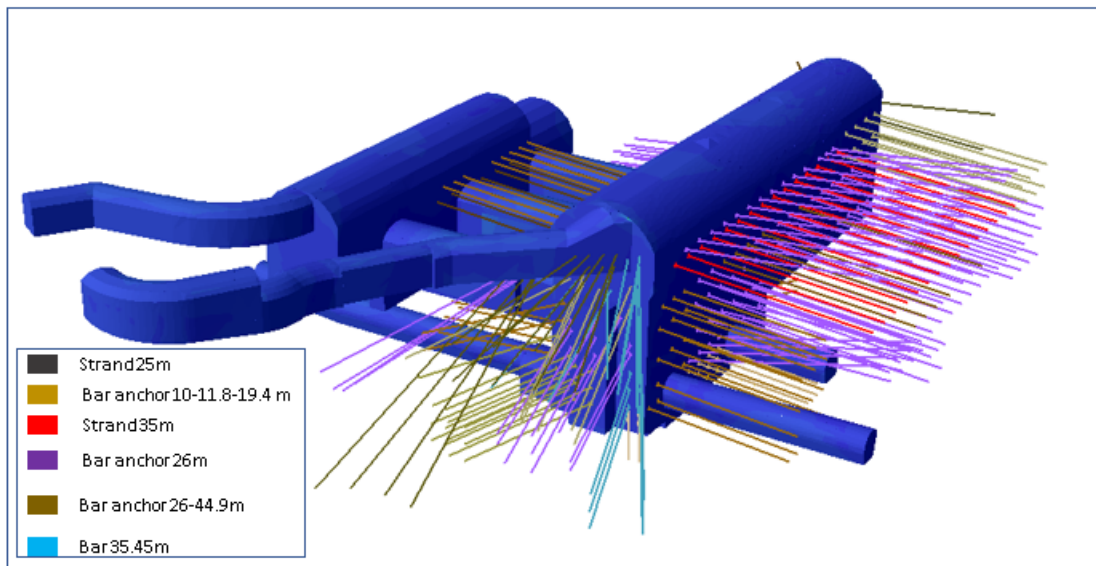
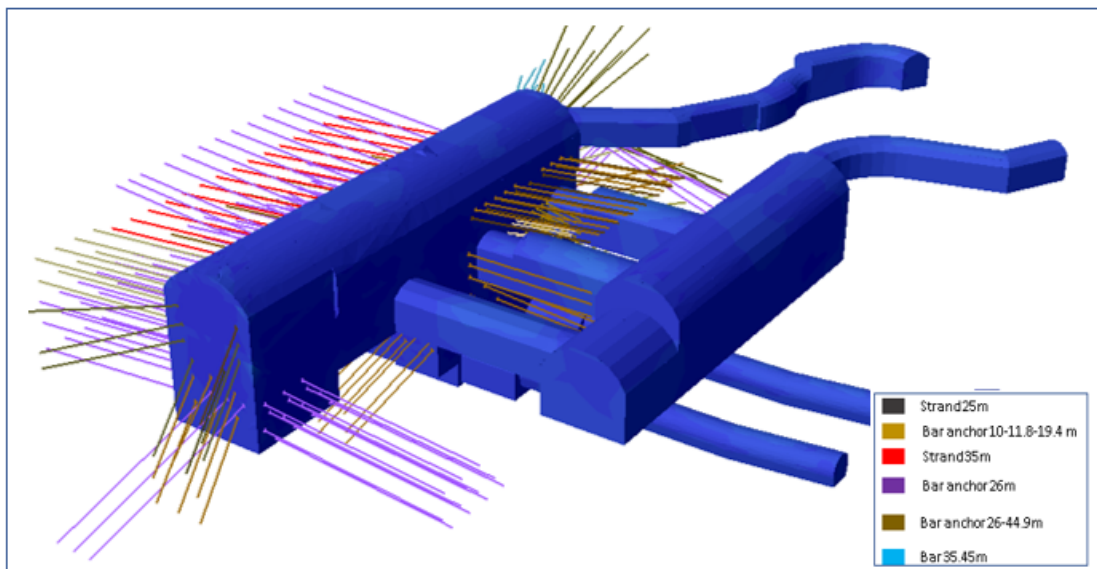


Figure 5.35: Upstream and north wall supports



**Figure 5.36:** South wall and down stream supports

## Chapter 6

# The Back analysis results

In this chapter, the results of the model described in chapter 5 have been compared with the results obtained by previous analyses carried out by the FDM implemented in code FLAC 3D. Furthermore, both models relied on the updated geological model and the same input data. The comparison of the two models is related to major aspects: total displacement, axial force in tendons, bar anchors, stress in rock dowels, and plastic zones.

### 6.1 Total displacements

The total displacements in the RS3 model is conformable with the results in FLAC 3D code. Furthermore, the maximum total displacement in both models is localized in the intersection of the upstream sidewall and fault 22, the pyroclastic layer 9, and the Class V rock mass.

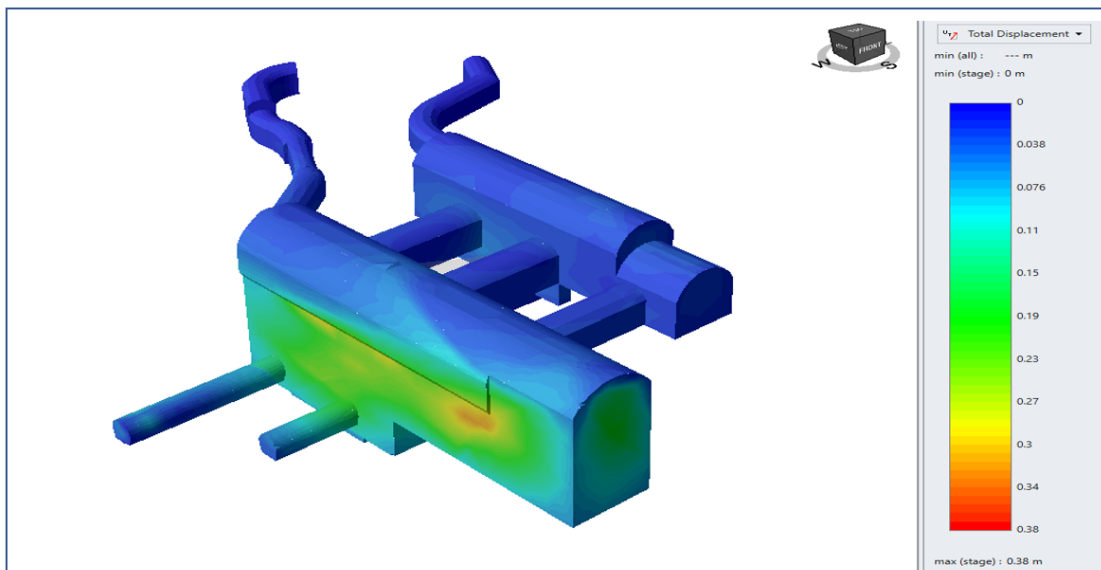


Figure 6.1: Displacements in the south and up stream wall.

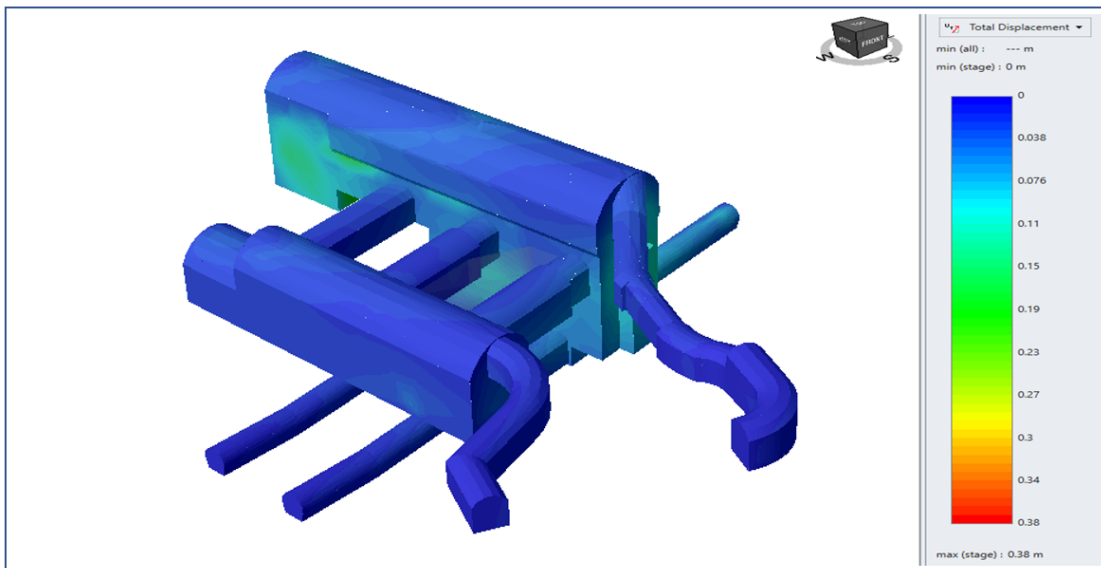


Figure 6.2: Displacements in the north wall and down stream wall

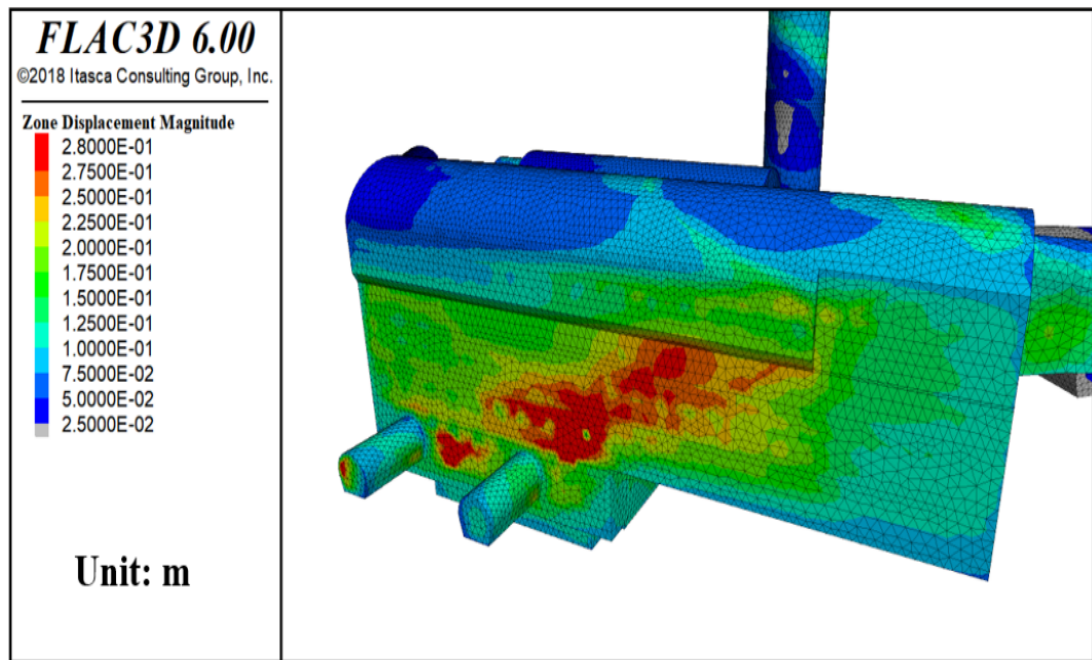


Figure 6.3: Displacements results obtained from FLAC 3D code.

A comparison between the results of Flac 3d code and RS3 code has been done for five different sections during the stages 6.4. The outputs in the two models are compatible within the excavation stages, as shown in figures from 6.6 to 6.14.

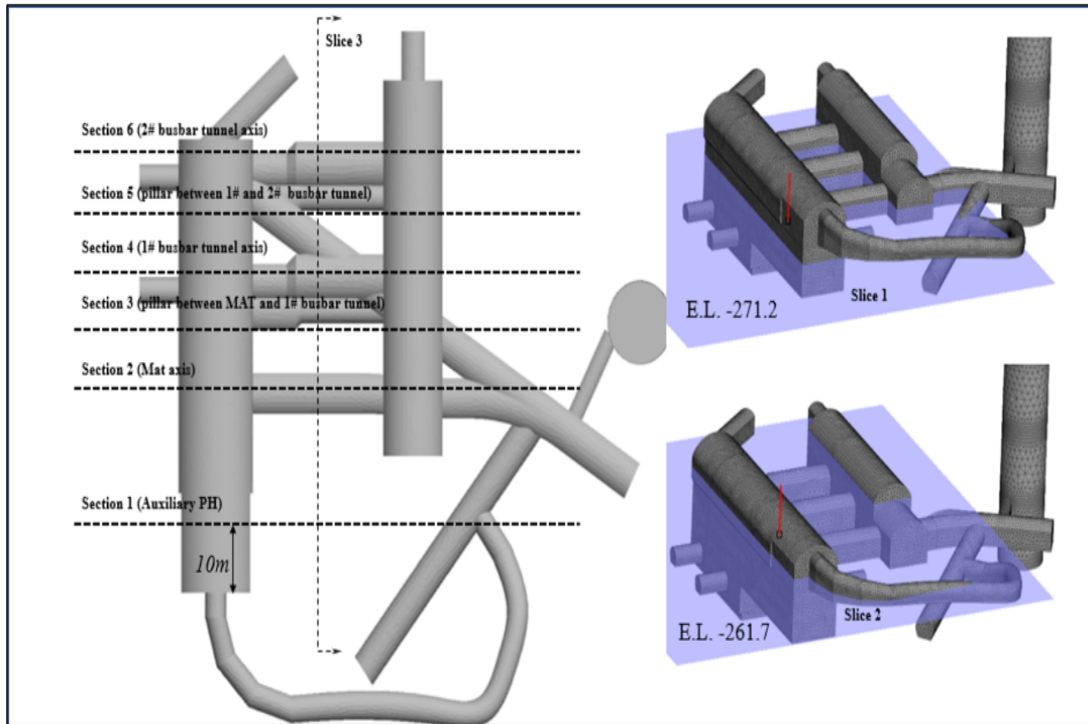


Figure 6.4: Different sections for the presentation of the results.

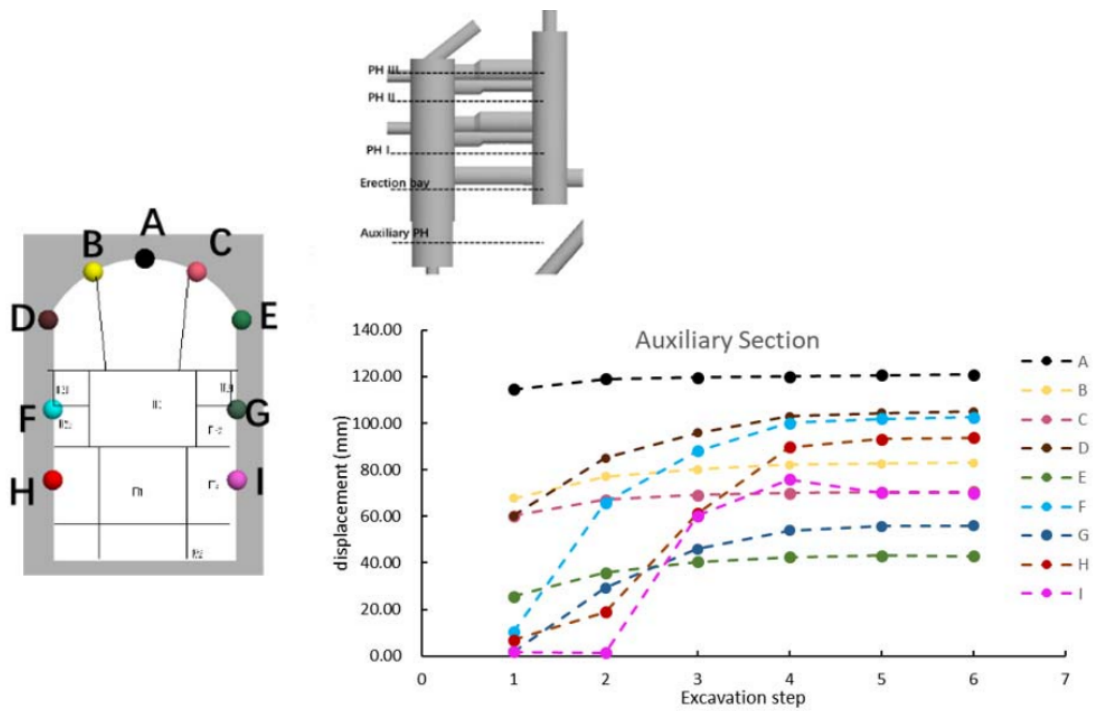


Figure 6.5: The displacement curve of the section auxiliary PH in FLAC 3D.

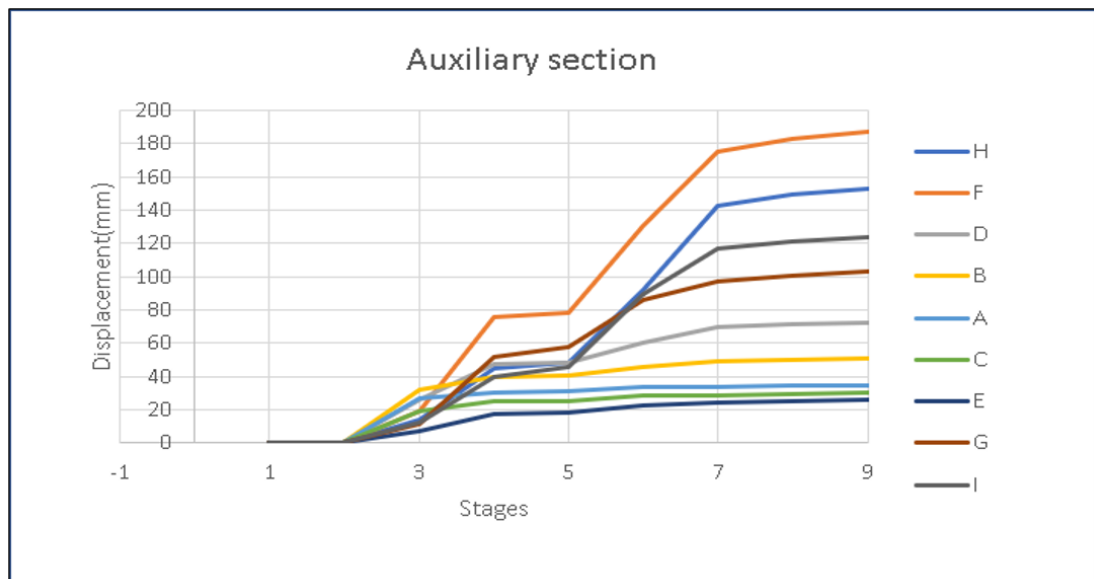


Figure 6.6: The displacement curve of the section auxiliary PH in RS3.

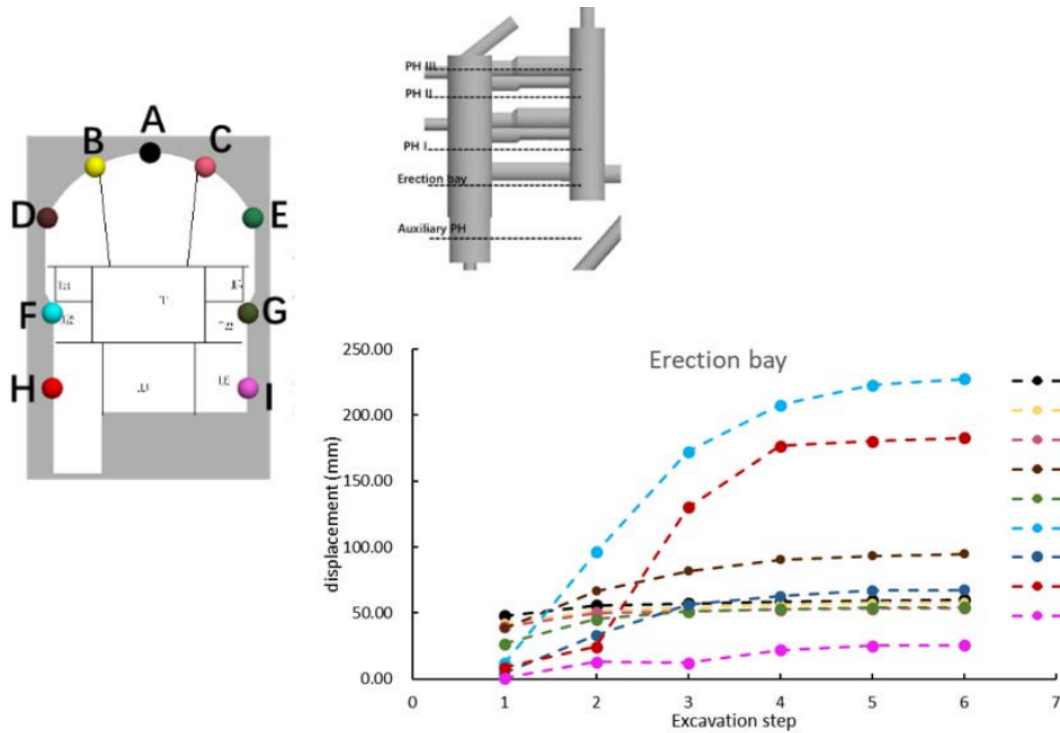


Figure 6.7: The displacement curve of the section erection bay in FLAC 3D.

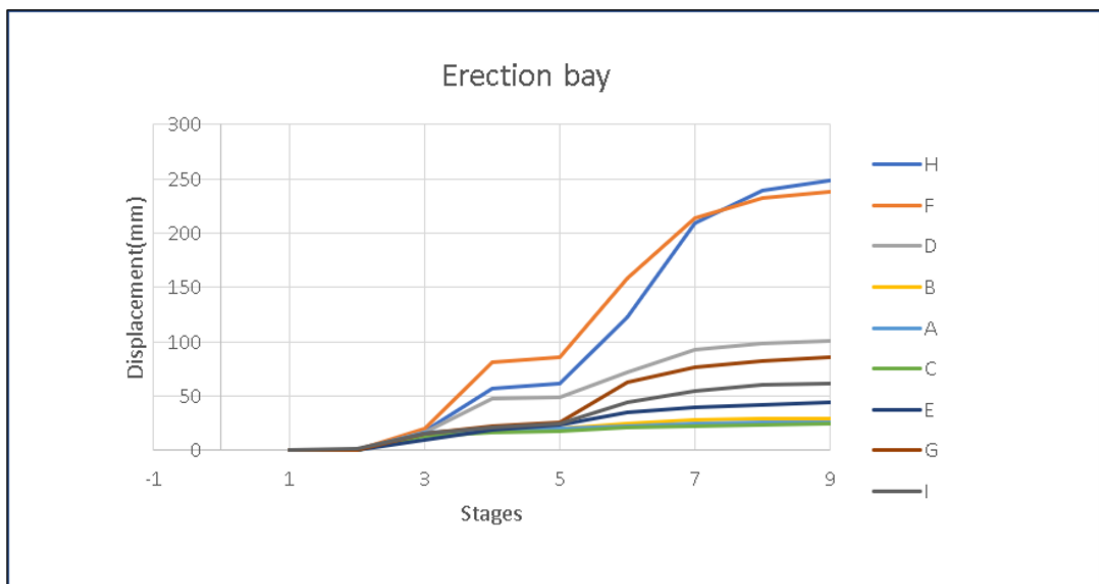


Figure 6.8: The displacement curve of the section erection bay in RS3 3D.

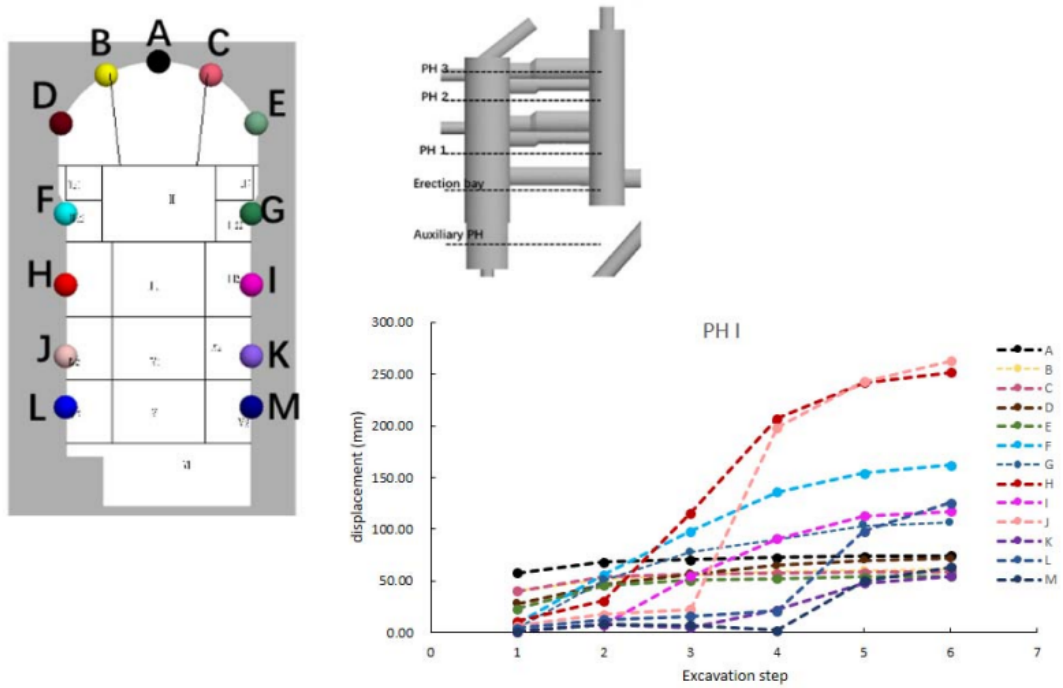


Figure 6.9: The displacement curve of the section PH I in FLAC 3D.

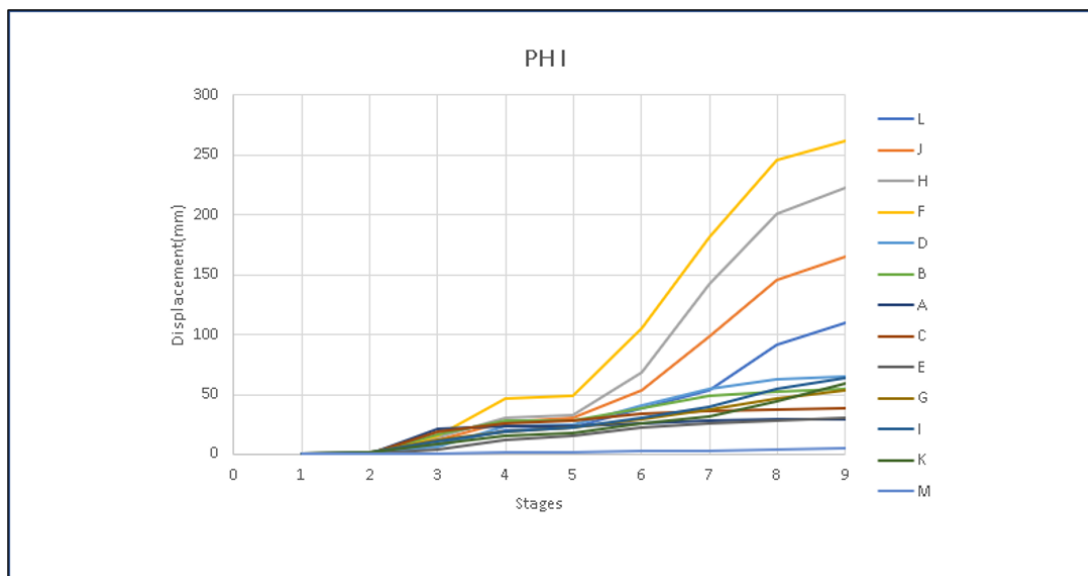


Figure 6.10: The displacement curve of the section PH I in RS3 3D.

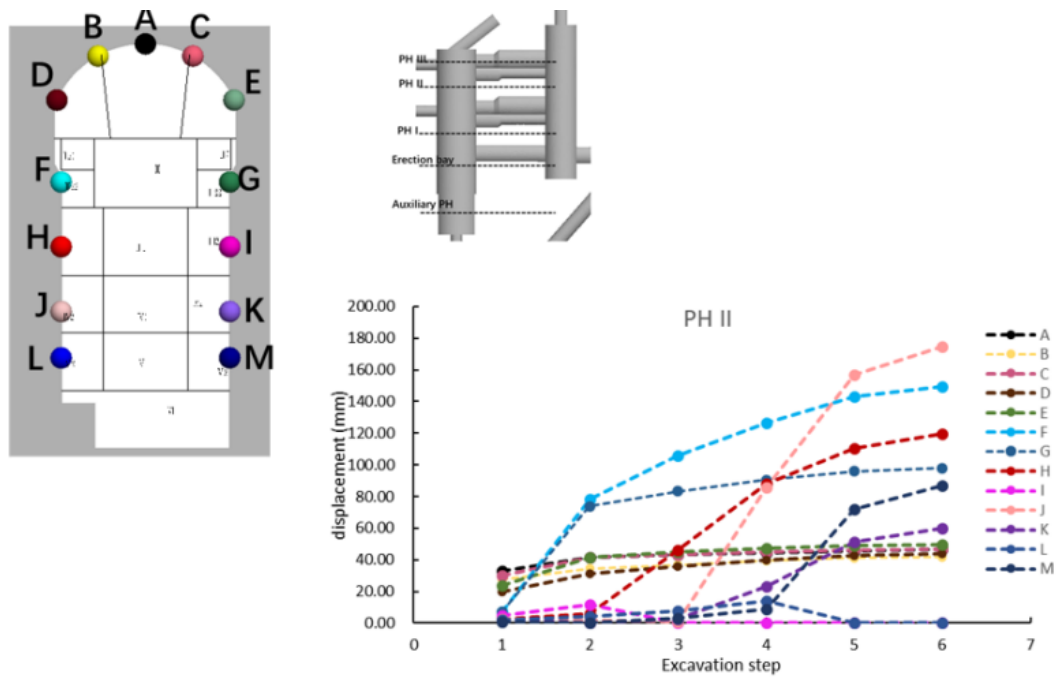


Figure 6.11: The displacement curve of the section PH II in FLAC 3D.

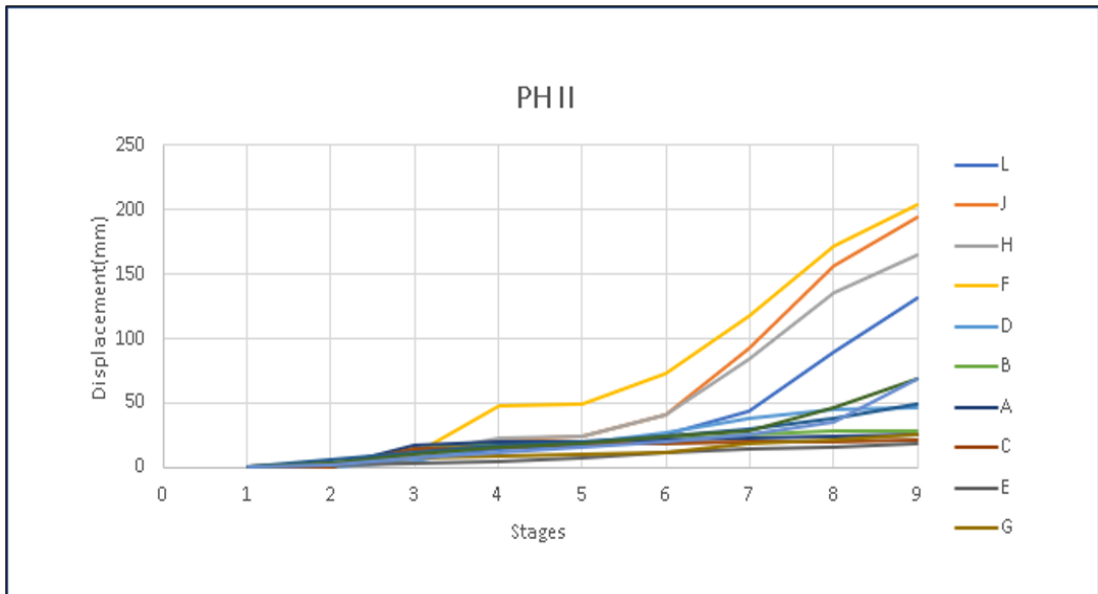


Figure 6.12: The displacement curve of the section PH II in RS3 3D.

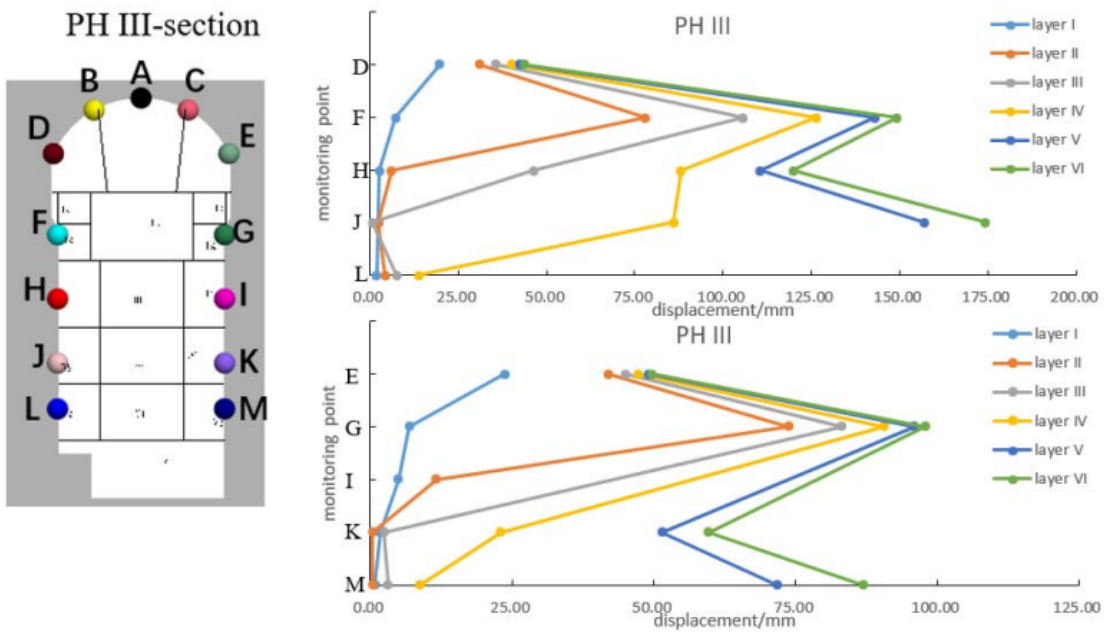


Figure 6.13: The displacement curve of the section PH III in FLAC 3D.

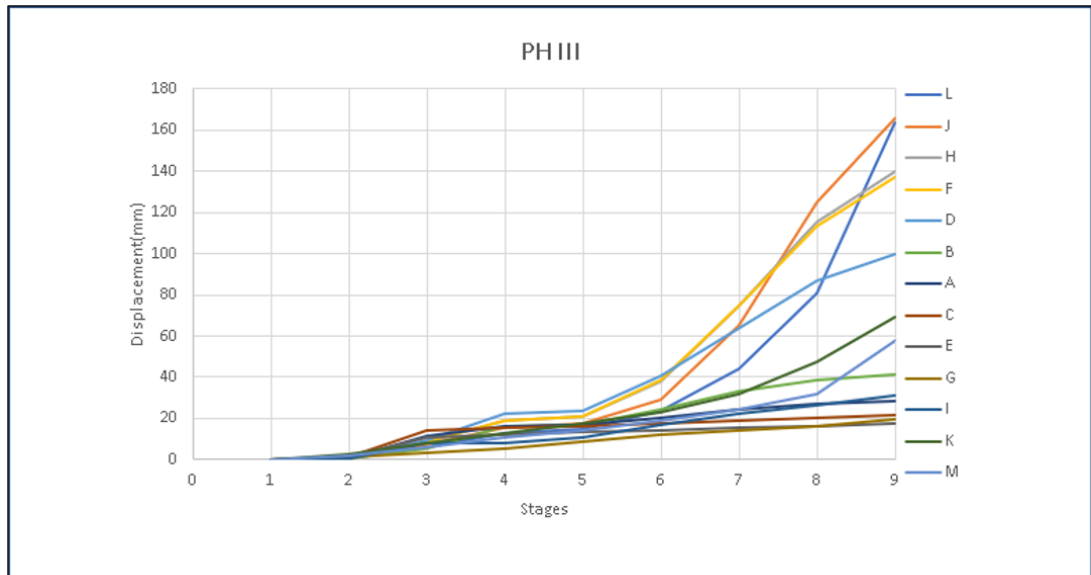


Figure 6.14: The displacement curve of the section PH III in RS3 3D.

## 6.2 Axial forces in tendons and bar anchors

In this section, the axial forces on tendons and bar anchors obtained by both FLAC 3D and RS3 analyses are shown in figures 6.15 , 6.16 and 6.17. The maximum value reaches 180 tons in both models, located in correspondence to the intersection of the fault 22, pyroclastic layer 9, class V with the upstream sidewall, as expected. Moreover, the other tendons are subjected to forces in the range of 70-150 tons.

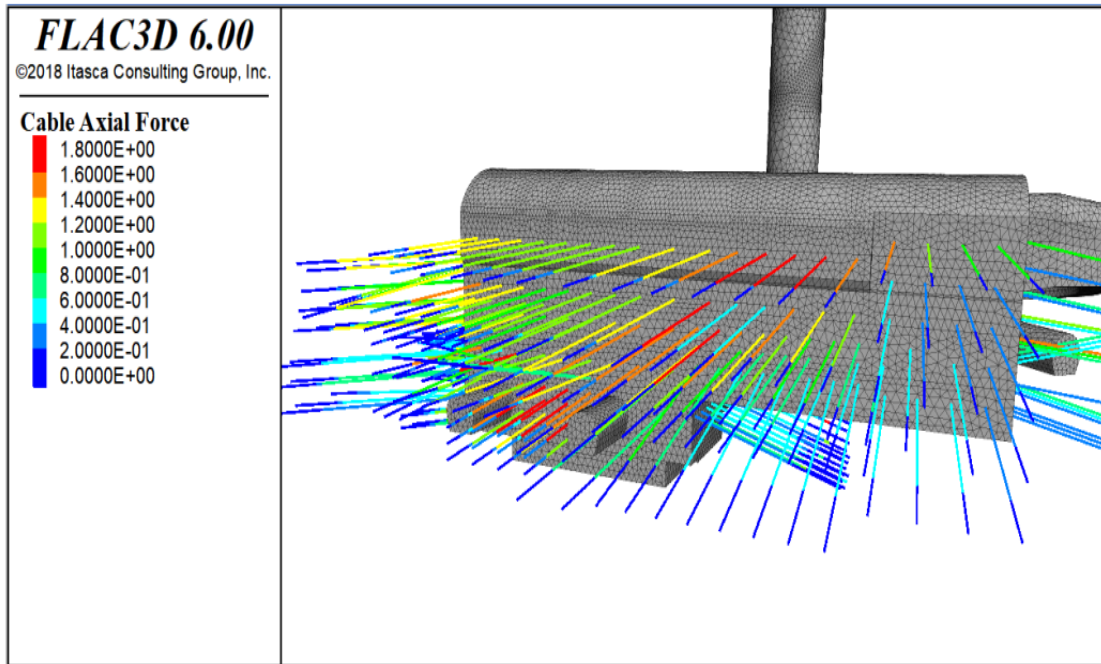


Figure 6.15: The force of tendons in FLAC 3D.

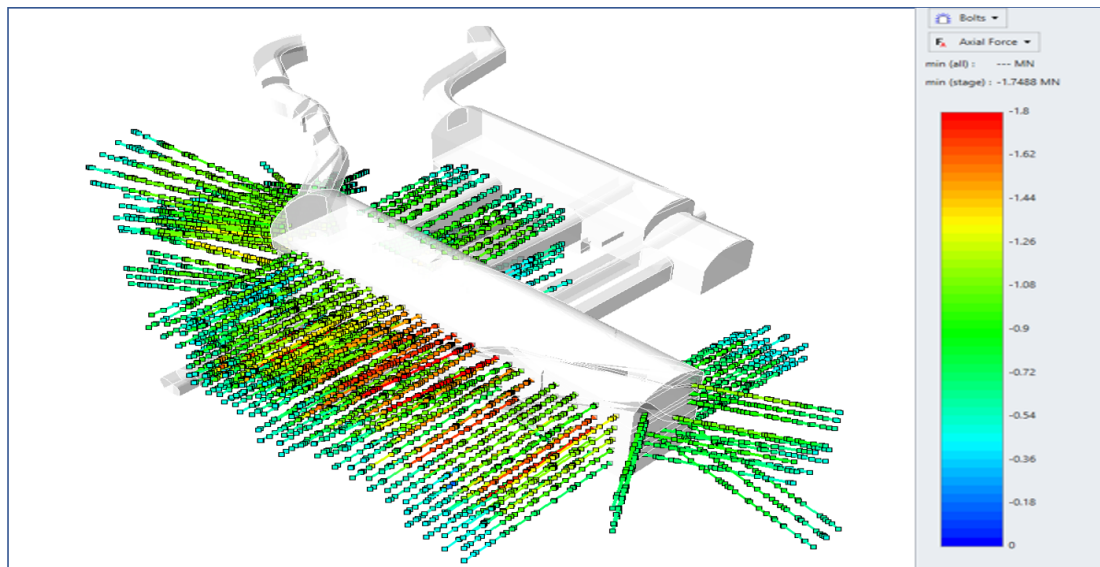


Figure 6.16: The tendons axial force in RS3.

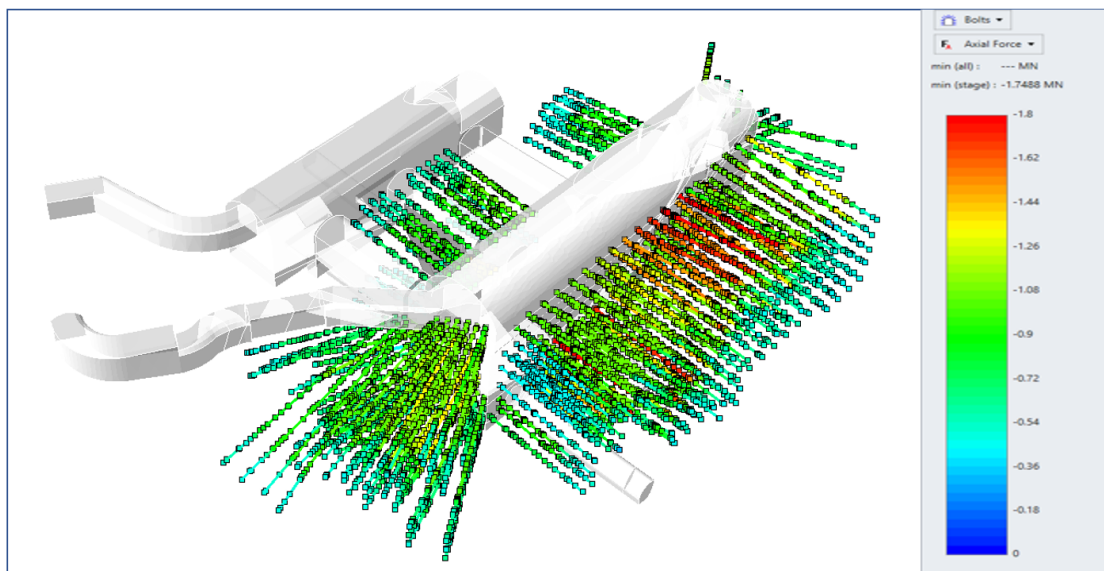


Figure 6.17: The tendons axial force in RS3.

### 6.3 Stresses in rock dowels

The results in terms of stresses are clarified in figures 6.18 to 6.20. Rock bolts located in the RS3 model in the upstream reach the maximum capacity, in contrary to the FLAC code results. In addition, not only the upstream sidewall but also the intersection between the pyroclastic layers and the excavation contour. In general stresses in FLAC code is around 365MPa, lower than the stresses in RS3 code (above 500 MPa). The reason could be that, in RS3 model, the rock dowels are installed layer by layer and activated at the same stage of the excavation. Thus, this could lead to an overestimation of the stress on the elements.

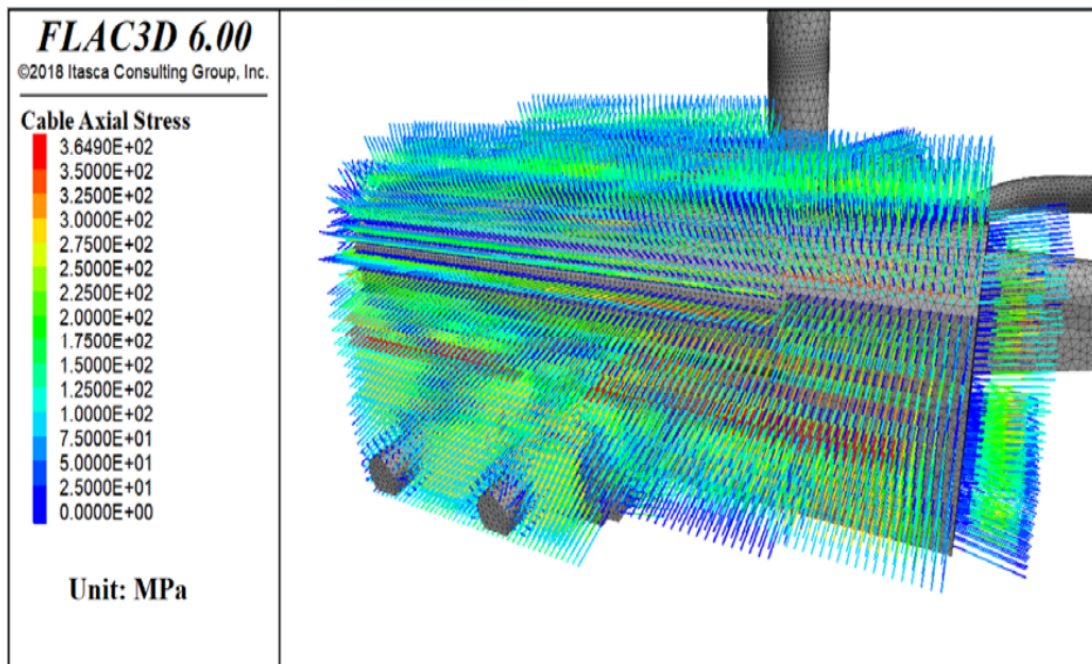


Figure 6.18: Stress of rock bolts in Flac 3D.

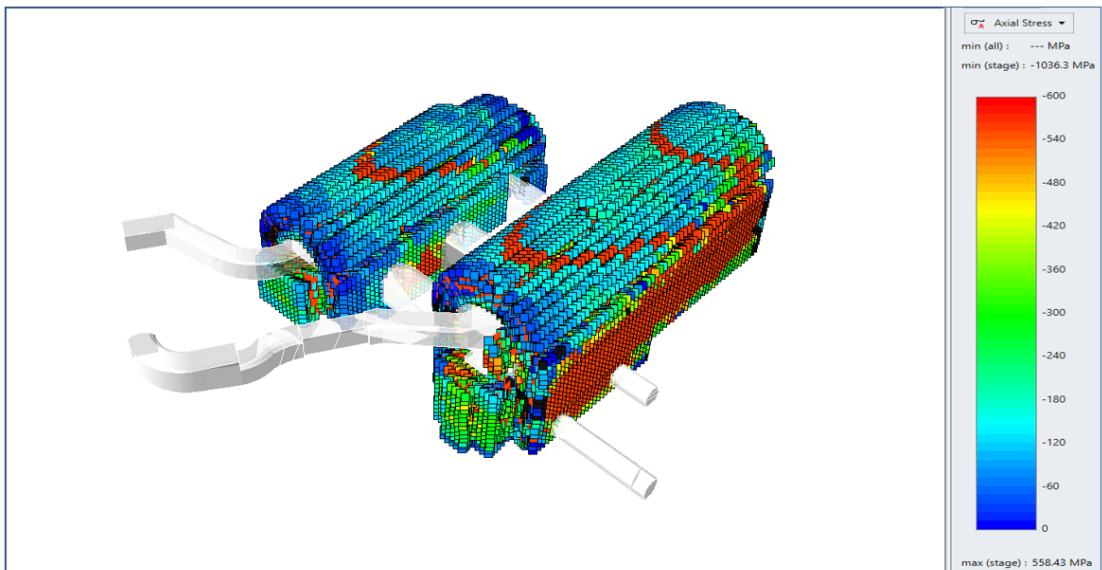


Figure 6.19: Stress of rock bolts in RS3 .

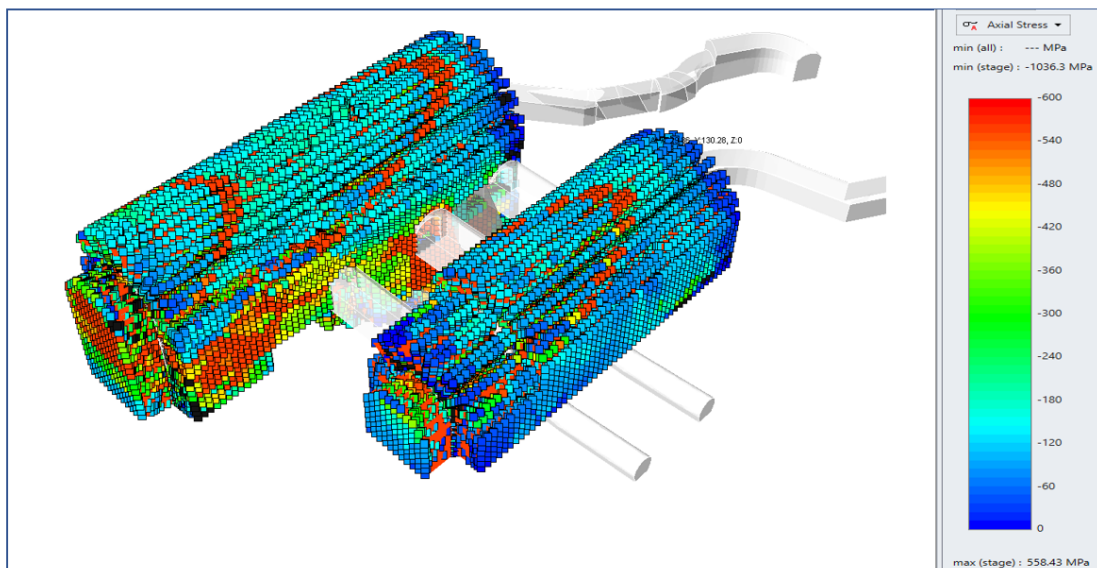


Figure 6.20: Stress of rock bolts in RS3.

## 6.4 Plastic zones

The comparison between the two models in terms of the plastic zones nearby the excavation contour is shown in figures from 6.21 to 6.31. The disturbance and the damage effect duo to the excavation are compatible and coherent between the models for different cross and longitudinal sections, even on the geological weak layers (faults and pyroclastic layers).

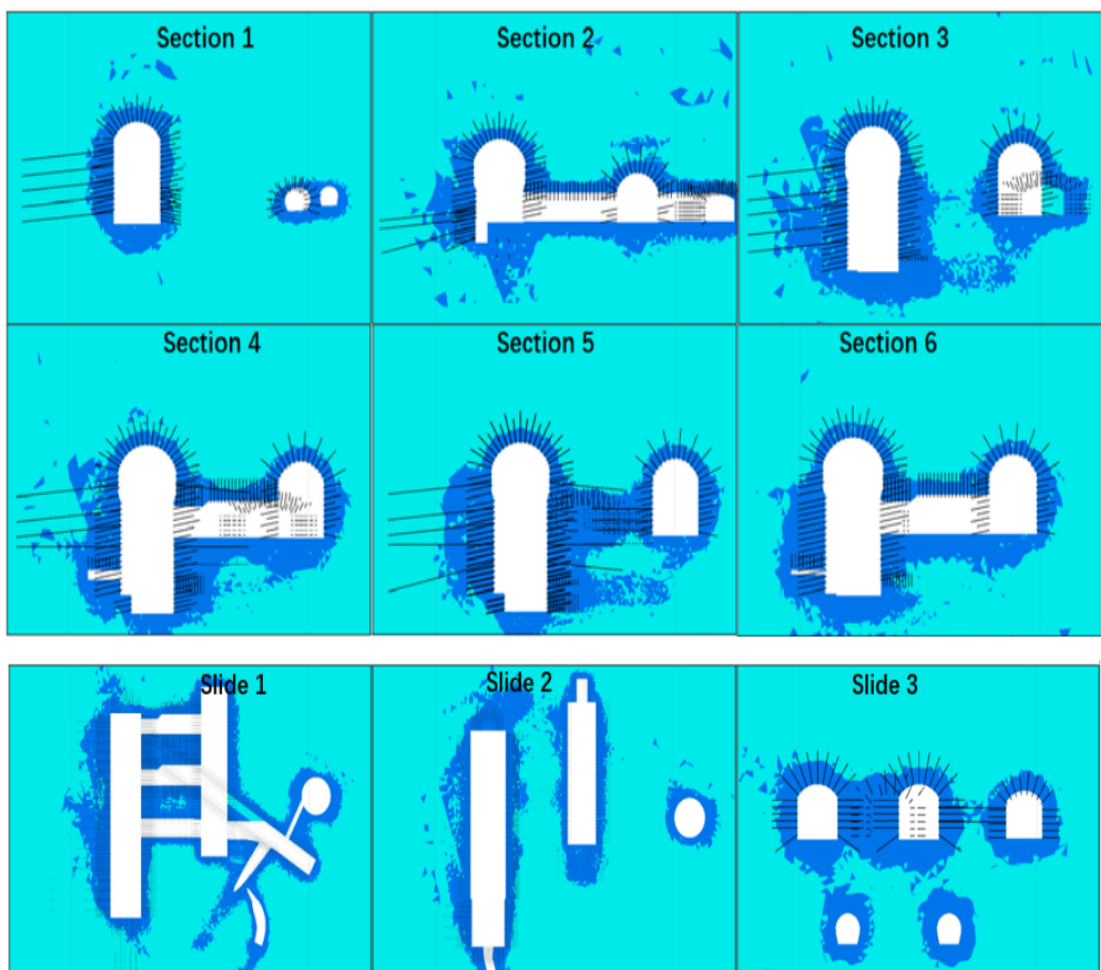
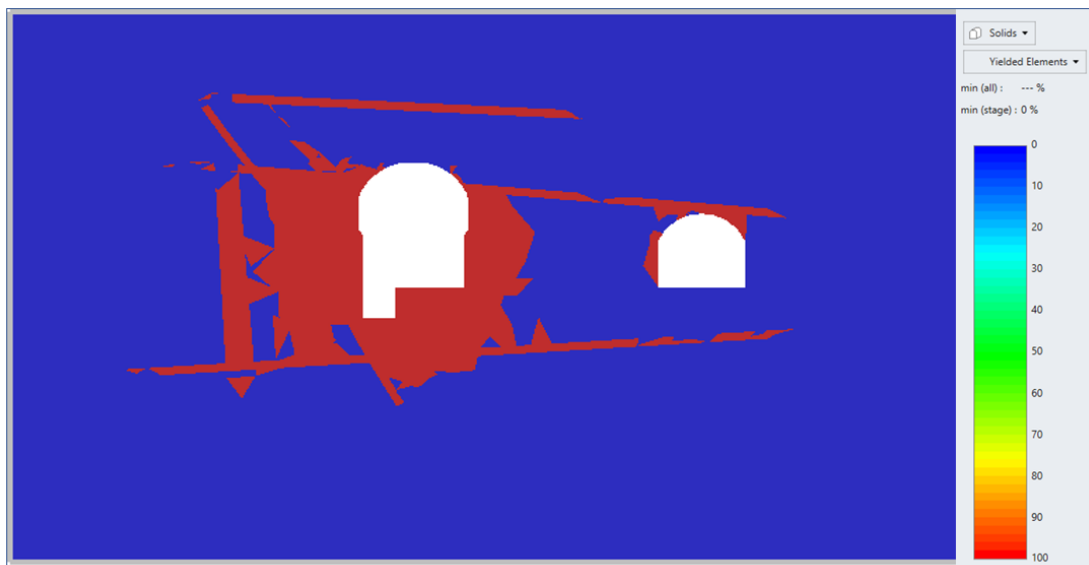


Figure 6.21: Plastic zones in FLAC 3D.



**Figure 6.22:** Auxiliary section Plastic zone in RS3 .



**Figure 6.23:** Erection bay section plastic zone in RS3.

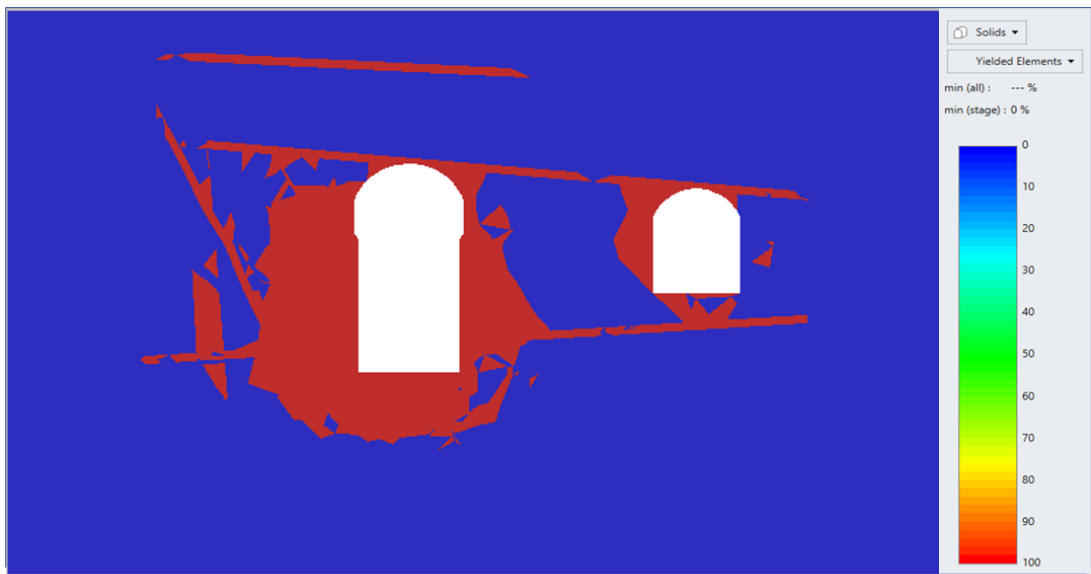


Figure 6.24: PH I section plastic zone in RS3.

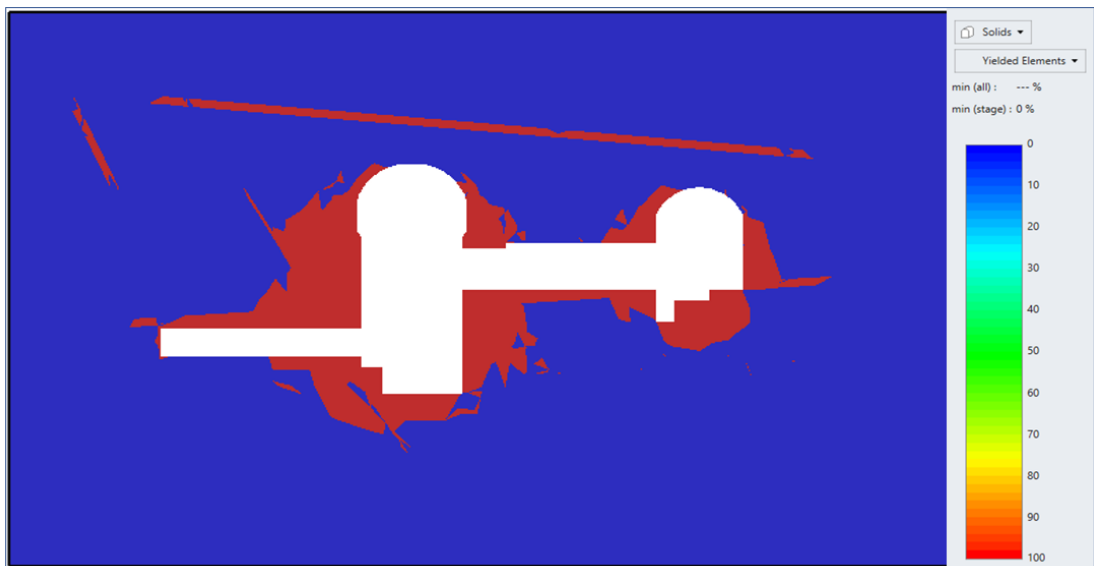


Figure 6.25: PH II section plastic zone in RS3.

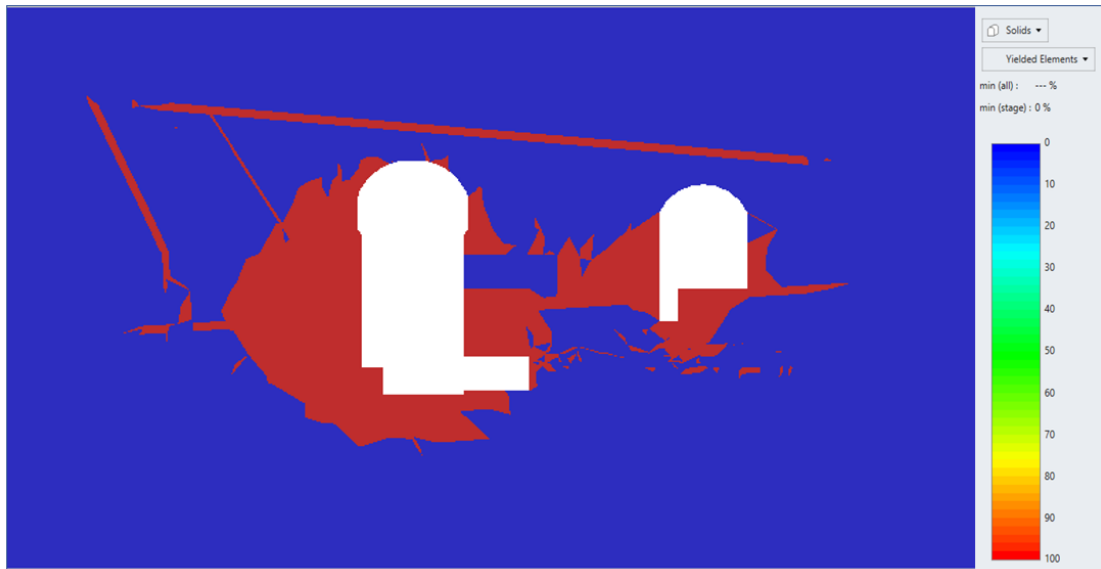


Figure 6.26: PH III section plastic zone in RS3

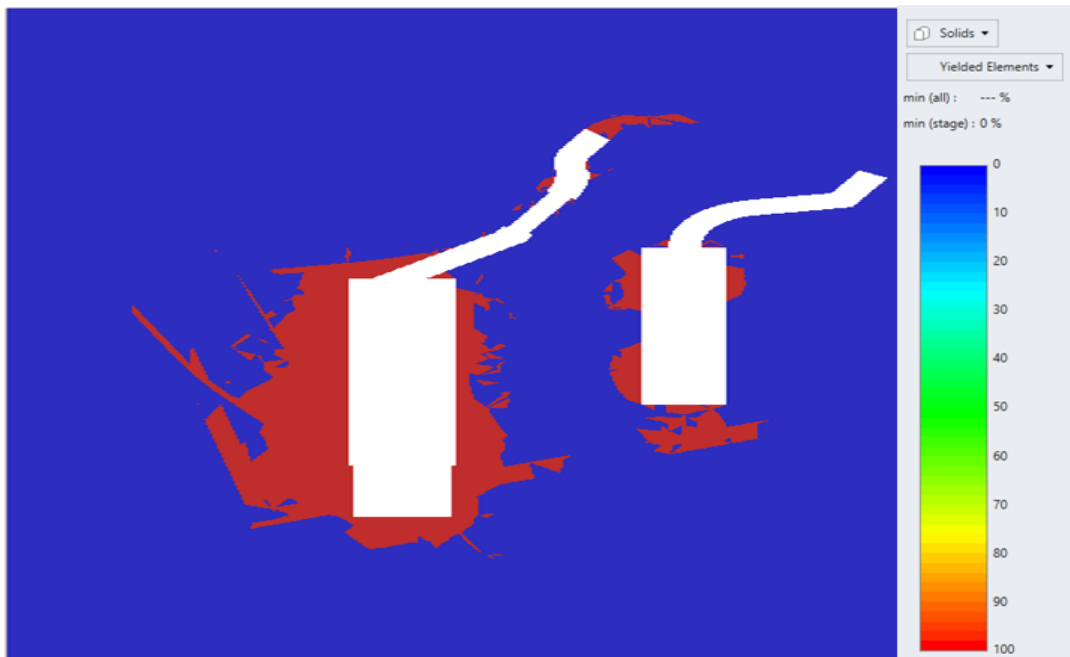


Figure 6.27: Slice 1 section plastic zone in RS3.

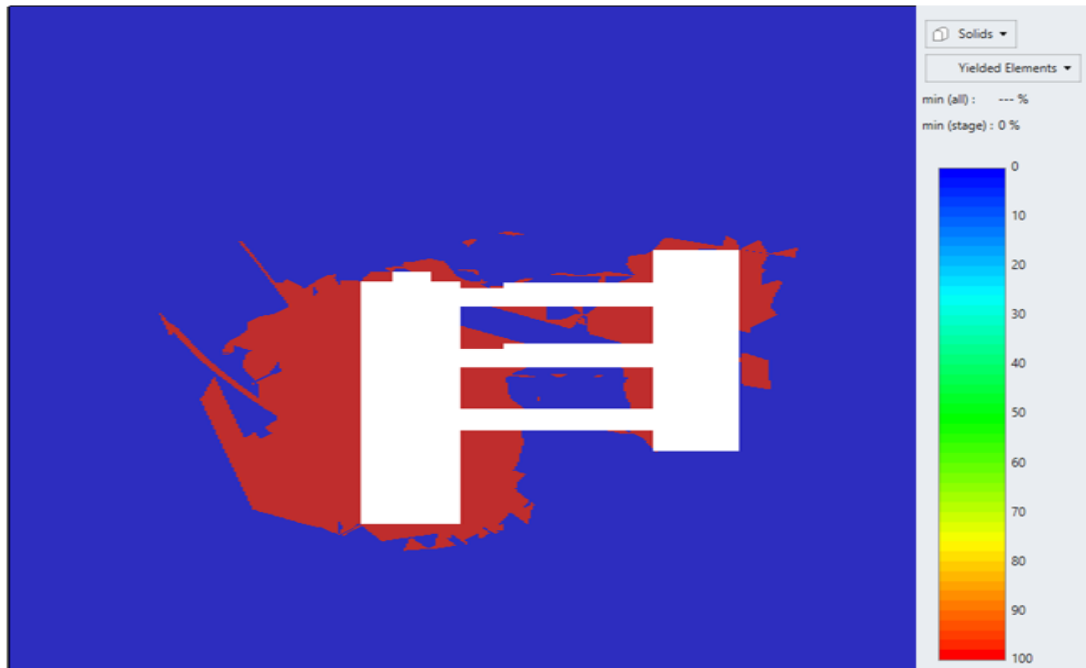


Figure 6.28: Slice 2 section plastic zone in RS3.

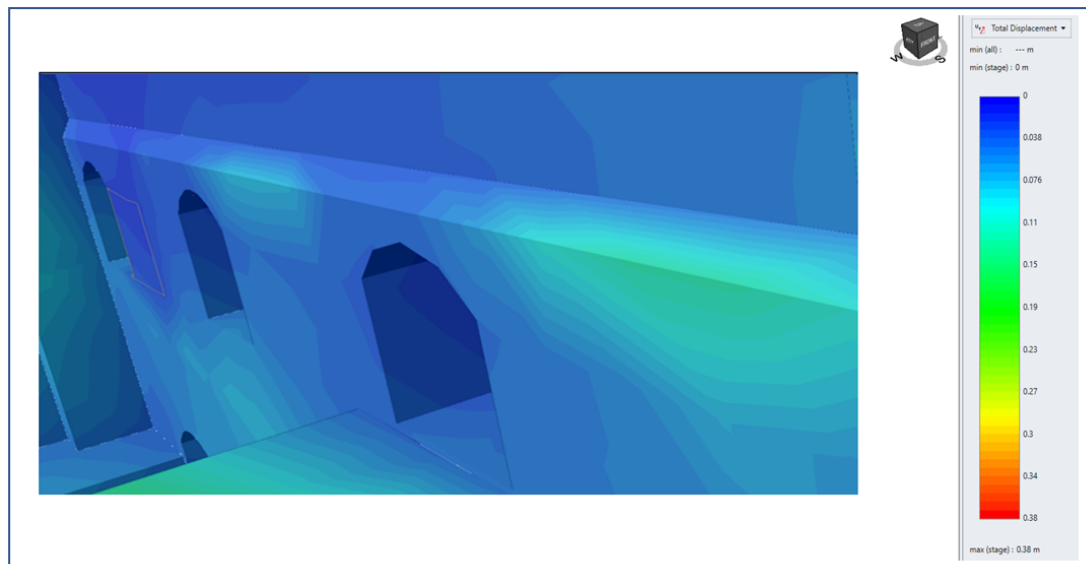


Figure 6.29: Intersection between the PH and the bus bar tunnels.

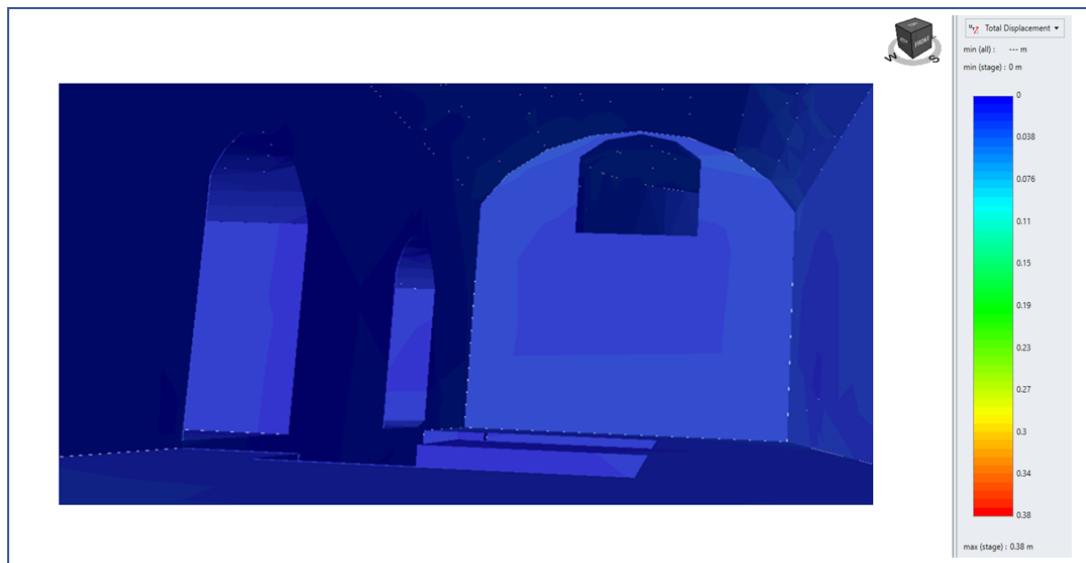


Figure 6.30: Intersection between the TH and the mat.



Figure 6.31: The view inside the mat.



**Table 6.1:** Results of the monitoring load cells and RS3 outputs on up stream side wall.

Axial force of anchors on upstream side wall(KN)		
Element	Monitoring system	RS3 results
DPph-21-R49U	807	523
DPph-5-R34U	747	1855
DPph-8-R21U	689	1686
DPph-10-R15U	522	1334
DPph-12-R0U	782	944
DPph-15-L12U	580	918
DPph-17-L22U	716	1031
DPph-19-L30U	627	606
DPph-29-R30U	467	1890
DPph-32-R17U	448	1890
DPph-35-R0U	709	1786
DPph-38-L13U	524	1365
DPph-512-L23U	741	1625
DPph-50-R22U	815	1380
DPph-44-R49U	286	436
DPph-add-R33U	295	163
DPph-522-R15U	579	1874
DPph-67-R0U	361	582
DPph-70-L13U	456	1743
DPph-79-L16U	485	1281
DPph-73-L27U	361	436
DPph-547-L13U	569	922

The representative anchors equipped with load cells on the downstream sidewall of PH are shown in figure 6.34.

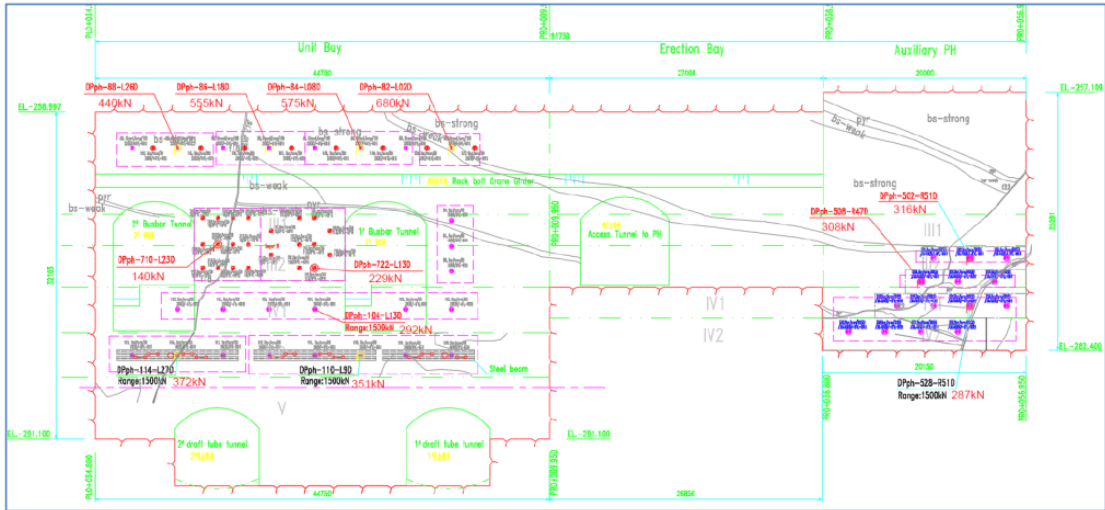


Figure 6.34: Load cells distribution on down stream side wall.

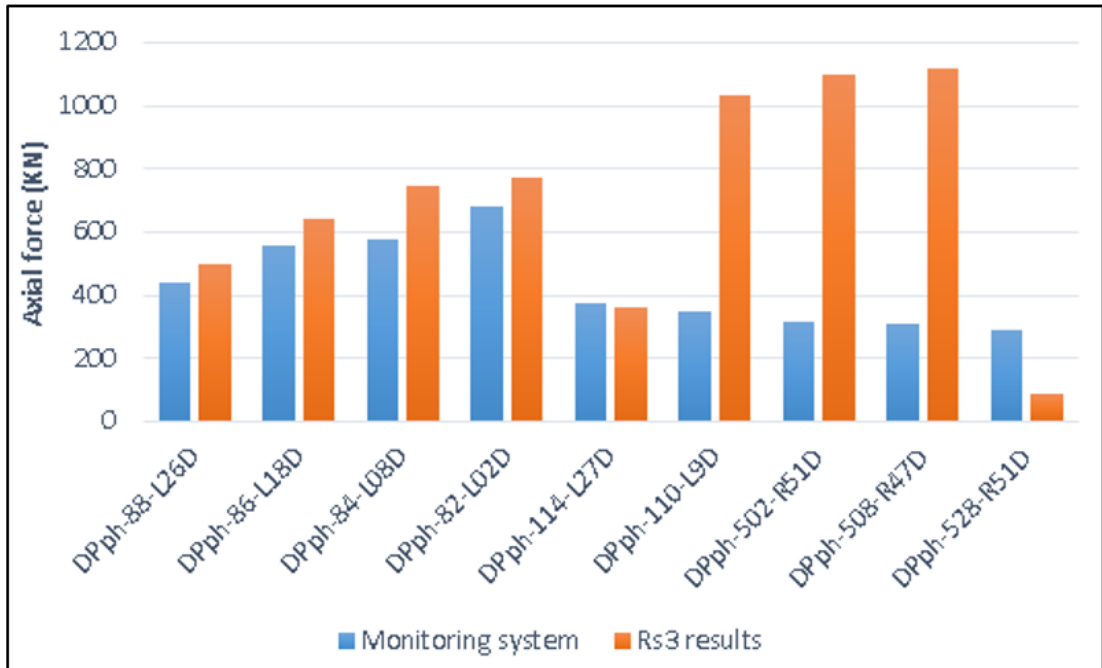


Figure 6.35: Comparison between RS3 results and Monitoring system on down stream side wall.

**Table 6.2:** Results of the monitoring load cells and RS3 outputs on down stream side wall.

Axial force of anchors on down stream wall(KN)		
Element	Monitoring system	Rs3 results
DPph-88-L26D	440	497
DPph-86-L18D	555	642
DPph-84-L08D	575	749
DPph-82-L02D	680	774
DPph-114-L27D	372	360
DPph-110-L9D	351	1034
DPph-502-R51D	316	1099
DPph-508-R47D	308	1119
DPph-528-R51D	287	85

The representative anchors of load cells on the north and south wall are shown in figure 6.36.

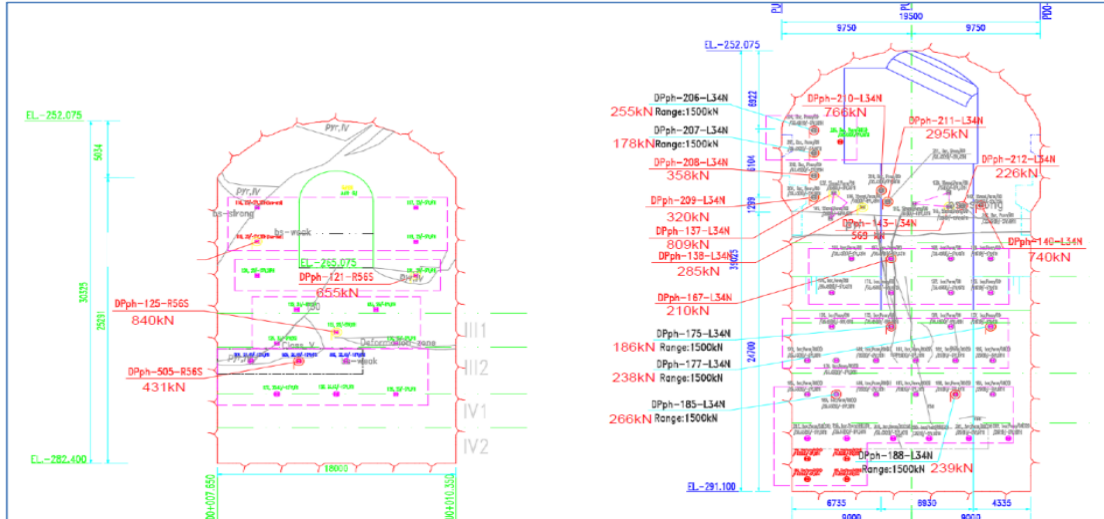


Figure 6.36: Load cells distribution on north and south wall.

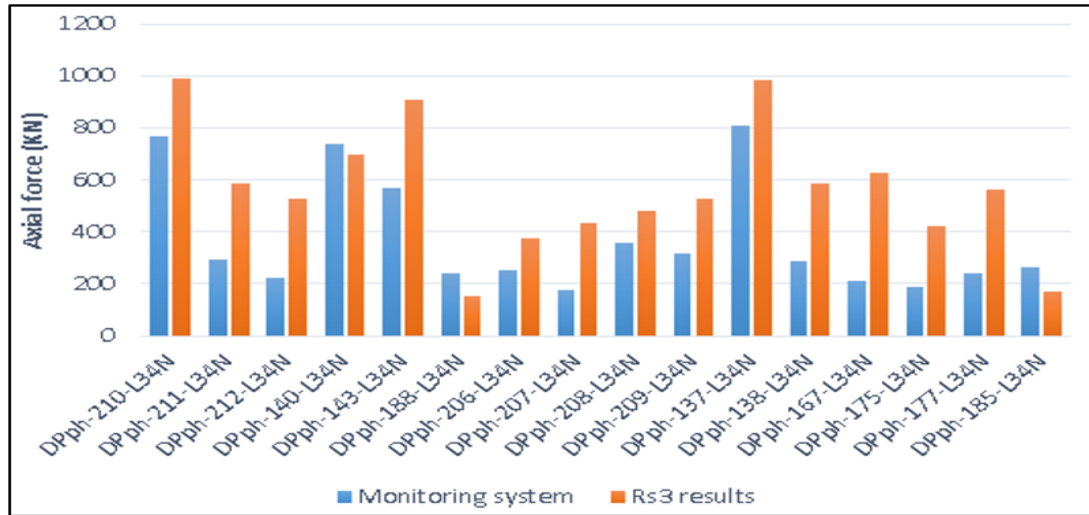
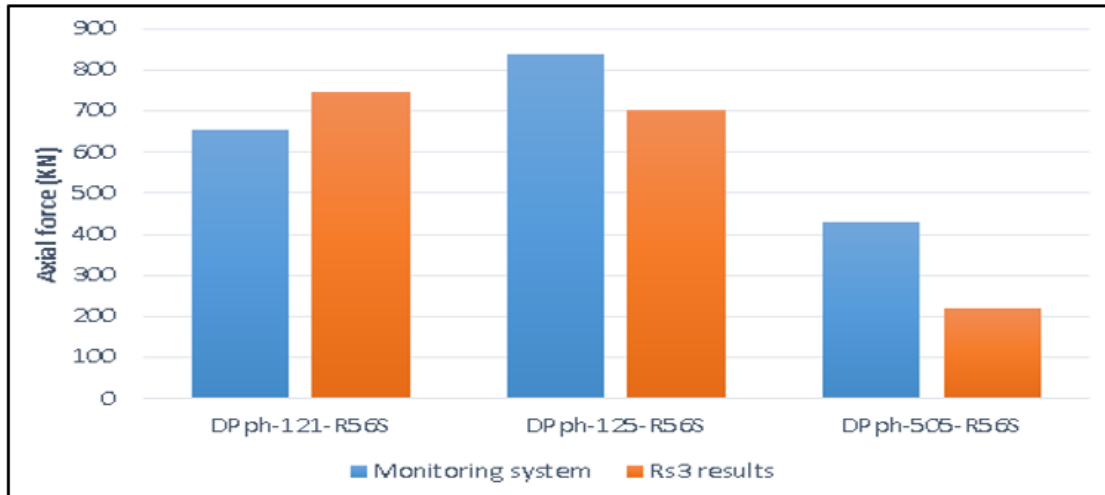


Figure 6.37: Comparison between RS3 results and Monitoring system on north wall.

**Table 6.3:** Results of the monitoring load cells and RS3 outputs of the north wall.

Axial force of anchors on north wall(KN)		
Element	Monitoring system	Rs3 results
DPph-210-L34N	766	990
DPph-211-L34N	295	589
DPph-212-L34N	226	526
DPph-140-L34N	740	695
DPph-143-L34N	569	909
DPph-188-L34N	239	155
DPph-206-L34N	255	377
DPph-207-L34N	178	431
DPph-208-L34N	358	479
DPph-209-L34N	320	526
DPph-137-L34N	809	983
DPph-138-L34N	285	589
DPph-167-L34N	210	630
DPph-175-L34N	186	423
DPph-177-L34N	238	564
DPph-185-L34N	266	170



**Figure 6.38:** Comparison between RS3 results and Monitoring system on south wall.

**Table 6.4:** Results of the monitoring load cells and RS3 outputs of the south wall.

Axial force of anchors on south wall(kN)		
Element	Monitoring system	Rs3 results
DPph-121-R56S	655	748
DPph-125-R56S	840	701
DPph-505-R56S	431	221

From previous figures and charts, it is clear that. The results that are obtained from RS3 code are higher than the monitoring data. In fact, load cells (DPph-110-L9D-DPph-502-R51D-DPph-508-R47D) on the downstream side wall have outputs around 320 KN, while, the RS3 results are around 1000 KN. This difference gives an indication about the low reliability of RS3 results, due to local missing of data. It should be also pointed out that the rock mass quality and the geological condition are not homogenous, so the numerical model is not able to match the monitor data of each device.

# Chapter 7

## time dependent behavior of rock mass

### 7.1 Introduction

In this chapter, the long-term deformational behavior of the rocks masses has been studied to forecast the hydro power plant stability within the next 50 years. Two approaches have been used. The first approach [5] was provided by Aydan et al .in 1993, in which the stress-strain behaviour of rock mass is analysed.The second one [6],proposed by Barla and Borgna in 2000, suggests to reduce the strength parameters as a function of strain levels. Moreover, using these two approaches is a solution to overcome a considerable limit of the RS3 code which can not handle time-dependent behavior like FLAC 3D code.

### 7.2 Prediction of the stress-strain behaviour of rock mass

The calculation of the proposed method is based on a crucial concept : the analogy between the axial stress-strain response of rock in laboratory tests and tangential stress-strain response of rock surrounding tunnels. The results of experiments clarified that five phases of rock behaviour during a complete testing process have been distinguished. These five phases are shown in figure7.1. Their descriptions is summarized as:

- 1-Elastic phase: the behavior of the rock is linear and no crack is observed.
- 2-Yielding phase: micro- cracks tend to merge and convert to macro-cracks after surpassing the peak of the stress-strain curve.
- 3-Hardening phase: the occurrence of macro-cracks started and their orientation

has the direction of maximum load.

4-Weakening phase: growth of macro-cracks, which are aligned in the most critical orientation.

5-Flowing phase: macro-cracks form sliding planes or bands, and fractured materials flow along these planes.

Based on the statistical analysis of the relationship between rock resistance and deformation conditions, Aydan derived the following empirical relationships: .

$$\eta_p = \frac{\epsilon_p}{\epsilon_e} = 2\sigma_c^{-0.17} \quad (7.1)$$

$$\eta_s = \frac{\epsilon_s}{\epsilon_e} = 3\sigma_c^{-0.25} \quad (7.2)$$

$$\eta_f = \frac{\epsilon_f}{\epsilon_e} = 5\sigma_c^{-0.32} \quad (7.3)$$

Where:  $\eta_p, \eta_s, \eta_f$  = normalizes peak, weakening and final deformations.

$\epsilon_e, \epsilon_p, \epsilon_s, \epsilon_f$  = elastic, peak, weakening and final strain values.

$\sigma_c$  = monoaxial compressive strength of the rock, this value is also considered representative of the storage resistance.

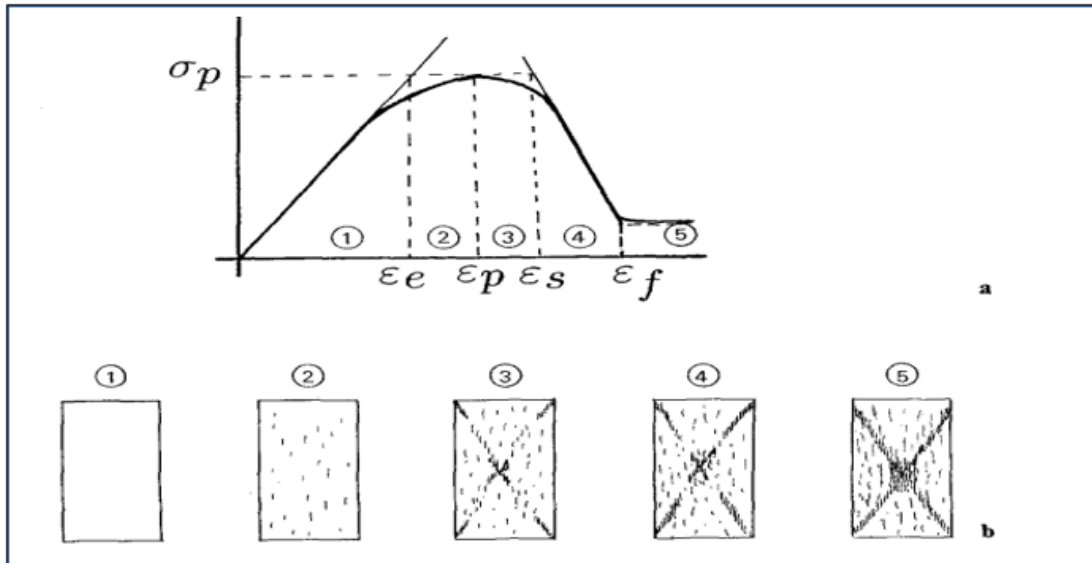


**Figure 7.1:** Idealised stress-strain curves and associated states

[5]

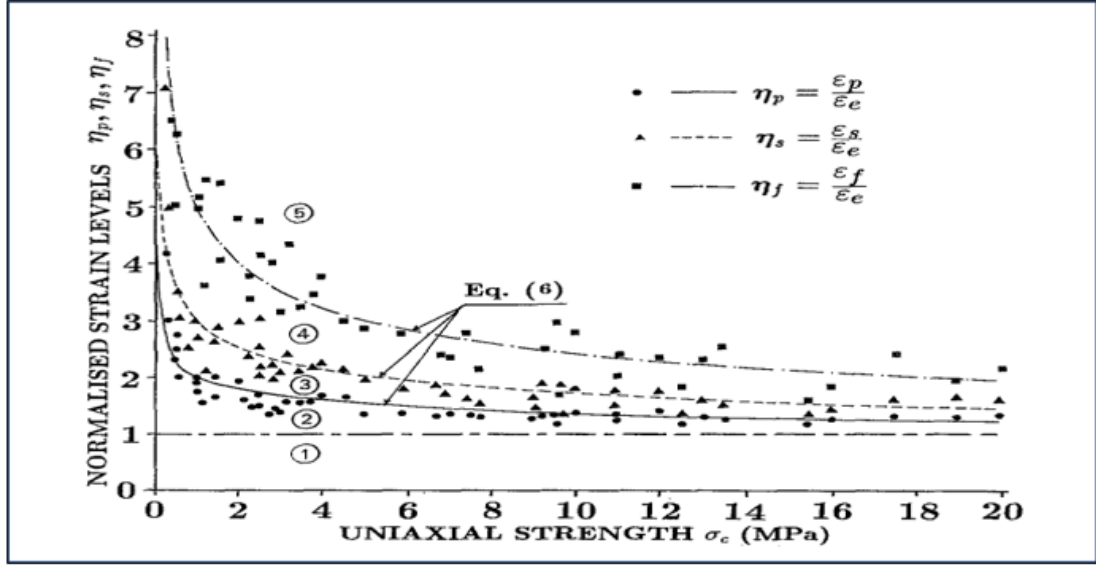


**Figure 7.2:** Experimental relationship between rock resistance and normalized deformations.

[5]

For the generic extrapolation of the method to rock masses characterized by the criterion of Hoek and Brown, the problem arises of the choice of geomechanical resistance to be considered. The accentuated non-linearity of the Hoek and Brown breaking criterion and the considerable influence of confinement pressure, lead these authors to distinguish two types of cluster resistance :

- Monoaxial storage strength

$$\sigma_{cm} = \sigma_c * s^a \quad (7.4)$$

- the global cluster resistance, related to the Mohr-Coulomb linear envelope in the interval  $\sigma_t < \sigma_c < \sigma_c/4$

$$\sigma_{cm}(global) = 2c * \cos \phi / (1 - \sin \phi) \quad (7.5)$$

The global cluster resistance is related to the Hoek and Brown parameters with the equation proposed by Hoek et al. (2002):

$$\sigma_{cm}(global) = \sigma_c \cdot \frac{(m_b + 4s - a(m - b - 8s)) / (m_b/4 + s)^{a-1}}{2(1 + a)(2 + a)} \quad (7.6)$$

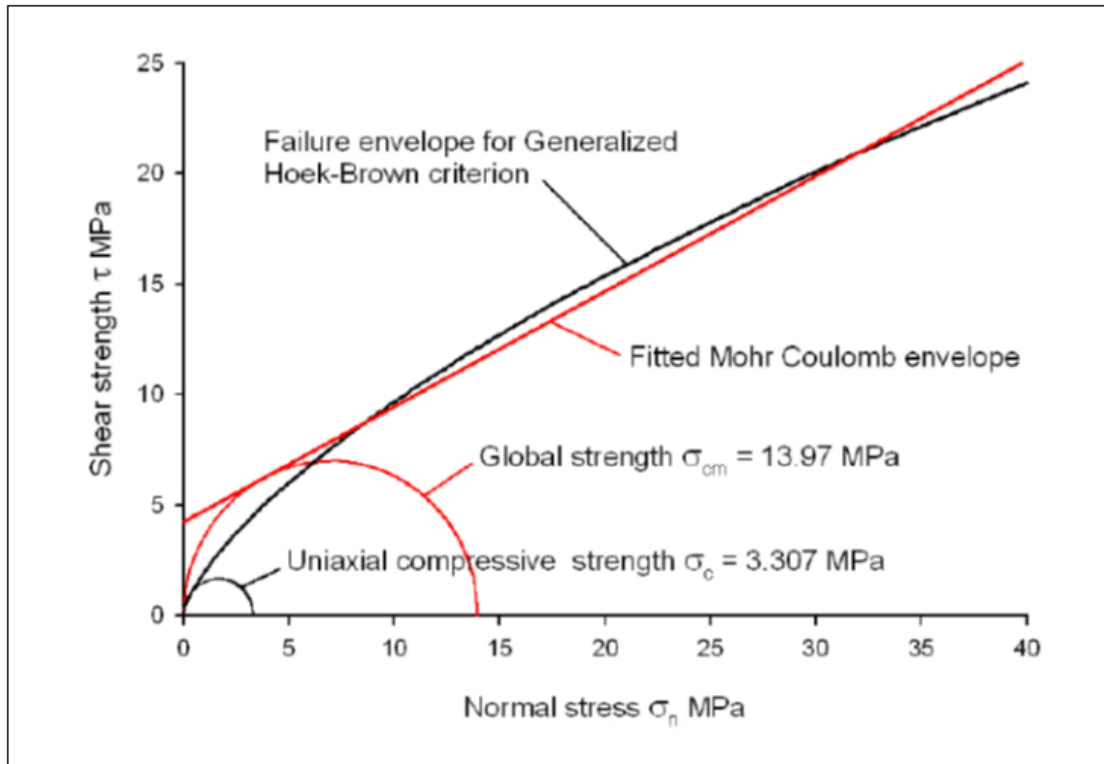


**Figure 7.3:** Hoek-Brown and Mohr-Coulomb envelopes and definition of uniaxial and global cluster resistance [7]

In the same article cited, it is highlighted that the monoaxial resistance of cluster defines the tensional state that originates the onset of fractures on the excavation contour, while the global resistance provides a more direct indication of the average resistance that can be mobilized by the cluster after propagation within the fractures. It is understood that the monoaxial resistance of cluster constitutes precisely the resistance in the absence of confinement derived from the Hoek-Brown rupture criterion (and as such is implicitly used in design calculations), we refer to the global resistance for the sole derivation of the characteristic deformations with the Aydan method. The deformations obtained are used to modify the real constitutive law of input in design calculations (initial conditions to modified conditions) [7].

Different strain values have been calculated to BS-strong class III, BS-weak class III, and BS-weak class IV as follows:

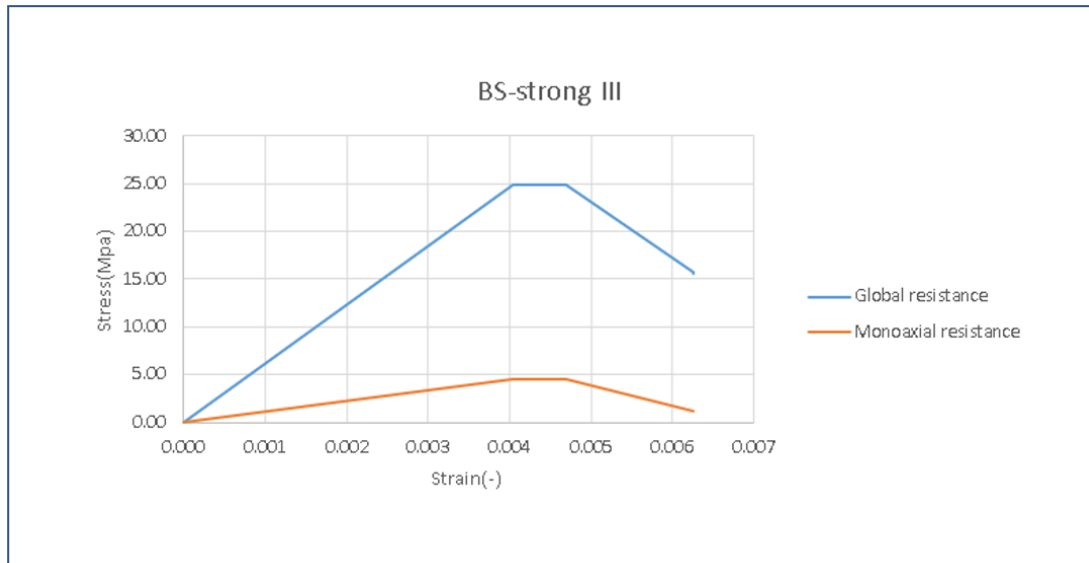


Figure 7.4: Stress-strain curve (BS-strong III).

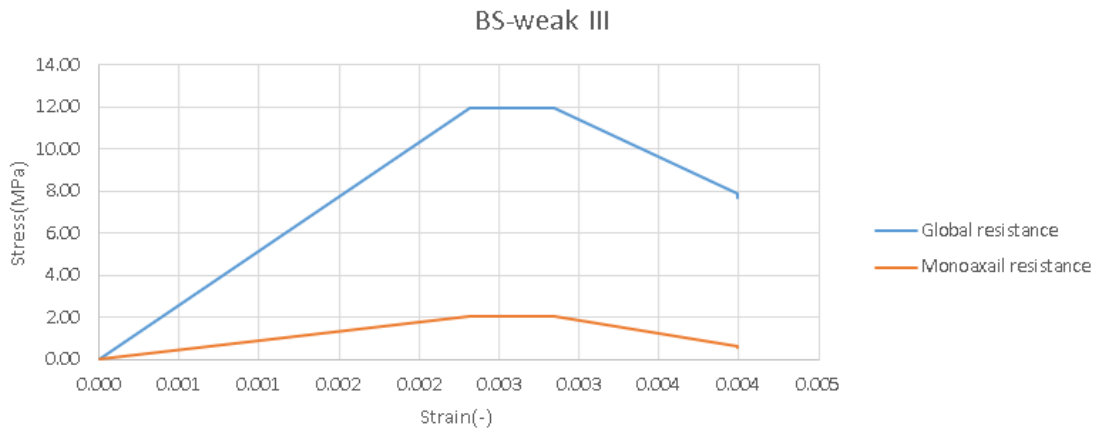
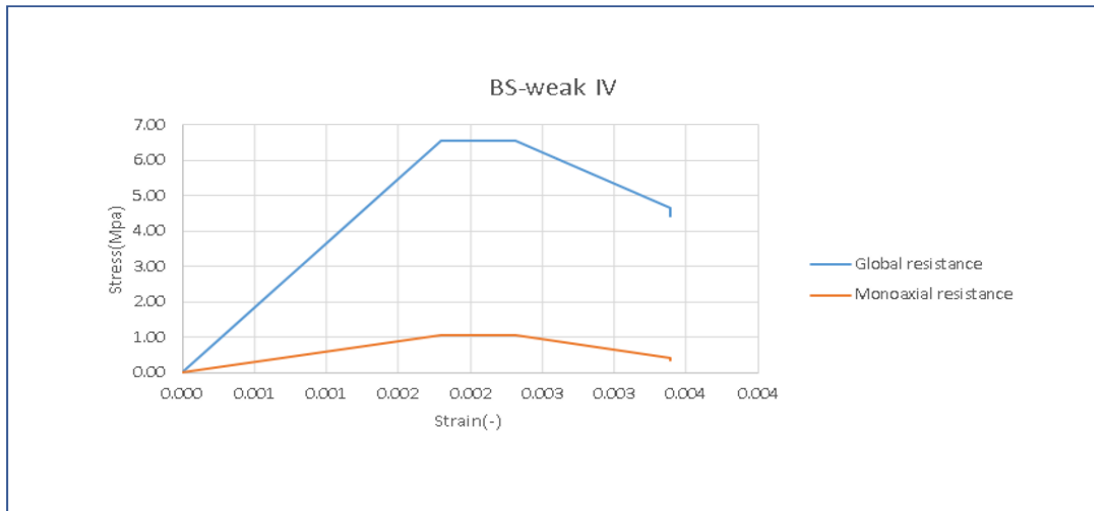


Figure 7.5: Stress-strain curve (BS-weak III).



**Figure 7.6:** Stress-strain curve (BS-weak IV).

**Table 7.1:** Stress-strain values.

Bs-strong III		BS-weak III		BS-weak IV	
Strain(-)	Stress(MPa)	Strain(-)	Stress(MPa)	Strain(-)	Stress(MPa)
0.000	0.00	0.000	0.000	0.000	0.000
0.004	24.87	0.002	11.967	0.002	6.553
0.005	24.87	0.003	11.967	0.002	6.553
0.006	15.67	0.004	7.857	0.003	4.659
0.006	15.50	0.004	7.677	0.003	4.414

### 7.3 Strength parameters update

In the second approach, the main purpose is to simulate the squeezing behavior in tunnels. Concerning three different stages of behavior: the elastic stage, up to the onset of time-dependent deformations; the hard-ending stage creep deformation; the softening stage, stress-strain law is applied. Validation of the results for stress-strain laws obtained in triaxial compression tests.

The most important factors influencing squeezing:

- 1- The yielding within the rock mass.
- 2- Time-dependent behavior.

Constitutive relationships such as elasto-plastic or elasto-visco-plastic are the most appropriate ones. Using these relationships is quite challenging, with respect to rock mass characterization. Moreover, the possibility to use elasto-visco plastic way is not supported by RS3 code.

As shown in the figure 7.7, there is no time-dependent behavior for stress values below the threshold value  $\sigma_t$ . On the other hand, stress values above  $\sigma_t$  and below  $\sigma_u$ , e.g.  $\sigma_E$ , creep is attenuating and stops at a finite strain  $\epsilon_f$ . The higher the applied stress and closer to the peak value, the shorter is the time to creep failure.

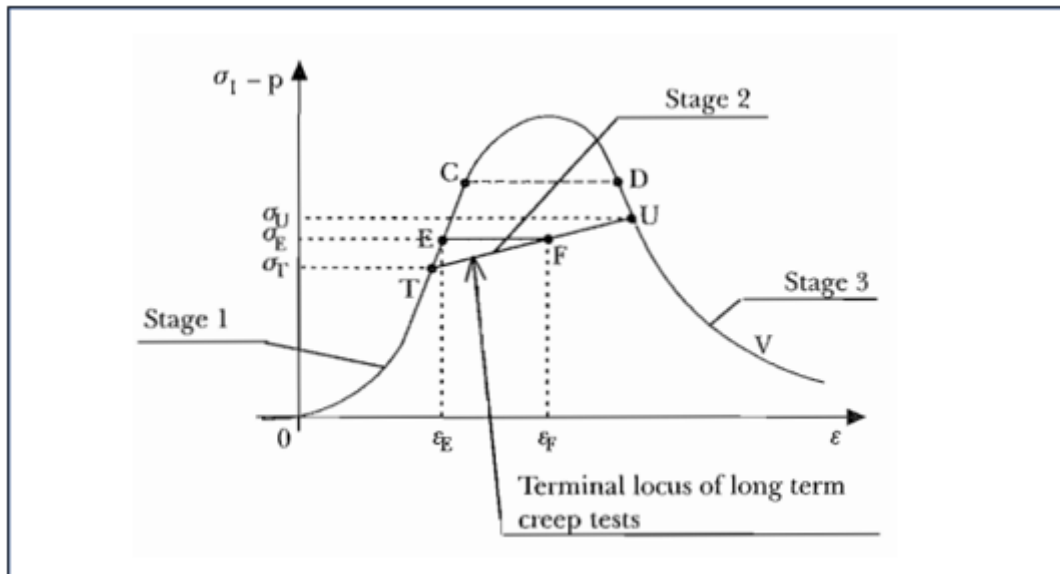
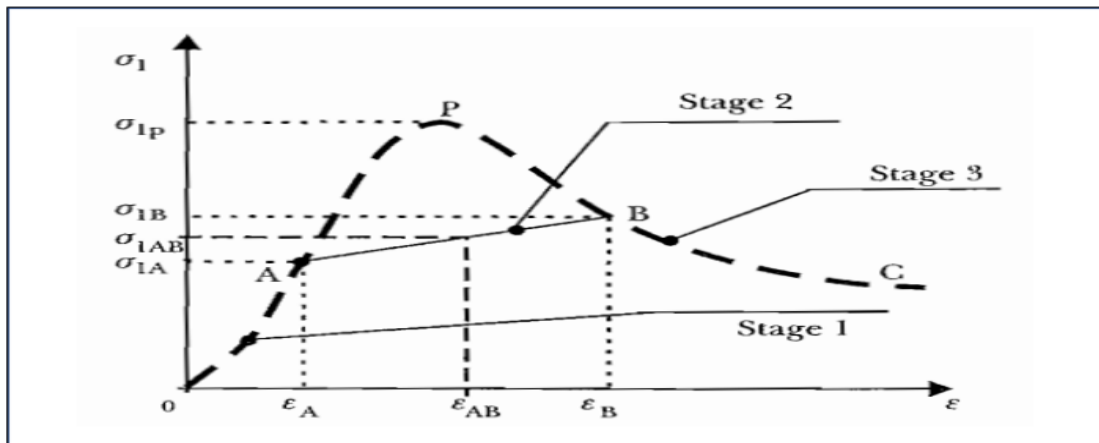


Figure 7.7: The complete stress-strain curve (LADANY1,1993).

With respect to the next three stages:

- stage 1: elastic behavior.
- stage 2: viscous behavior.
- stage 3: permanent large deformations occur.

Moving from the second stage to the third stage occurs to the plastic strain which is a function of the state of the stress. In the long-term stage, the behavior considers plastic again according to the Mohr-coulomb plasticity model. Thus, the friction angle and cohesion have been decreased by using a softening formulation as a function of the plastic accumulated strain.



**Figure 7.8:** Proposed model for the analysis of squeezing behaviour (Barla and Borgna,2000).

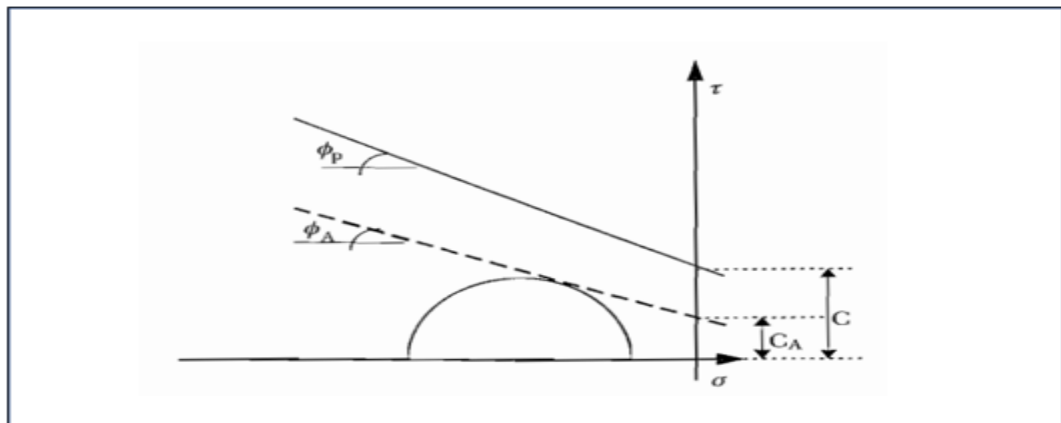


**Figure 7.9:** Mohr-Coulomb envelopes used to define stage 1 and stage 2 on the complete stress-strain curve (Barla and Borgna,2000).

Equations 7.7 and 7.8 have been obtained from doing different simulations of uniaxial conditions by using the FLAC code (ITASCA,1996). The hardening/-softening behavior can be simulated with the variation of strength parameters (cohesion, friction angle, and dilation angles) as a function of plastic shear strain.

$$\phi_{BC} = 13.4(\epsilon_{BC} - \epsilon_A)^{-0.2065} \quad (7.7)$$

$$c_{BC} = c_A(1 - (\epsilon_{BC} - \epsilon_A)) \quad (7.8)$$

These relationships have been applied to the case under study. The results are collected in tables 7.2 and 7.3 .

**Table 7.2:** Decreasing of the friction angle.

BS-strong class III		BS-weak class III		BS-weak class IV	
Strain(-)	$\phi(^{\circ})$	Strain(-)	$\phi(^{\circ})$	Strain(-)	$\phi(^{\circ})$
0.000	47.0	0.000	41.1	0.000	34.8
0.004	32.9	0.002	32.8	0.002	32.2
0.005	32.9	0.003	32.8	0.002	32.2
0.006	32.9	0.004	32.8	0.003	32.2
0.006	32.9	0.004	32.8	0.003	32.2

**Table 7.3:** Updated cohesion values

BS-strong class III		BS-weak class III		BS-weak class IV	
Strain(-)	c(Mpa)	Strain(-)	c(Mpa)	Strain(-)	c(Mpa)
0.000	2.70	0.000	2.05	0.000	1.55
0.004	1.51	0.002	1.15	0.002	0.87
0.005	1.51	0.003	1.15	0.002	0.87
0.006	1.51	0.004	1.15	0.003	0.87
0.006	1.51	0.004	1.15	0.003	0.87

The adopting strain-softening model for BS-strong III, BS-weak III, and BS weak IV are shown in figures 7.10 to 7.12. The reduction in friction angle is around 30 percent except in BS-weak IV is around 10 percent. With respect to cohesion, in BS-strong III ,BS-weak III and BS-weak IV ,cohesion is reduced up to 45 percent as shown in following figures from 7.13 to 7.15.

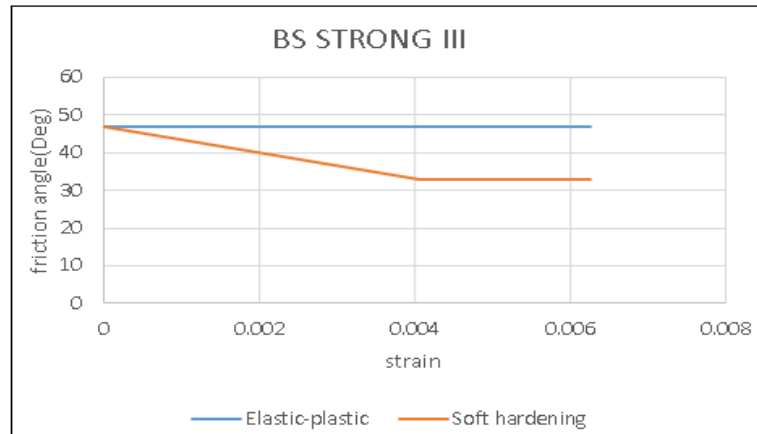


**Figure 7.10:** Friction angle reduction(BS-strong III).

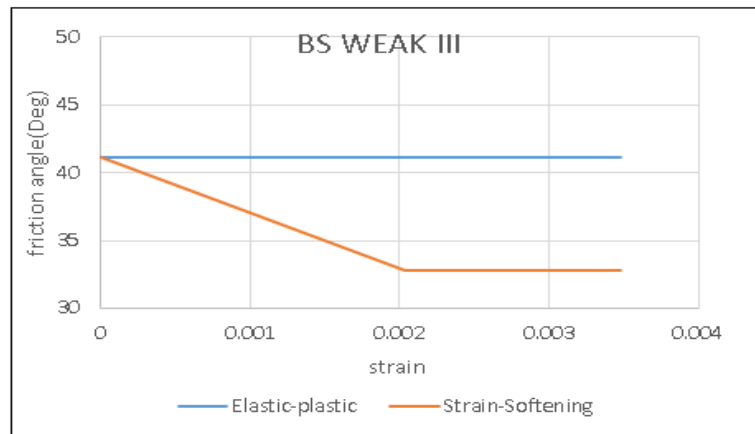


**Figure 7.11:** Friction angle reduction(BS-weak III).

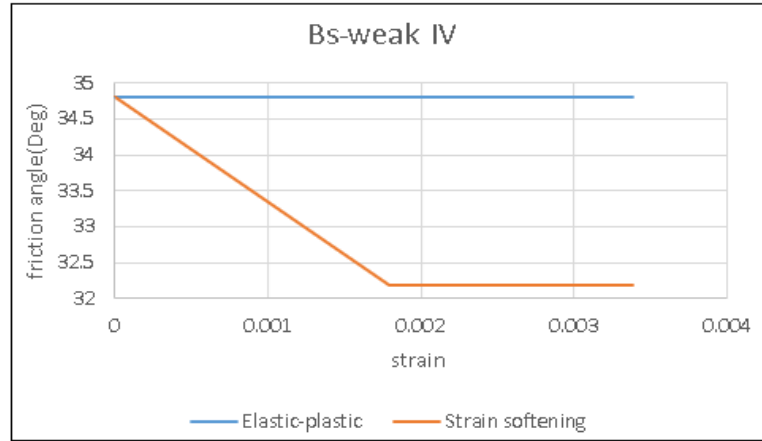


**Figure 7.12:** Friction angle reduction(BS-weak IV).

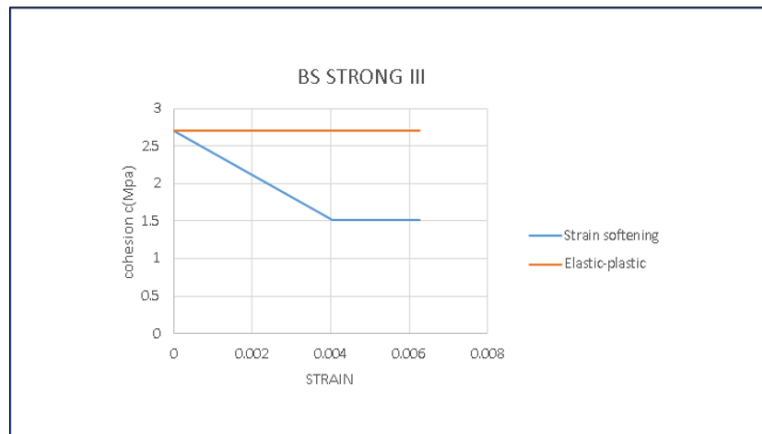


**Figure 7.13:** Cohesion reduction (BS strong III).

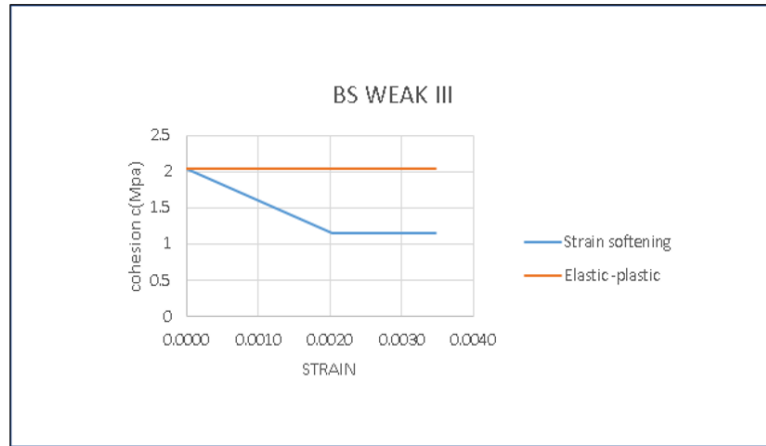


**Figure 7.14:** Cohesion reduction (BS weak III).

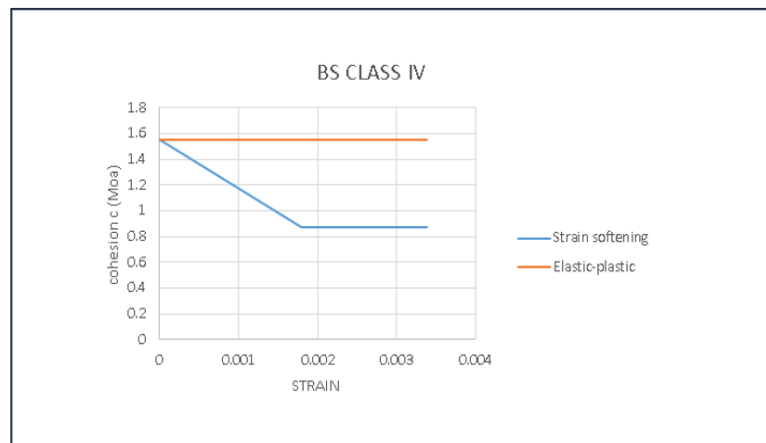


**Figure 7.15:** Cohesion reduction (BS weak IV).

**Table 7.4:** Mohr coulomb input parameters (First scenario simulation).

	Peak strength	Residual strength		
Lithology	c(Mpa)	$\phi(^{\circ})$	c(Mpa)	$\phi(^{\circ})$
bs-strong classIII	2.7	47.01	1.51	32.9
bs-weak classIII	2.05	41.08	1.15	32.8
bs-weak class IV	1.55	34.8	0.87	32.2
Pyr	0.7	19.76	0.7	19.76
bs weak V	0.765	23.49	0.765	23.49
faults	0.1	23	0.1	23

In table 7.5, the residual values of the cohesion remained the same as it was defined in chapter 4 .

**Table 7.5:** Mohr-coulomb input parameters(Second scenario simulation).

	Peak strength	Residual strength		
Lithology	c(Mpa)	$\phi(^{\circ})$	c(Mpa)	$\phi(^{\circ})$
bs-strong classIII	2.7	47.01	0	32.9
bs-weak classIII	2.05	41.08	0	32.8
bs-weak class IV	1.55	34.8	0	32.2
Pyr	0.7	19.76	0.7	19.76
bs weak V	0.765	23.49	0.765	23.49
faults	0.1	23	0.1	23

## 7.4 Long term behaviour results

### 7.4.1 First scenario simulation

#### Total displacements

In general with the first scenario, the results of total displacements are more compatible with the monitoring data after around 2 year from when the construction was started. The total maximum displacement is 0.18 m. Also, the maximum value is located in the same spot between faults 22,31 and the pyroclastic layers number 9. The displacements in the north and the south wall are around 10 cm. On the other hand, the rest part is stable. The results are illustrated in figures 7.16 and 7.17.

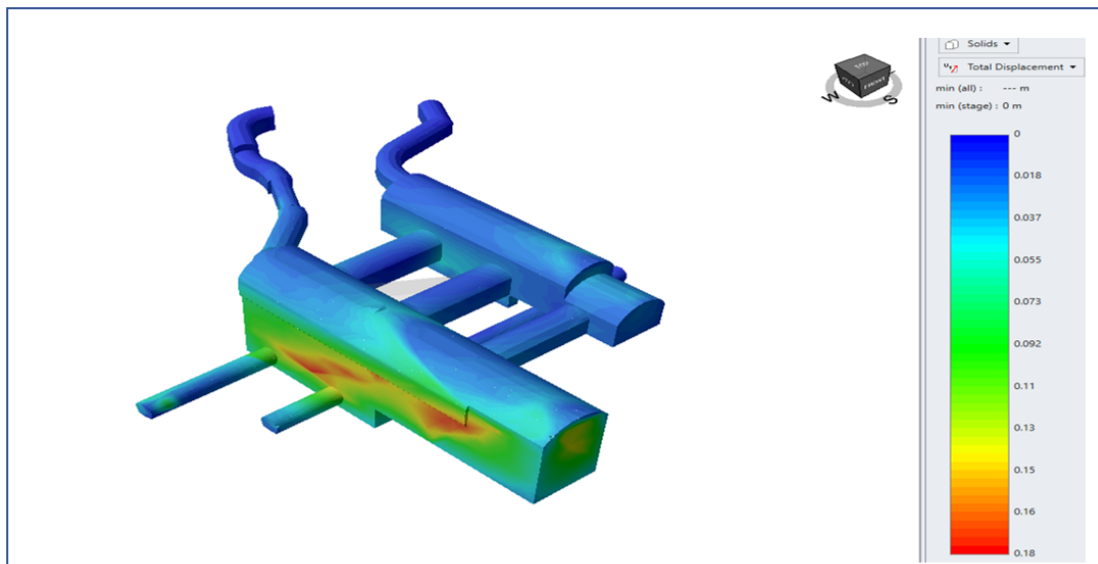


**Figure 7.16:** Total displacement in south and upstream sidewall(first scenario).

#### Axial force in tendons and bar anchors

In figure 7.18, the results of axial forces are shown. Group of bar anchors in the first layer of the power house in the upstream wall reach the maximum capacity 180 tons. But the major part of the tendons and bar anchors are located in range between 50 to 100 tons. Also in this scenario, the results are quite close to the monitoring data.

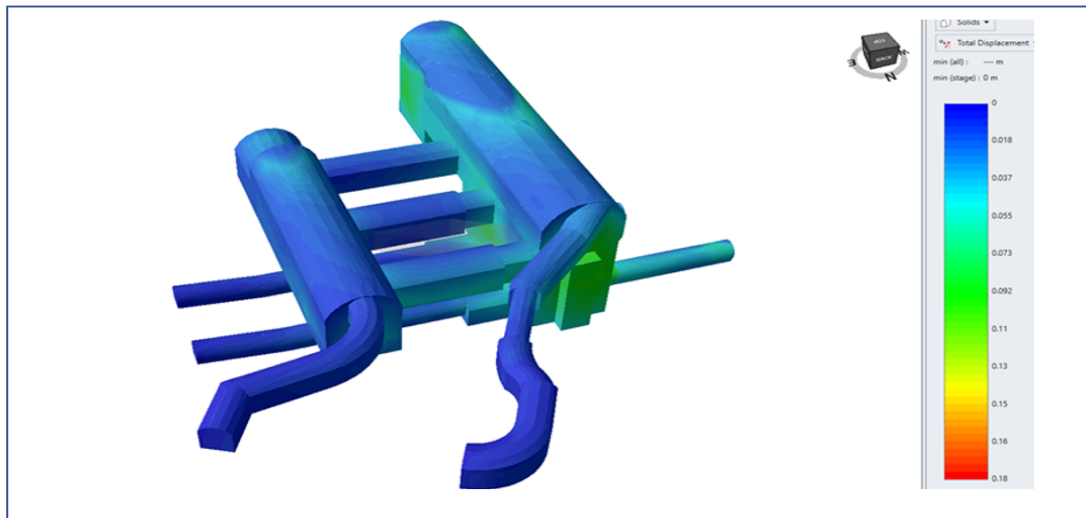


**Figure 7.17:** Total displacement in south and upstream sidewall(first scenario).

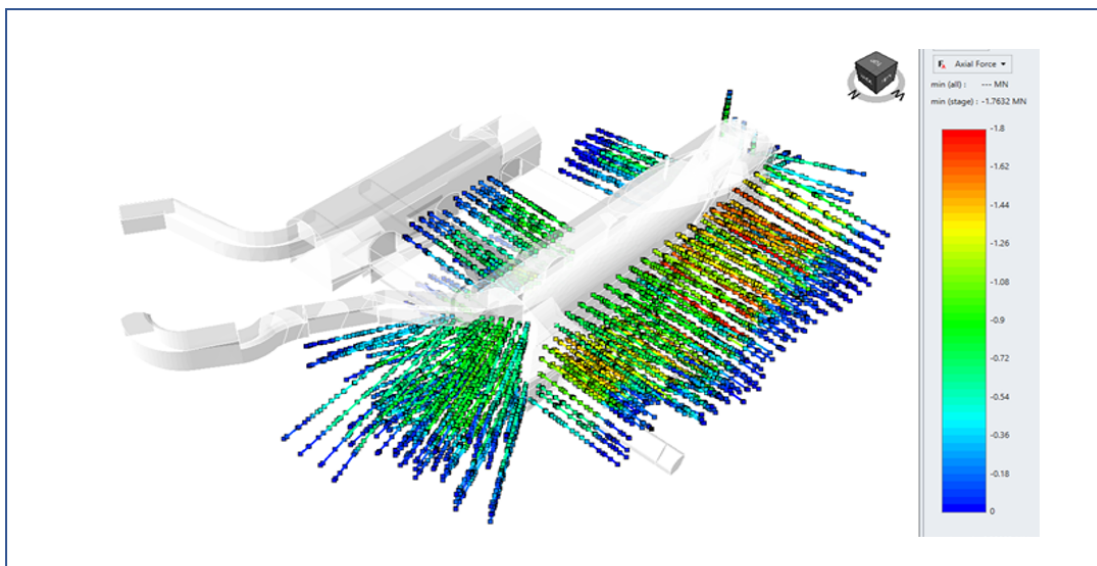


**Figure 7.18:** Axial force in tendons and bar anchors(first scenario).

### Axial stress in rock bolts

The results in terms of stresses are clarified in figure 7.19. Rock bolts which are located in the intersection among faults,pyroclastic layers and the excavated structure reach the maximum capacity(above 500 MPa).Thus,that means RS3 is sensitive to the intersection between different layers. The stress of most rock bolts is in range of 180 to 250 MPa.

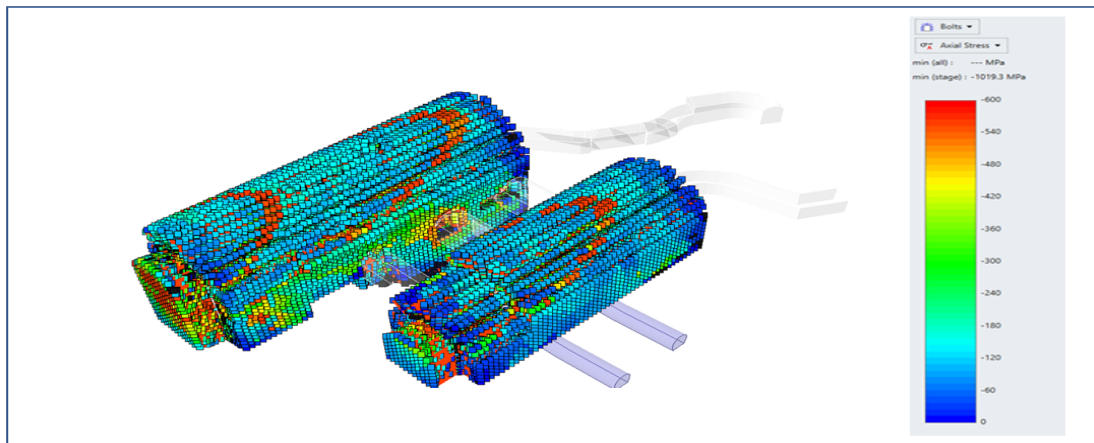


Figure 7.19: Axial stress in rock bolts(first scenario).

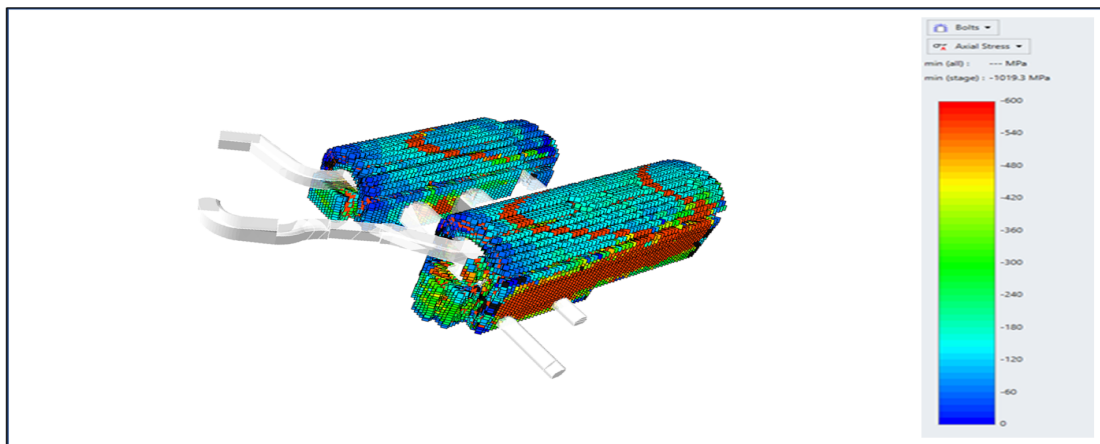


Figure 7.20: Axial stress in rock bolts(first scenario).

## 7.4.2 Second scenario simulation

### Total displacements

The total maximum displacement reaches 0.63 m which is around 50 percent more than the previous results. Also, the maximum value is located in the same spot between fault 22,31 and the pyroclastic layer number 9. Moreover, the rest part of the structure is affected by high values of displacement especially the north and the south wall.

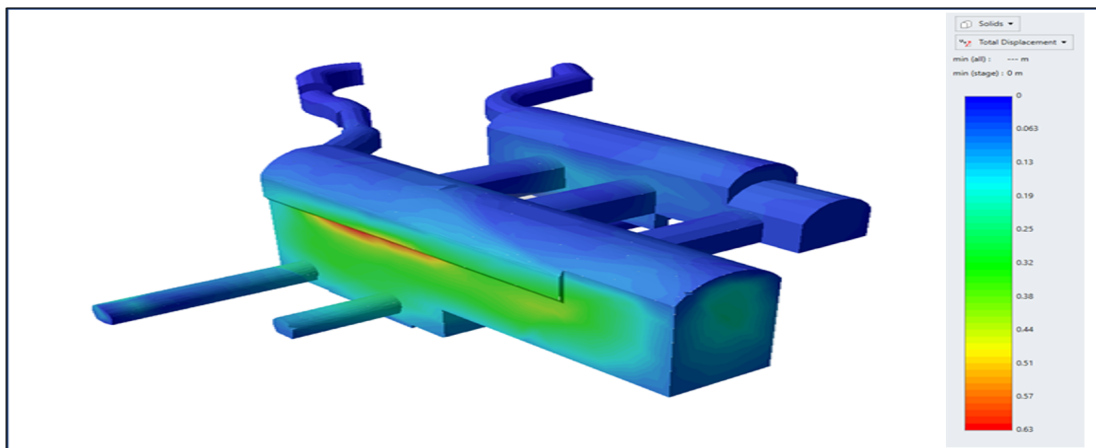


Figure 7.21: Total displacement in south and upstream sidewall(second scenario).

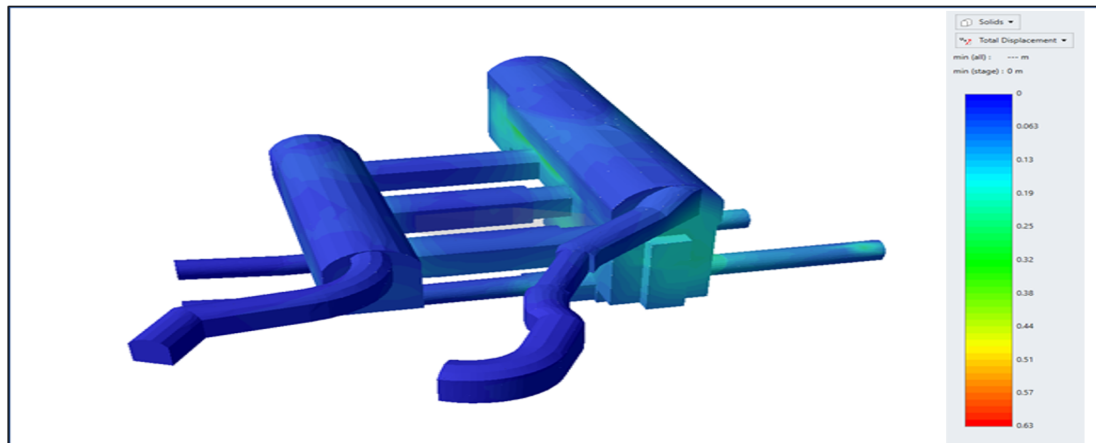


Figure 7.22: Total displacement in north wall and downstream side wall(second scenario).

### Axial force in tendons and bar anchors

The results in terms of axial forces are illustrated in figures 7.23 and 7.24. Few bar anchors in the top part of the north wall reach the maximum capacity. The higher portion of the tendons and bar anchors are in the range between 90 and 120 tons. Also, few tendons in both upstream and downstream walls reach 180 tons.

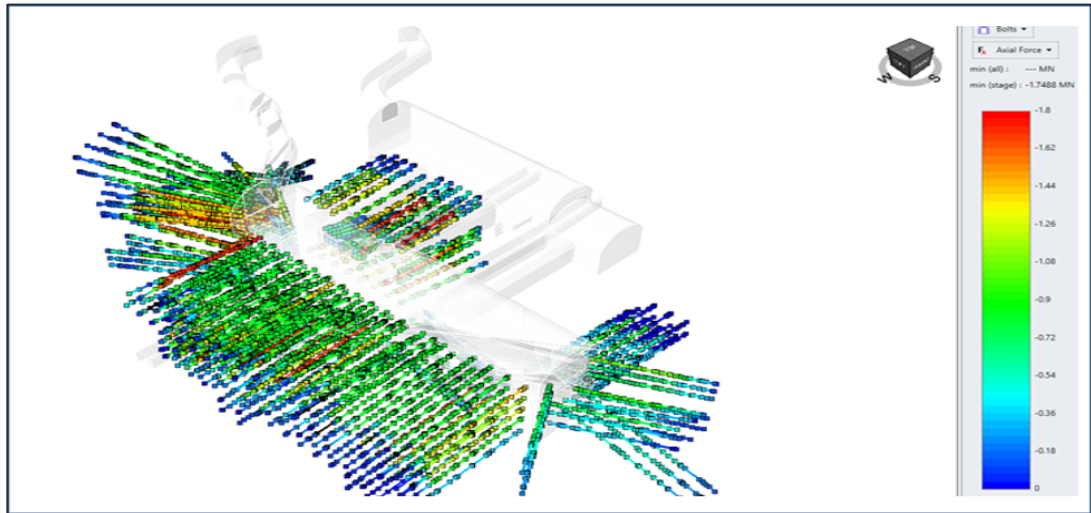


Figure 7.23: Axial force in tendons and bar anchors(second scenario).

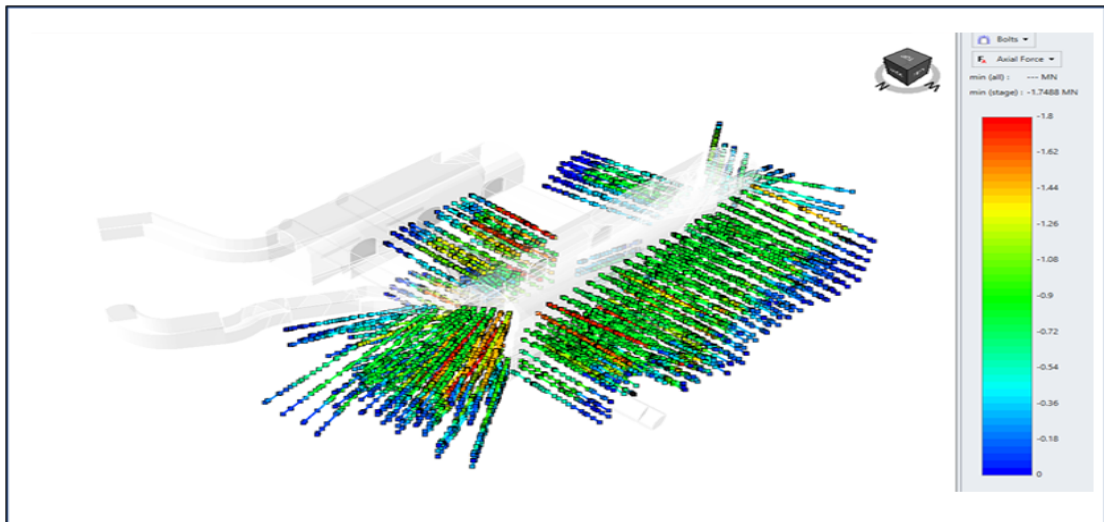


Figure 7.24: Axial force in tendons and bar anchors(second scenario).

### Axial stress in rock bolts

In this section, the axial stresses in rock bolts are shown in figures 7.25 and 7.26. Most of the rock bolts located in the upstream sidewall, the rock bolts located in the intersection between the bus bar tunnels and the transformed hall and the rock bolts in the intersection between the structure and the pyroclastic layers have been reached failure. The stress of most rock bolts is in the range of 240-550 MPa.

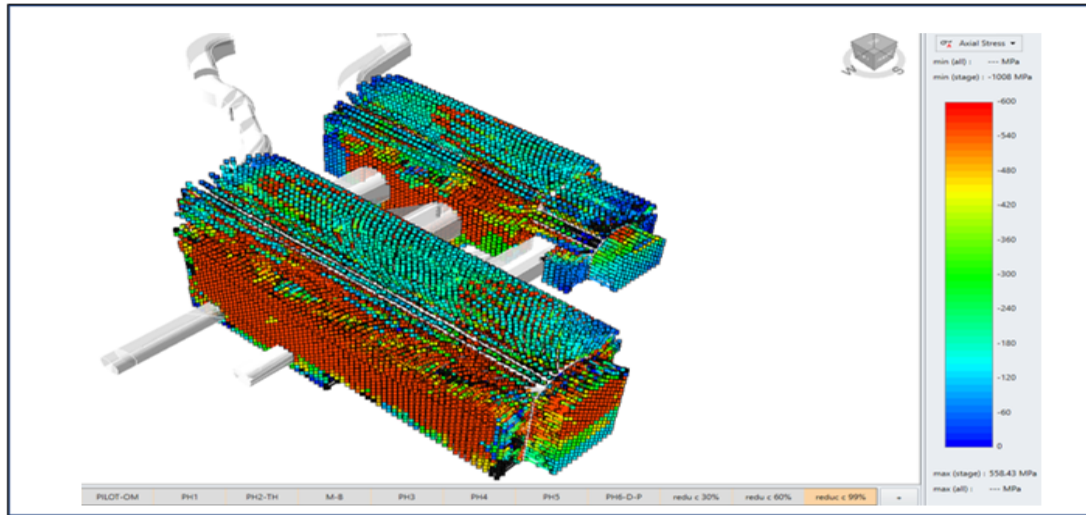


Figure 7.25: Axial stress in rock bolts(second scenario).

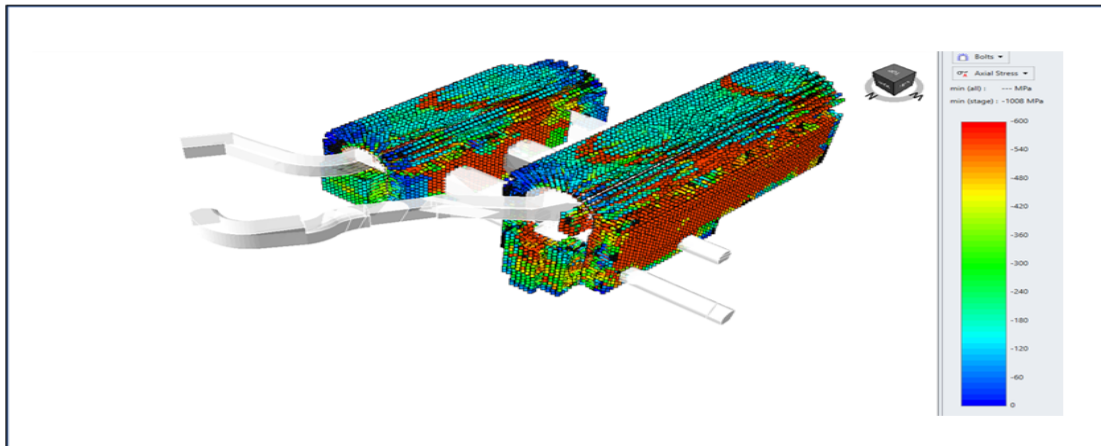


Figure 7.26: Axial stress in rock bolts(second scenario).

The situation seems worsen over time due to the long term behaviour of rock. It should be noted that the obtained results have to be considered not in absolute terms because ,as highlighted in previous chapter, the RS3 analyses give a conservative results. In relative terms, in any case, a worsening of the stability scenario is expected.

# Chapter 8

## Conclusion

This study is devoted to the project of a complex system of caverns and tunnels of a big hydroelectric power plant. Numerical analyses by FEM in a 3D environmental have been performed, by means of RS3 code. The results are compared with previous analyses performed with FDM approach by FLAC 3D code and with monitoring data. Moreover, the validated RS3 model has been used to consider the time.

Some key points and suggestions summarized as follows.

1- The outputs of calculation by RS3 code are matching with the results obtained by FLAC 3D code with equivalent parameters and in-situ stress parameters.

2- In general, the results related to support deformation and stresses from the numerical analysis are higher than the measured one from monitoring data.

3- Further investigations are mandatory because some elements have different behavior than the predicted model.

4- The rock bolts stress gauges are very sensitive to the geological joints or rupture across the sensors.

5- The model reaches equilibrium. However, geological and geomechanical conditions are implemented in the simulation which are less favorable than in reality.

6- By considering the time-dependent results, the achievement of equilibrium in long-term behavior is guaranteed .

The solutions for withstanding the overloaded tendons and bar anchors are suggested below:

-The overloaded anchor shall be substituted by new anchors or shall be released to 80 percent service capacity.

- The temporary tendons are considered to be released after substituted anchors are installed.

# Bibliography

- [1] Charlie Chunlin Li. «Field observations of rock bolts in high stress rock masses». In: *Rock Mechanics and Rock Engineering* 43.4 (2010), pp. 491–496 (cit. on p. 13).
- [2] Hongkui Gong, Mehmet S Kizil, Zhongwei Chen, Moe Amanzadeh, Ben Yang, and Saiied M Aminossadati. «Advances in fibre optic based geotechnical monitoring systems for underground excavations». In: *International Journal of Mining Science and Technology* 29.2 (2019), pp. 229–238 (cit. on p. 31).
- [3] Evert Hoek and Mark S Diederichs. «Empirical estimation of rock mass modulus». In: *International journal of rock mechanics and mining sciences* 43.2 (2006), pp. 203–215 (cit. on p. 40).
- [4] Evert Hoek and ET Brown. «The Hoek–Brown failure criterion and GSI–2018 edition». In: *Journal of Rock Mechanics and Geotechnical Engineering* 11.3 (2019), pp. 445–463 (cit. on p. 40).
- [5] Ömer Aydan, T Akagi, and T Kawamoto. «The squeezing potential of rocks around tunnels; theory and prediction». In: *Rock mechanics and rock engineering* 26.2 (1993), pp. 137–163 (cit. on pp. 99–101).
- [6] G Barla and Stefania Borgna. «Numerical modelling of squeezing behaviour in tunnels». In: *Associazione Geotecnica Italiana (AGI, 20 0 0* (2000) (cit. on p. 99).
- [7] G Russo and P Grasso. «On the classification of the rock mass excavation behaviour in tunneling». In: *11th ISRM Congress*. OnePetro. 2007 (cit. on p. 102).